On the analysis of near-infrared point spectrometer data for the investigation of lunar surface mineralogy

vorgelegt von
Esa Vilenius
aus Helsinki, Finnland

D7

Referent: Prof. Dr. Martin Kappas

Korreferent: Dr. Urs Mall

Tag der mündlichen Prüfung: 19.2.2009

Cover image: The SIR instrument (top left), a schematic view of the sensor head part of SIR (top middle), reflectance spectra at 1.0 to 2.2 μm from a small crater at the wall of the Eimmart crater (top right), ultraviolet and visible image of Aristarchus crater by Hubble Space Telescope, credit: NASA/ESA HST Moon team (background).

Contents

Summary

Near Infrared (NIR) spectra provide compositional and mineralogical information of the lunar surface focusing on the distribution of fundamental mineralogical components such as pyroxene, olivine and plagioclase. Given that lunar regolith's absorption features in NIR spectra are often weak, in order to extract useful and reliable geochemical information it is imperative to achieve an accurate calibration and photometric data reduction of the whole data set, measured in various illumination geometries.

In 2003 the European Space Agency (ESA) launched the SMART-1 spacecraft, a technology demonstrator, which was also their first scientific mission to the Moon. In 2005-2006 one sixth of the lunar surface was observed by the onboard 256-channel NIR point spectrometer, called *SMART-1 infrared spectrometer* (SIR), with a spectral range of 0.9 to 2.4 μm, and spatial resolution between 300 m and 3 km.

Chandrayaan-1, the first Indian mission launched to the Moon in October 2008, has an improved version of the SIR spectrometer called SIR-2, employing an upgraded detector, along with other improvements targeting thermal stability issues. Furthermore, the circular orbit of 100 km altitude chosen for the Chandrayaan-1 mission, rather than an elliptical one as per the SMART-1, is better suited for remote sensing surveys, potentially yielding more consistent scientific data.

In this work the data reduction of the data sets of SIR and SIR-2 spectrometers has been developed starting from calibration measurements and their analysis and including necessary steps to produce reflectance factor values as a function of wavelength. The absolute sensitivity, photo-response nonuniformity, linearity properties, wavelength range, and spectral resolution of the SIR-2 and SIR-2 flight spare model have been determined by measurements in a controlled environment with calibrated sources in terms of wavelength and intensity of light. During this work the analysis of SIR calibration measurements has been improved too, and a simulated output of the instruments has been calculated. Due to the 16-month journey of SMART-1 to the Moon, and the thermal cycling and radiation involved, the instrument response extracted from laboratory calibration did not compare in full with the inflight instrument response of SIR. Inflight calibration information has been acquired by observing the Apollo landing sites where samples have been returned and their NIR spectra measured in laboratories; this comparison produced a wavelength-dependent correction factor.

The photometric function used in this data reduction is a combination of Akimov's disk function and the semi-empirical Shkuratov phase function, whose parameters at NIR have not been sufficiently determined before. The shadow hiding parameter of this function has been fitted using SIR data from target tracking observation of selected sites at varying phase angles. The value of the parameter was found to be $k = 1.07 - 0.00015\lambda[nm]$, where λ is the wavelength.

1 Introduction

With three ongoing and several planned missions, the Moon has become the target of interest to several space faring countries and agencies. Mapping and exploration for the purpose of resource utilization and renewed human presence are under way with new high-resolution instruments never used in lunar science before. Remote sensing and other remote observation techniques have provided a wealth of scientific data for planetary research since returned samples from known locations are available only from nine sites on the Moon.

Near Infrared (NIR, 0.7-3.0 μm) spectroscopy provides a tool for determining which minerals are present on the surface. The detection is based on mineral-dependent absorption of solar light when photons travel through the uppermost part of regolith or rocks before scattering towards the direction of the observing instrument. Knowing the minerals, which have different solidification temperatures, it is possible to infer the temperature under which solidification took place, and thus have information about the history of rock formation via melting, differentiation, crystallization, and volcanic processes.

Ground based observations are limited by the atmospheric absorption bands in NIR; to avoid that absorption, to get a closer look with higher spatial resolution, and to observe surfaces which are not visible from the Earth, spacecraft are sent to orbit planets, moons, and small bodies of the solar system.

One of the scientific reasons why we investigate the Moon is that it is the closest terrestrial object, and it can be compared in size to other solar system bodies without an atmosphere, like Mercury and the large moons of Jupiter. For instance, both Mercury and the Moon have experienced heavy cratering. There are also differences between the two terrestrial bodies in the inner solar system: Mercury has a global magnetic field whereas the Moon does not, indicating different core structures, and the plains of Mercury contain less iron than the dark maria of the Moon. The returned regolith and rock samples combined with spacecraft observations give an insight of our Moon, and this information can be used in comparative studies.

Another scientific aspect is that the Moon has preserved a record of solar wind in its regolith. Helium-3, carried to the surface of the Moon by the solar wind, might be used as fuel for fusion power plants in the future. Although the relative amount of Helium-3 is very small and requires the excavation of the upper regolith layer and a method to extract Helium-3, it is potentially an economically feasible source of fuel once the fusion technology is developed. Fuel cell catalysators require metals which are rare on Earth and they have been found mostly in areas of old meteorite impacts. Those metals could also be found in many of the lunar impact craters. Although the Moon is dry, water brought by comets might be found as ice at cold dark crater bottoms near the poles, having collected there as a result of ballistic leaps of individual molecules. Indirect evidence of hydrogen

deposits have been suggested by spacecraft missions, but the findings and amounts of H_2O still remain to be further investigated. There is another class of observations called lunar transient phenomena which are bright flashes that occur randomly on the Moon's surface about a dozen times per year and their origin remains unclear. The Moon also has local magnetic anomalies associated with albedo features called swirls; there are many theories about their origin.

The moon of the Earth was investigated extensively from the late 1950's to the mid-1970's. After failed attempts by USA missions, the first picture from the farside was taken by the Soviet Luna 3 mission in 1959. The first robotic soft landing including TV pictures from the surface were accomplished in 1966 by the successful Luna missions. The USA was more successful in manned missions with six landings in 1969-1972 but after that, the interest in the Moon decreased dramatically. The Soviet Union had the first rover and robotic sample return missions in 1970; their Moon program ended in 1976 with Luna 24, their third robotic sample return. Following the 12 successful lunar missions by the USA and the USSR in the 1970's there were no Moon missions all through the 1980's. Lunar exploration resumed in 1990 when a small Japanese spacecraft called Hiten made a dust and gravity study.

The Galileo mission to Jupiter, made two Earth flybys in the 1990's and took pictures and spectra of the Moon (see Section 1.4.1). It carried onboard an imaging spectrometer. The USA Clementine mission of 1994 had imaging cameras at several bands at ultraviolet, visible and NIR wavelengths, which were used to make inferences on mineralogy, but it did not carry spectrometers (see Section 1.4.2). On the other hand the Lunar prospector mission in 1998, also from USA, did not have cameras, but it had spectrometers for gamma rays, neutrons and alpha particles.

The first European lunar mission was the SMART-1 in 2003-2006 (see Section 1.4.4). After a 16-month journey it reached a polar elliptic orbit with perigee at 300 km and apogee at 3000 km and observed the Moon for one and half years until a planned impact in September 2006. The SMART-1 carried on board the first high resolution NIR spectrometer SIR, which had been sent to orbit the Moon together with six other instruments.

In 2007 two Asian countries launched their lunar missions which are currently orbiting the Moon: the Chinese Chang'e and the Japanese Kaguya with its two sub-satellites. Kaguya is on a 100 km polar orbit and carries 13 science instruments on board, one of them is a visible to NIR spectrometer targeting mineral identification. Kaguya's mission objectives are global characterisation of the lunar surface and detailed gravimetry (see Section 1.4.3). Chang'e is on a 200 km polar orbit with six science instruments. It is used to capture 3D images and map geologic structures. It is also used for investigating the depth of the lunar regolith and space weather processes between the Earth and the Moon. Chang'e carries on board a spectrometer for visible wavelengths with a spatial resolution of 200 m.

The first Indian Moon mission Chandrayaan-1 was launch in October 2008 for the purposes of high resolution selenological and chemical mapping (see Section 1.4.4). It is on a circular polar orbit at an altitude of 100 km. Among the 11 science instruments it carries an upgraded NIR point spectrometer SIR-2 built by the Max Planck Institute for Solar System Research as a ESA contribution to the mission.

NASA is planning the launch of the Lunar Reconnaissance Orbiter mission for spring 2009 intended as a preparatory mission for human exploration. It will have cameras

with spatial resolution of 0.5 m, similar to that currently onboard Mars Reconnaissance Orbiter, instruments to map mineralogy and radiation environment, and a radar to search for water ice. For 2011 NASA is planning a mission with two orbiters called GRAIL and LADEE to investigate the lunar gravity field and its interior. India's Chandrayaan-2 with an orbiter and a Russian rover is planned for 2011 as well. For the decade 2012-2021 there are preplans to send both orbiters and landers by several countries: Germany (LEO, BW 1), United Kingdom (Moonraker, MoonLITE), Russia (Luna-Glob), China (Chang'e 2 and 3), Japan (Kaguya 2 and 3), India (Chandrayaan-3), ESA (MoonNEXT), and Korea. NASA has planned a series of missions culminating in a human landing in the 2020's. Also entrepreneurs are encouraged to send a rover to the Moon and collect the Google Lunar X-prize reward. The competition is on until 2014, and currently there are 10 private teams working towards that goal.

Outline of the thesis

Extracting high-quality science data from the high-resolution instruments requires that their instrument response has been carefully measured under laboratory conditions. The observing instrument gives an output signal which is a combination of the incoming physical signal, electromagnetic radiation or particles, and the instrument itself. Optical instruments, like the NIR spectrometers SIR and SIR-2 (characterised in Chapter 2), are calibrated with respect to incoming intensity of light as well as for the response to different wavelengths. Also the instrument output with no incoming light is investigated in different physical conditions of the instrument, with temperature being the most important variable. The calibrating devices themselves must be in a known status of calibration, which can be derived from national standards. However, even our best ground calibrations may not represent the true status of the instrument after the launch and cruise phases. The ground calibrations of the SIR and SIR-2 instruments are described in Chapters 3 and 4 of this thesis. Calibrations of NIR instruments in previous missions have needed major corrections also during the science mission. For example, the flight calibration of the NIR camera onboard the Clementine spacecraft has taken a considerable time and effort. The inflight calibration can use astronomical objects whose spectra and intensities are known, or areas on the planetary surface where an expected response is already known. On the Moon typical ground truth locations are some of the Apollo landing sites, from which samples have been analysed in laboratory, and which are representative enough to be compared to remote sensing observations. In the data reduction of visible and NIR data the specific illumination conditions have to be taken into account, because changes in the incidence and emergence angles affect the spectrum. Data reduction including the photometric corrections for illumination geometry as well as the inflight calibration are described in Chapter 5. Sample cases from the SMART-1 / SIR data are shown in Chapter 6.

The following Subsections in this Chapter offer an introduction to lunar mineralogy, reflectance spectroscopy, spectrometers and previous NIR experiments onboard Moon orbiting spacecraft.

1.1   Lunar mineralogy and geology

Before the age of spacecraft observations there were unverified speculations about the composition and origin of our closest neighbor in the Solar System. The advantage was, though, that the Moon is close enough to distinguish features on its surface even without any instruments. There are two major terrain types: the heavily cratered highlands, and the lightly cratered, probably younger, maria. They are darker in color and cover one sixth of the nearside. There were speculations, which are nowadays known to be false, that the highlands were composed of granite and maria are sediments only a few million years old, or that the Moon was an undifferentiated object (Taylor 2005). Also, most of the craters were thought to be of volcanic origin. Valley formations called rilles led to the erroneous conclusion that flowing water had been present. Even though many geological speculations turned out to be false later, ground-based observations did give information about the Moon's orbit, the 1:1 resonance of orbital and rotational periods, lunar density, and angular momentum. Inferences about the internal structure could be made based on the density and angular momentum data.

In the late 19th and early 20th centuries several theories were proposed to explain the origin of the Moon (Schrunk et al. 1999). George Darwin stated that since the Moon is slowly receding from the Earth, it would have originated in the fission of an asymmetric early Earth. The problem with this fission hypothesis was that the Moon could not have formed within the Roche limit of the Earth. Other theories of that time were the Laplace theory, supported by Roche himself, where the two bodies formed by co-accretion at the same time and in the same neighborhood. In the capture theory by Thomas See the Moon had been captured in the same way as some of the moons of Jupiter and Saturn.

The current understanding of the formation of the Moon is based on isotopic data from the 400 kg of samples from six Apollo and three Luna sites on the nearside, as well as on dynamic modelling. Oxygen isotopic compositions of different inner solar system bodies show heterogeneity and since the oxygen-isotopic composition is similar between Earth and the Moon they would have formed from a similar mix of material. The leading current theory is the Giant Impact hypothesis. According to this theory, a Mars-sized object named Theia impacted the Earth, consequently the impactor was destroyed and part of early Earth's mantle was thrown into orbit. The new bulk Earth and the disk of ejecta were thus a combination of material from both the proto-Earth and the impactor. From this disk of vapor and debris the Moon begun to accrete. Pahlevan and Stevenson (2007) speculate that the debris disk remained connected to the Earth by silicate vapor and diffusive mixing evened out the differences of those elements which eventually vaporized, such as oxygen. Dynamical simulations suggest that most of Moon's mass came from Theia (Canup and Asphaug 2001). A recent refinement of the timing of the giant impact gives an estimate of 62^{+90}_{-10} million years after the formation of the Solar System accretion (Touboul et al. 2007), which occurred 4567 million years ago.

At the beginning the Moon probably featured a global magma ocean, which began to solidify at around 200 million years (Touboul et al. 2007). There was at least some partial differentiation during the magma ocean phase, producing a highly aluminous flotation crust enriched in plagioclase feldspar. The duration and depth of differentiation is a key question in lunar geology, as well as the existence of a possible undifferentiated lower mantle.

Minerals and regolith

A fundamental source of data on lunar minerals and geology have been the returned samples. They were studied, and still continue to be studied, with all the conventional methods of geochemistry, mineralogy and petrography (e.g. Lunar Sample Preliminary Examination Team 1969, Alvarez et al. 1970, Papanastassiou and Wasserburg 1971, Apollo 17 Preliminary Examination Team 1973, Andersen and Hinthorne 1973, Benkert et al. 1993, Saal et al. 2008). From the samples it was quickly realised that the maria formed as a result of basaltic lava flows due to partial melting of the mantle. The paucity of central volcanic cones is explained by the high fluidity of lunar lavas compared to Earth lavas. The maria basalts contain pyroxene, and are enriched in iron and titanium in comparison to Earth's equivalent. The highland rocks are mostly feldspathic breccias of anorthositic composition, with aluminum and calcium as the major elements. They are strongly enriched with trace element materials called KREEP (potassium, rear Earth elements and phosphorus).

The major minerals on the Moon are pyroxenes, olivines, plagioclases and ilmenite and as most lunar minerals, they are also common on Earth. Nevertheless, the Moon is depleted in comparison to Earth in iron and volatile elements. The principal difference is that on the Moon there are no minerals that indicate the presence of water, for instance, clays, micas and amphiboles are missing; potassium feldspar is also rare, whereas on Earth it is common. Oxide minerals are found mainly in the mare regions and ilmenite containing titanium is typical of mare basalts.

Regolith, the few meters thick fragmented rock debris caused by impacts on the surface, is composed of all grain sizes. Impacts have further pulverized the regolith over time and it is also affected by space weathering. The mean grain size is 60 μm to 70 μm (Papike et al. 1991).

Cratering rates

The determination of the ages of the returned samples was essential in calibrating cratering rates (Ivanov and Hartmann 2007). They are between 3 and 4 billion years old, so even the youngest maria samples are as old as the oldest rocks on the Earth. Since the Moon has been geologically inactive for the last 3 billion years it is possible to estimate the cratering rate (the number of craters of a given diameter per square kilometer) at a given time interval. The rate of formation of new craters due to meteorite bombardment is decaying with time since the formation of the Solar System, and together with the absolute ages from lunar samples, geologic evolution of the terrestrial planets has become better understood. Both Mercury and the Moon may have experienced a downpour of meteorite impacts at the end of the formation of the solar system called Late Heavy Bombardment.

Internal structure

The seismic experiments of the Apollo missions provided new information about the inner structure of the Moon, although they were installed only on five landing sites on the nearside. The crust is on average 60 km thick, the litosphere extends to a depth of around 1000 km, and below it, we find a partly liquid astenosphere down to 1740 km. Doppler

gravity data from the later Lunar Prospector mission in 1998 indicate the possible pres-
ence of an iron core with a radius of 220 to 450 km, and a mass of less than 3% of the
Moon mass (Konopliv et al. 1998).

Farside and nearside asymmetry

The first pictures from the farside of the Moon revealed obvious geological differences
in comparison to the nearside: maria only cover 1% of the farside compared to 17% on
the nearside (Papike et al. 1991). One of the results from the Apollo program was that
the shape of the Moon is asymmetric i.e. the crust on the farside is thicker than on the
nearside. Data from the Clementine mission show that the center of mass is displaced two
kilometers toward the nearside from the center of the figure of surface (Zuber et al. 1994).
Based on modelling of the formation of impact basins, combined with topographic and
crystal thickness data, it has been suggested that a large impact on the nearside excavated a
mega basin throwing an ejecta blanket mantling the farside (Byrne 2007), and thus caused
the farside and nearside asymmetry.

1.2 Bidirectional reflectance spectroscopy

Spectroscopy can be defined as the study of light as a function of wavelength that is
reflected, emitted or scattered from a solid, liquid, or gas (Clark 1999). As photons enter
a mineral or an amorphous rock some of them are absorbed whereas others are refracted
and scattered again in other mineral grains. Some of the scattered or emitted photons
will eventually reach an observing instrument, where the absorption signatures of the
mixture of minerals within the field of view of the instrument are seen in the spectrum.
Reflectance spectroscopy is used by telescopic and spacecraft observers alike and as a
tool in laboratory analysis of samples. The infinitesimal power dP measured by a remote
sensing instrument from a surface element dA is

$$dP(r) = L(e, \phi) \, dA \cos(e) \, d\Omega(r), \tag{1.1}$$

where r is the distance between the plane surface element dA and the observing instru-
ment, L is the radiance of the surface element, also known as (specific) intensity or bright-
ness, e is the angle between the surface normal and the direction to the instrument, ϕ is
the azimuthal angle of this direction in the plane of the surface, and $d\Omega$ is the scattering
solid angle, i.e. the solid angle of the instrument's aperture seen from dA. Because the
power depends on the distance it is convenient to quantify the measurements in units of
radiance, which is invariant to distance in free space, i.e. when the power from the surface
element dA is equal to the power received by the instrument. The bidirectional reflectance
is defined as

$$r(e, \phi; i, \phi_i) = \frac{L(e, \phi)}{J(i, \phi_i)}, \tag{1.2}$$

where J is the collimated irradiance (power per unit surface area) incident to dA, i is the
angle of incidence, and ϕ_i is the azimuthal angle of incidence. Another quantity often used
in remote sensing is the bidirectional reflectance distribution function: $BRDF = \frac{r(e,\phi;i,\phi_i)}{\cos i}$.

1.2.1 Physical causes of mineral absorption

Mineral identification is based on characteristic absorptions in regolith grains or rock when sunlight traverses them before scattering in the direction of the instrument. A typical depth of light penetration for silicate material is in the order of 1 μm (King et al. 2004). The mechanisms of absorption are electronic processes, as well as vibrational, rotational, and free carrier transitions. The electronic processes are the crystal field effect, charge transfer absorptions, conduction band transitions, and color centers. The most typical transitions at visible and NIR are electron excitations, where a single electron is induced from a lower energy level to a higher one. Partial rotation and translation (lattice modes) occur at lower energies corresponding to longer wavelengths than NIR. When a photon is absorbed at some wavelength it causes heating of the material and possible an emission at a longer wavelength.

Isolated atoms have discrete energy states, whereas in a solid the wavefunctions of the outer electrons overlap. This results in splitting of the energy levels so that there are several energy states which are close to each other. The energy levels of shared electrons may become smeared over a range of values and form an energy band, therefore mineral absorption bands are much broader than absorption lines in e.g. stellar spectra. The bands are usually superimposed on a background continuum, which is caused by a wing of a larger absorption feature.

The depth of an absorption band depends, among other factors, on the grain size; at NIR wavelengths large grains have stronger absorption bands than small grains of the same material. There are more surface reflections in small grains and less absorption due to internal paths in the grains where photons are absorbed according to Beer's law

$$I = I_o e^{-\kappa_s s}, \tag{1.3}$$

where I and I_o are the intensity of light exiting and entering the grain, respectively, κ_s is the absorption coefficient[1], and s is the distance travelled inside the grain.

The band depth increases as a function of grain size until it reaches a maximum value and then starts decreasing due to the effect of first reflections. In mid-infrared wavelengths (3.0 to 30 μm) absorption coefficients are typically larger and surface reflections are more dominant than in visible or NIR and the grain size effect may have an opposite trend at some wavelengths but not on others.

Crystal field effect

Crystal field effect occurs in minerals which contain transition elements. Their unfilled 'd' orbitals have identical energies in isolated atoms but split in a crystal. Since the crystal field splitting (energy separation between 'd' orbitals) varies from mineral to mineral, absorption features can be used to identify the mineral. Even the same ion (e.g. Fe^{2+}) produces slightly different depth, shape and positions of absorption bands depending on the physical properties of this ion's environment. The energy levels, which determine the possible wavelengths of the absorption, depend on i) the type of ion and ligands (surrounding anions treated as point negative charges), ii) symmetry of the site within the crystal, and

---

[1]This is related to the wavelength λ and the imaginary part of the complex index of refraction n as $\kappa_s = \frac{4\pi \Im n}{\lambda}$.

iii) the metal-ligand inter-atomic distance. The strength of the absorption band depends on i) the valence state of the transition element ion, ii) the amount of the ion, iii) symmetry of the site, iv) the compositional properties of the neighboring ligands and ions, and v) physical properties, e.g. closeness to the grain surface. Especially, minerals bearing iron produce prominent features in the NIR which can be used for mineral identification. On the other hand, the partly unfilled shells of rear Earth ions have deep-lying electrons, whose energy levels remain largely unchanged in a crystal field, thus their absorptions do not vary between different minerals (Hapke 1993, King et al. 2004, Clark 1999).

Charge transfer

A charge transfer absorption is an interelement transition where the absorption of a photon causes an electron to move between ions of different elements, ions of the same element in a different valence state, or between ions and ligands. The absorptions are hundreds of times stronger than in the crystal field effect and occur in the ultraviolet with wings extending to the visible wavelengths. Charge transfer absorptions cause the red color of iron oxides (King et al. 2004, Clark 1999).

Conduction bands

In some minerals there are two main energy levels for electrons to occupy (Hapke 1993, Clark 1999). In the band model of electrons in a solid, the highest energy band where all electron states are occupied is called the valence band; its electrons are located on a discrete ion or atom, whereas the higher energy levels of the conduction band may be partially or completely empty, and its electrons can move freely about the solid lattice. The valence electrons are binding the atoms or ions together in the mineral. The energy gap (band gap) between the valence and conduction bands determines the maximum wavelength of electromagnetic radiation that can excite an electron from the valence band to the conduction band. The band gap of some solids corresponds to the photon wavelengths in visible and NIR; these solids are typically semiconductors, whose band gap is only a tenth of a typical dielectric substance (insulator). The detector of the SIR instruments is based on this property of semiconductors (see Section 2.1).

Color centers

Most rock forming minerals suffer from lattice imperfections: vacancies, interstitials (an extra ion forced between the space between ions), and substitutional impurities (replacements of ions with different species). These imperfections may produce discrete energy levels in some minerals. If an excess charge is accompanied by the imperfection, an electron can orbit a positively charged imperfection, or a hole a negatively charged one. In this type of system, called a color center, an electron or a hole can jump to a higher energy level causing an absorption band, usually in the visible or NIR (Hapke 1993, Clark 1999).

Vibrational processes

The bonds in a crystal lattice are vibrating in specific frequencies depending on the mass of the vibrating atom and the strength of the bond. Minerals carrying the hydroxyl ion

(OH⁻) may have absorptions near 1.4 μm, near 1.9 μm, and near 2.3 μm. The broad absorptions of water ice near 1.5 μm and 2.0 μm are a consequence of multiples of the basic frequency of the hydrogen bonds. While the crystal structure of ice is hexagonal, these bonds are orientationally disordered, which broadens the bands (Clark 1999).

1.2.2   Bidirectional reflectance

There are many kinds of reflectances (diffuse scattering of light into many directions by a geometrically complex medium) depending on the geometry and set-up of a measurement or an observation. While in reality all measured reflectances are biconical, i.e. neither the source nor the detector is perfectly directional or perfectly diffuse, in many real-life remote sensing situations the sunlight can be assumed to be collimated, and the field of view of the detector can be assumed to be relatively small, so that bidirectional reflectance is a good approximation (Hapke 1993). Another reflectance, the directional-hemispherical reflectance, is better known as the (plane) albedo, commonly used in astrophysics.

When a lunar spectrum is observed it is a combination of the effects of incident solar radiation, properties of the surface, and the illumination geometry, which has an effect on the intensity of the observed spectrum and also on its shape, for instance by changing its continuum slope. There are five physical processes affecting the light incident on a regolith surface: i) reflection, ii) absorption, iii) diffraction, iv) scattering by subwavelength and wavelength size particles, and v) refraction. In addition, there are coherence effects between numerous wavefronts generated by multiple interactions between particles of different shapes and different geometric scales; the most important coherence effect is the opposition spike at small phase angles. In order to compare spectra observed at different photometric conditions a correction needs to be applied. There are three classes of models for bidirectional reflectance: i) empirical, ii) geometrical optics, and iii) radiative transfer models. The parameters of empirical models often do not have a physical meaning but on the other hand the number of parameters is small compared to geometrical optics and radiative transfer models.

The simplest bidirectional-reflectance function is the Lambert's law, which assumes that brightness is independent of the angle of emergence and the azimuthal direction of incidence and scattering:

$$r_L(i) = \frac{1}{\pi} A_L \cos i, \qquad (1.4)$$

where r_L is the Lambert reflectance and A_L is the Lambert albedo. This law provides a reasonable adequate approximation for high-albedo surfaces. In the interpretation of experimental data a quantity commonly used is the reflectance factor, which is the bidirectional reflectance of the observed surface compared to that of a Lambertian surface:

$$REFF(e, \phi; i, \phi_i) = \frac{r(e, \phi; i, \phi_i)}{r_L(i)}, \qquad (1.5)$$

where the Lambert surface is perfectly diffuse ($A_L = 1$).

Another empirical function is the Minnaert reflectance r_M:

$$r_M(i, e) = A_M (\cos i)^\nu (\cos e)^{\nu-1}, \qquad (1.6)$$

15

where A_M and v are empirical constants not related to any physical properties in an obvious way; furthermore, their values do have a dependence on the geometry. Minnaert's reflectance can be used as an approximation for many surfaces but for a limited range of angles and it breaks down completely at high angles of emergence.

Treatment of scattering of light from a dispersed particulate medium is well established by Chandrasekhar's radiative transfer theory, but no general theory exists for a surface with particles packed close together (Hapke 1981). However, several approximate analytical or semi-empirical expressions are available. The bidirectional reflectance of a semi-infinite, particulate medium where light is scattered only once and there are no sources within the medium, can be analytically calculated from the radiative transfer equation assuming that the scatterers are isotropic. The result is the Lommel-Seeliger law:

$$r_{LS}(i,e) = \frac{w}{4\pi} \frac{\cos i}{\cos i + \cos e},\tag{1.7}$$

where w is the single scattering albedo defined as $\frac{\kappa_s}{\kappa_a + \kappa_s}$, where κ_s is the scattering coefficient and κ_a is the absorption coefficient of the medium (Section 1.2.1); the single scattering albedo w is the probability that a photon survives an interaction of a single particle. This law can be used for low albedo bodies in the solar system at moderate to high phase angles, and it can be generalised to include nonisotropic scatterers: $r'_{LS}(i,e,\alpha) = r_{LS}(i,e)P(\alpha)$, where P is the phase function and α is the source-surface-observer phase angle; for instance $P = 1$ for isotropic scattering, $P(\alpha) = 1 + \cos\alpha$ for back scattering, $P(\alpha) = 1 - \cos\alpha$ for forward scattering and $P(\alpha) = \frac{3}{4}(1 + \cos^2\alpha)$ for Rayleigh scatterers. These ideal cases are often not accurate enough; Hapke (1963) proposed a phase function for the Moon:

$$P(\alpha) = \frac{4\pi}{5} \left(\frac{\sin\alpha + (\pi - \alpha)\cos\alpha}{\pi} + \frac{(1 - \cos\alpha)^2}{10} \right).\tag{1.8}$$

Taking into account multiple scattering with the simplifying assumption that it is isotropic the isotropic multiple scattering (IMSA) bidirectional reflectance becomes (Hapke 1981)

$$r_{\text{IMSA}}(i,e,\alpha) = \frac{w}{4\pi} \frac{\cos i}{\cos i + \cos e} \left[(1 + B(\alpha))P(\alpha) + H(i)H(e) - 1 \right],\tag{1.9}$$

where the multiple scattering part, the H function (an approximation of the Chandrasekhar's H function) is $H(i) = \frac{1 + 2\cos i}{1 + 2\gamma\cos i}$, where $\gamma = \sqrt{1 - w}$. A better approximation, which must be used if $r_{\text{IMSA}} > 0.9$ can be found in Hapke (2002). For small phase angles the phase function has to be multiplied by a coherent interference factor, which is relevant to medium where particles are close to each other:

$$B(\alpha) = \frac{B_0}{1 + \frac{1}{h}\tan\left(\frac{\alpha}{2}\right)},\tag{1.10}$$

where B_0 is the amplitude of the shadow hiding opposition effect and $h = (\kappa_a + \kappa_s)d\ln\frac{1-p}{2p}$, where d is the mean particle radius, and p is the filling factor.

The anisotropic multiple scattering (AMSA) model by Hapke uses a more complicated function to replace the H function with a more isotropic multiple scattering term. A further modification, the Lumme-Bowell model has a more complicated P function
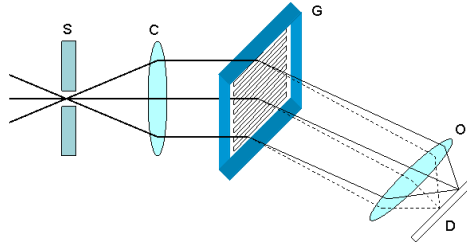
Figure 1.1: General scheme of a spectrometer with a slit (S), collimator lens (C), grating (G), objective lens (O) and detector (D). The spectrometer is usually equipped with a front-end optics system. The grating in this figure is a transmission grating but a more common type used is a reflection grating. When differential diffraction is used, the grating is replaced by a prism.

comprising of three parts: scattering from individual particles, shadowing and surface roughness. A photometric function developed by Shkuratov and Akimov is discussed in Section 5.4.

1.3   Spectrometers

The word *spectrometer* in this work refers to an optical instrument consisting of a slit, followed by a prism, grating or interferometer, and a photoelectric photometer to measure radiant intensities at various wavelengths (Fig. 1.1). The word spectrometer is also used for other types of instruments, for example in mass spectrometry where the abundance of elements is measured as a function of atomic number. The spectrometer in optical instrumentation is based on the physical principle of either interference or differential diffraction. Interference based spectrometers have diffraction gratings or interferometers whereas differential refraction relies on a prism. The most important parameters in designing an optical spectrometer are the intended wavelength range, and the resolving power, i. e. how narrow and fine-detailed spectral features are to be observed with the instrument.

For prism spectrometers, typical values of resolving power R, that is wavelength divided by the least resolvable wavelength difference ($R = \frac{\lambda}{\Delta\lambda}$), is in the order of 10^4. The

prism materials available set limits to the wavelength range, and they are not used at far infrared or below 200 nm. The linear dispersion, that is the difference in linear distance on the detector corresponding to a difference in wavelength, is inversely proportional to the wavelength, so the wavelength spacing on the detector is not linear. The property of a prism is to introduce astigmatism, an aberration where rays from an off-axis object have different focal lengths depending whether they are on the plane containing the object and the optical axis (tangential plane) or in the plane perpendicular to it (sagittal plane). Due to astigmatism an off-axis point source is imaged as an elongated ellipse. The apex angle of the prism which gives the minimum astigmatism is not the same as the apex angle giving the best spectral resolution, thus a trade-off between astigmatism and spectral resolution has to be made (Kitchin 1984, Hecht 2002).

For technical reasons gratings have between 100 and 1000 slits or grooves per millimeter. The resolving power can be calculated as the product of the number of grooves or slits multiplied by the order of diffraction selected, typically the resolving power of grating spectrometers is between 10^3 and 10^5. The linear dispersion of a grating spectrometer is almost constant, which offers the advantage of having a linear wavelength spacing on the detector. The principal disadvantage of a grating design is that a significant amount of light is lost to spectra of different orders of diffraction than the one used by the detector.

For reflection gratings the disadvantage of losing light to other orders of diffraction can be minimised by blazing: individual mirrors which constitute the reflection grating are angled so that they concentrate the light into a single solid angle (Hecht 2002). Furthermore, by curving the reflection grating to that of an optical surface the grating itself can act as a collimator or objective lens, making the design simpler. For instance, an optical surface called the Rowland circle has the same radius as the curvature of the grating, and the slit and the spectrum are on that circle. Undesired effects are often superimposed on the ideal grating spectrum. They may be caused by overlap from higher or lower orders, imperfections in the grating, or secondary maxima associated with the principal maximum. The overlap can be blocked by employing suitable filters in different areas before the detector. The secondary maxima are very low for gratings with more than a few tens of grooves, and their effect may only be seen in the wings of an instrument response to a line spectrum. Reflection grating spectrometers are the most common in astronomical use (Kitchin 1984).

Other important types of spectrometers exploiting the interference effect are the Fourier transform spectrometer and the Fabry-Perot interferometer. In the Fourier transform spectrometer light is split into two paths, like in the famous Michelson-Morley experiment to measure the speed of light in perpendicular directions, and the path length difference of the two rays is modified by moving a mirror. The output is the real part of the Fourier transform of the spectral intensity function of the source, hence the name of this class of spectrometers. The resolving power of Fourier transform spectrometers is in the order of 10^6. To sample the Fourier transform of the spectrum the mirror should be moved in steps, which degree depends on the start and the end wavelengths, so that the step size is larger at longer wavelengths. The Fourier transform spectrometer is common in infrared applications. The other common class, the Fabry-Perot interferometer, instead utilizes multiple beam interference and has two parallel partially reflecting surfaces with a cavity between them. Rays arriving at a nonzero incidence angle are partially reflected inside the cavity between the surfaces, and partially transmitted through the surface as parallel rays.

All rays at a given wavelength incident on the partially reflecting surface will combine, past the objective lens, in a circular fringe of uniform irradiance. Different wavelengths produce circular fringes of different radius and the result is a very high resolving power (up to $R = 10^7$). Fabry-Perot interferometers are used in astronomy for detailed studies of spectral lines (Kitchin 1984, Hecht 2002).

The resolving power is a fundamental parameter indicating which spectrometer has the best capabilities for seeing the details of a spectrum. When comparing different spectrometer systems a more useful figure than the resolving power alone is the product of the resolving power and the light gathering power, or etendue: $R \times (\tau A \Omega)$, where τ is the total optical transmission, A is the area of the collimator entrance or the dispersing element, whichever is smaller, and Ω is solid angle of the entrance slit of the collimator; these are calculated for the SIR instrument in Section 2.2. Typically the product of the resolving power and the etendue is highest for Fabry-Perot interferometers, intermediate for grating spectrometers, and lowest for prism-based instruments.

1.4 Spacecraft experiments in the NIR

NIR lunar observations from spacecraft were carried out by the Galileo mission during two flybys in 1990 and 1992, the Clementine mission in 1994, the SMART-1 mission in 2005-2006 as well as the ongoing Kaguya mission. With just two flybys Galileo was able to map, although at low spatial resolution, 20% of Moon's farside. The Clementine mission used a NIR camera with six filters, and they mapped the Moon with an average spatial resolution of 200 m during a two and a half month long mission. The SMART-1 spacecraft carried the first high spectral resolution NIR spectrometer on a lunar orbit. The instrument called SIR was a point spectrometer with 256 channels in the NIR covering about one sixth of the lunar surface with a footprint size of 3 km or less. The maximum gap in the data between orbits was 60 km in the east-west direction.

Limitations of ground-based observations

The most obvious reason to deploy spacecraft is that the farside of the Moon is not visible from the Earth; another reason is to avoid Earth's atmosphere. High altitude telescopes have been able to observe NIR spectra, avoiding part of the atmospheric absorption. The spatial resolution achieved is between 3 and 10 km. The main obstacle in telescopic observations is often small-scale atmospheric turbulence. Systematic atmospheric variations can be overcome by making comparative observations by pointing the telescope at a standard area, for example the Apollo 16 landing site, and then dividing the observed spectrum with the observed reference area spectrum. However, a further disadvantage is the difficulty in reproducing a precise pointing of the telescope on a reference location (Pieters and Pratt 2000).

1.4.1   The Galileo / NIMS instrument

The first imaging spectrometer observations of the Moon from a spacecraft were carried out during the 24 hour flyby in 1990 by an instrument called Near-Infrared Mapping Spectrometer (NIMS), an imaging spectrometer with a reflection grating and a 17 pixel detector with 15 InSb and two silicon photovoltaic diodes across the focal plane of the spectrometer (McCord et al. 1994). Images were captured by a moving secondary mirror in the front-end optics in one direction, and the whole instrument platform in a direction perpendicular to the instrument scanning plane. The spectral range of 0.7 μm to 5.2 μm is achieved by moving the grating in 24 steps resulting in 408 adjacent and partially overlapping channels with spatial resolution between 170 km and 630 km, see Table 1.1. The mechanical movement of the scanning platform was not uniform, so a depatterning autocorrelation technique was developed for removing jitter.

Only relative spectra were obtained from the collected data because the ground calibrations were not accurate enough due to changes in the detector and electronics. After offset adjustment, dark reduction, and a photometric correction using Minnaert's function (Equation 1.6), the conclusion was reached that the NIMS instrument was indeed working, and that the 1 μm and 2 μm absorption bands of mafic minerals could be seen in a few locations, as expected from ground-based telescopic observations. For radiometric inflight calibration there was a blackbody radiator onboard, which consisted of a mosaic of hexagonal honeycomb cavities painted with an infrared black paint. The radiator was heated to 315 K and it provided a known radiance which could be used for calibration purposes at wavelengths longer than 2.5 μm. The photometric calibration target was a diffuser plate made of aluminium, which reflected solar radiation and had been calibrated for a variety of incidence angles over the spectral range of 0.3 to 5.2 μm.

The second flyby in 1992 lasted 12 hours, during which relative spectra from the north polar regions were observed with a spatial resolution of 60 km at best, with data suffering from jitter again. The combined data from the two flybys covered 20% of the farside of the Moon with a spatial resolution between 200 and 500 km (Carlson et al. 1993).

Table 1.1: Parameters of the NIMS instrument onboard Galileo (Carlson et al. 1992).

Type of instrument	Grating imaging spectrometer
Wavelength range	0.7 μm - 5.2 μm
Grating	flat field diffraction grating, 39 lines/mm
Spectral resolution	25 nm or better
Angular resolution	0.5 mrad $\times$ 0.5 mrad
Focal length	800 mm
f-ratio	3.5
Detector	InSb and Si photovoltaic diode array
Dynamic range	0 - 1023 digital number units
Total mass	18 kg
Power	max. 13 W
Onboard calibration	Dark background
	Photometric calibration target
	Radiometric calibration target

1.4.2   The Clementine cameras

The Clementine mission's main scientific target was to investigate a near-Earth asteroid, while the Moon represented an opportunity to demonstrate the performance capabilities of the instruments. After a two-month mapping phase Clementine was heading towards the target asteroid when a software error caused all of the attitude-control propellant to be exhausted. Clementine never reached its primary target, but it did provide a global multispectral map of the Moon, the first geological investigation of the poles and the farside as well as the first view of the global topographic figure of the Moon. The Clementine mission covered more than 99% of the surface with a spatial resolution between 100 m at periselene and 400 m at the poles (Le Mouélic et al. 1999a) from a polar elliptical orbit of 400 km to 450 km altitude (Edwards et al. 1996). It did not carry spectrometers, but two cameras with filters, one for NIR and the other for visible and ultraviolet wavelengths. The spectral bands covered by the NIR camera are given in Table 1.2. The UVVIS camera had a broad band mode and a filter wheel for selecting from five narrow band channels (Nozette et al. 1994).

There were difficulties in calibrating the NIR camera on a global scale because of variations in the dark background of the CCD images during the mission, and there were also uncertainties in the gain values. A drifting additive offset in the gain values, which varied throughout an orbit and from orbit to orbit was in the worst cases as much as 100% compared to the lunar signal (Lucey et al. 1997). The photometric correction used a linear combination of Lambert and Lommel-Seeliger laws (Equations 1.4 and 1.7) where the proportionality coefficient of the two parts of the combination is a third order polynomial of the phase angle with three empirical constants (Shkuratov et al. 2001). The first scientific studies used relative images, that is one NIR channel divided by another NIR channel, and focused on localized targets (Le Mouélic et al. 1999a). Absolute reflectance were obtained by using Earth-based telescopic spectra as ground truth. The latest global calibration of the Clementine cameras was completed in 2007 (Combe et al. 2008). The final NIR images have a noise level of 1% and the UVVIS images 0.5% (Cahill et al. 2004).

One of the applications of the UVVIS data set has been the production of global maps of iron oxide and titanium oxide content (Lucey et al. 2000). The NIR channel 1500 nm, which is representing the continuum on the longer wavelength side of the iron absorption band seen in visible and NIR, helps to refine the iron content maps by discriminating between maturity effects on the spectrum and its slope from the effect of the iron composition (Le Mouélic et al. 1999b).

1.4.3   The Kaguya / LISM instrument

The ongoing Japanese Moon mission Kaguya was launched in September 2007, reaching the Moon a month later, and it is now on a 100 km high polar orbit. It carries an instrument which is a combination of cameras and a spectrometer; the subinstruments of the Lunar Imager/Spectrometer are a terrain camera, a multiband imager and a spectral profiler. They share some of the power supply, control and data handling electronics. The terrain camera, a stereo pair with spatial resolution of 10 meters, and the multiband imager share the same mechanical structure. The five visible and four NIR channels of the multiband

Table 1.2: Parameters of the NIR camera as well as the center wavelengths of the UVVIS camera onboard Clementine (Nozette et al. 1994).

Type of instrument	Camera, 6 bandpass filters
Center wavelengths	1.1, 1.25, 1.5, 2.0, 2.6, 2.78 μm
Filter bandwidths	30 nm, 60 nm for 2.78 μm filter
Field of view	5.6° × 5.6°
Focal length	96 mm
Detector	InSb 256 × 256 pixel CCD
Total mass	1.9 kg
Power	11 W
UVVIS camera wavelengths	415, 750, 900, 950, 1000 μm
UVVIS camera bandwidths	20, 5, 15, 15, 15 nm

imager provide nine-color images with spatial resolution of 20 to 60 m for mapping the global mineral distribution. The spectral profiler (see Table 1.3) is a visible to NIR point spectrometer with a wavelength range between 500 and 2600 nm, covered by 300 channels and three separate detectors to cover the whole range. For inflight calibration there are halogen lamps to check the stability of wavelengths as well as the signal levels. The data from the multispectral imager is used for cross-calibration as well (Ohtake et al. 2008).

Table 1.3: The main properties of the spectral profiler as part of the LISM instrument on board Kaguya (Haruyama et al. 2008).

| Type of instrument	Visible and NIR point spectrometer
Wavelength range	0.52 μm - 2.6 μm
Grating	plane gratings
Spectral sampling	6 to 8 nm
Angular resolution	4.0 mrad
Focal length	125 mm
f-ratio	3.8
Detectors	128 pixel Si photo diode array at 520-960 nm
	128 pixel InGaAs photo diode array at 900-1700 nm
	128 pixel InGaAs photo diode array at 1700-2600 nm
Dynamic range	0 - 2^{16} digital number units
Total mass	10 kg
Inflight calibration	halogen lamps
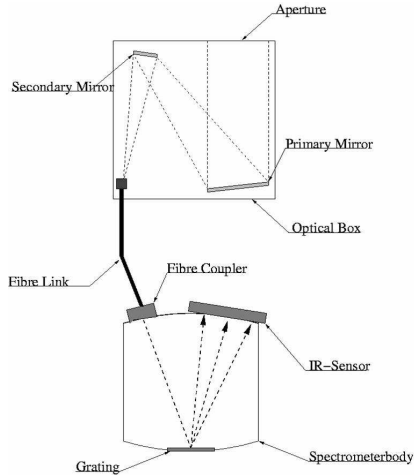
Figure 1.2: A schematic view of the front-end optics (upper part) and sensor head parts (lower part) of the SIR instrument. The two parts are connected by an optical fiber. A separate electronics box is located inside the spacecraft.

1.4.4   Missions carrying the SIR instruments

The SMART-1 infrared spectrometer (SIR) was built by the Max Planck Institute for Solar System Research as a technology demonstration. It is a light weight point spectrometer operating in the NIR equipped with a photodiode array detector with 256 pixels, and it covers the wavelength range from 0.9 μm to 2.4 μm. The main components of the SIR instrument (see Fig. 1.2) are 1) the front-end optics, 2) the sensor head, which contains a slit, core optics including a diffraction grating, and a detector, and 3) a separate electronics unit, which is located inside the spacecraft. The properties of the instrument are listed in Table 1.4. An upgraded version of the SIR instrument with the same basic design, but including various component improvements, has been built and was launched on Chandrayaan-1. This section introduces these two missions; the SIR and SIR-2 instruments are discussed in more detail in Section 2.1.

The SMART-1 mission

The SMART (Small Missions for Advanced Research and Technology) missions are designed to test new technologies to be used on future ESA missions (Racca et al. 2002). SMART-1 was launched in September 2003 and it took 16 months for the experimental ion propulsion system to slowly accelerate the one cubic meter spacecraft and to reach the Moon on a spiralling orbit, which was calculated to utilize the gravitational pull of the Moon during lunar resonances. The spiralling orbit took the spacecraft and its instruments

Table 1.4: The main properties of the SIR instrument (Mall et al.   2004). Differences between the SIR and SIR-2 instruments (SIR-2 Team 2007) are indicated.

Type of instrument	Grating NIR point spectrometer
Wavelength range	0.9 μm - 2.4 μm
Grating	concave reflection grating, 179 lines/mm
Spectral sampling	about 6 nm
Rayleigh resolution	about 18 nm
Angular resolution	1.1 mrad (SIR), 2.2 mrad (SIR-2)
Focal length	180 mm
f-ratio	2.5
N.A. of optical fiber	0.2
Detector	Hamamatsu InGaAs G8180-256W (SIR)
	Hamamatsu InGaAs G9208-256W (SIR-2)
Detector cooling	passive (SIR)
	passive, active stabilization (SIR-2)
Dynamic range	0 - 2^{16} digital number units
Exposure time	Selectable 0.5 - 503 ms (SIR)
	Selectable 0.1 - 628 ms (SIR-2)
Total mass	2 kg (SIR), 3 kg (SIR-2)
Power	max. 5.4 W (SIR), max. 11 W (SIR-2)

through the Earth's radiation belts about 150 times. The science phase lasted one and half years and the mission ended in a planned impact on the nearside. Despite the small mass allowed for the instruments there were three instruments for lunar surface science, as well as two plasma instruments and two technology experiments (see Table 1.5). One of the instruments was the NIR point spectrometer SIR (Table 1.4). The other surface science instruments besides SIR were D-CIXS (Demonstration of a Compact Imaging X-ray Spectrometer) and AMIE (Advanced Micro-Imager Experiment). The D-CIXS spectrometer operated in the energy range from 0.5 keV to 10 keV with a surface resolution of 30 km. It produced the first global view of the lunar surface in X-ray fluorescence, and made the first remote detection of calcium from lunar orbit (Grande et al. 2007). The AMIE camera had a resolution of 30 m per pixel and a field of view of 5.3°×5.3°. The 1024×1024 pixel CCD was divided into regions with no filter, 0.75 μm filter, 0.92 μm filter, and 0.96 μm filter. The AMIE camera was used to image selected sites on the Moon, including the north and south poles to look for craters in permanent shadow. During 1150 orbits of the SMART-1 mission the point spectrometer SIR observed 18% (as per Appendix A) of the lunar surface with spatial resolution of 3 km up to at best 330 m at the lowest point of the elliptical orbit. The typical observing mode was nadir pointing. The Apollo landing sites and several other targets have also been observed in a target-tracking mode where the whole spacecraft was turned to point to a specific location on the surface.

Table 1.5: The European SMART-1 mission. The three instruments D-CIXS, SIR and AMIE were designed for lunar surface studies (Foing et al. 2006).

Mission objective	technology demonstration
Total mass	350 kg
Scientific payload	19 kg
Orbit type	polar, 300-3000 km
Revolution period	about 16 h
Launch	September 2003
Science phase start	March 2005
Mission end	September 2006
Instrument	Target of study
EPDP	plasma surroundings
SPEDE	electron plasma, dust
KATE	high rate telecommunication
RSIS	spacecraft position
D-CIXS	elemental composition
SIR	mineralogical composition
AMIE	chemical composition, maturity

The Chandrayaan-1 mission

The Chandrayaan-1 mission, launched in October 2008 is the first Indian planetary exploration mission. The scientific goal is to improve the understanding of the origin and evolution of the Moon. For that purpose the Moon will be mapped in high resolution to investigate minerals and chemical compositions, as well as to acquire topography data for 3D maps. The payload allows the direct estimation of the elements Fe, Ti, Al, Mg, Si and Ca with a spatial resolution of 20 km, which is an improvement compared to previous elemental maps. The nature of transport of water molecules and other volatiles will also be investigated. The mission parameters are given in Table 1.6. SIR-2 on board Chandrayaan-1 will be observing the Moon at an altitude of 100 km, much lower than the SMART-1; this improves the spatial resolution of this point spectrometer to 220 m. Also an imaging infrared spectrometer, the Moon Mineral Mapper (M3), will be on board Chandrayaan-1. M3 has a field of view of 40 km and a spatial resolution of 70 m/pixel with a spectral range of 0.43 to 3.0 μm. The M3 spectrometer has one spherical mirror and a convex grating; a three mirror telescope is used as the front end optics. The instrument provides a spectral resolution of 15 nm with a spectral sampling of 10 nm (Pieters et al. 2006, Green et al. 2007).

Table 1.6: Indian Moon mission Chandrayaan-1 (Goswami et al. 2006). SIR-2, CIXS and SARA are contributions of ESA, MMM and Mini-SAR are from NASA, and RADOM from Bulgaria. Other instruments are from India. SIR-2 and CIXS are upgraded instruments from the SMART-1 mission.

Mission objective	high resolution selenological and chemical mapping	
Total mass	523 kg	
Scientific payload	55 kg	
Orbit type	circular polar, 100 km	
Revolution period	about 2 h	
Launch	October 2008	
Science phase start	January 2009	
Instrument	Target of study	Type of instrument
TMC	3D image of lunar surface	stereo camera, resolution 5 m
SIR-2	mineralogical composition	point spectrometer 920-2400 nm
MMM	mineralogical composition	infrared spectrometer
HySi	mineralogical composition	hyper spectral imager, 400-950 nm
HEX	volatile transport	20-250 keV spectrometer
LLRI	topography	laser ranging, resolution 5 m
Mini-SAR	polar water ice	radar
CIXS	chemical composition	low-energy X-ray spectrometer
SARA	solar wind sputtered atoms	sub-keV atom reflecting analyzer
	magnetic anomalies	
RADOM	energetic particle flux	radiation dose monitor
impactor	imaging of impact	video camera, radar altimeter
	trace gases in exosphere	mass spectrometer

2 The SIR instruments and their simulated response

The response of an instrument can be modelled based on the available data from the manufacturers of different parts of the instrument combined with measurements in a controlled laboratory environment. This model calculation can later be compared with real observations. Section 2.1 describes the operational concept of the SIR (SMART-1 infrared spectrometer) and SIR-2 (Spectrometer Infra-Red 2) instruments. A simulated response of these instruments to reflected sunlight from lunar surface is developed in Section 2.2. Possible noise sources are discussed in Section 2.3.

2.1 The SIR instrument family

The SIR instrument was developed by the Max Planck Institute for Solar System Research. It is partly based on a commercially available spectrometer from the Zeiss company, the Monolithic Miniature Spectrometer Module MMS NIR. It is a sealed and thermally stable system, which has an aberration corrected concave reflection grating attached on a glass body made of Suprasil 311 (synthetic quartz glass manufactured by flame hydrolysis of $SiCl_4$), and a photodiode array as the detector. A complete redesign of the commercial spectrometer was necessary to make it space qualified. A schematic figure of the instrument is shown in Fig. 1.2. The front-end optics (O-Box) was designed for the SMART-1 mission (Figs. 1.2, 2.1 and 2.2). The O-Box is connected to the sensor head part, which also includes the spectrometer body, by an optical fiber. The parabolic primary mirror has an off-axis design (Fig. 2.2) to avoid reduction in the aperture and to avoid chromatic errors. The purpose of the plane secondary mirror is to fold the light path and make the construction more compact in size.

Photodiodes are a usual choise of detectors at wavelengths between 1 and 6 μm and they are used in the visible range as well. The detector of the SIR instrument is a modified InGaAs G8180-256W photodiode array, which is extended to 2.4 μm instead of the typical 1.7 μm (see Table 2.1). A spectrometer based on such an extended InGaAs cut-off wavelength has been flown before on European Space Agency's ENVISAT satellite in 2002 (Hoogeven et al. 2001) for the spectrometry of Earth's atmosphere as well as on the Japanese Hayabusa, which was observing asteroid Itokawa in 2005 with an InGaAs detector, whose maximum wavelength was 2.1 μm (Abe et al. 2006). The roundish structure in the sensor head part of the SIR instrument provides a radiation protection for the detector, which is equivalent to 14 mm of aluminium (Mall et al. 2004). The housing of the detector is open to space during the mission to ensure a pressure balance and to avoid
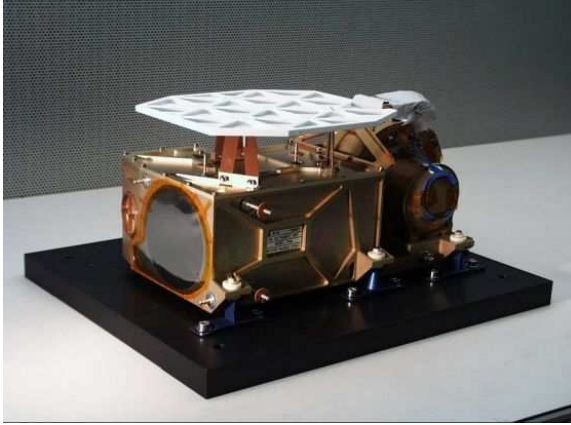
Figure 2.1: The O-Box and sensor head of the SIR instrument. A white radiator is located on top of the O-Box. A cooling band connects the radiator to the cooling console of the detector. The quartz body is inside a round aluminium housing, which is shown on the right. The plate where the sensor head is mounted (behind, right of the O-Box) is part of the structure of the O-Box.
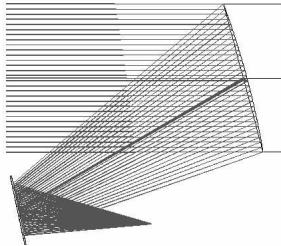

Figure 2.2: Optical scheme of the front-end optics of the SIR and SIR-2 instruments (P. Wawer, personal communication 2008). Light incoming through the open aperture (from left) is reflected from the parabolic mirror having a radius of curvature of 360 mm and diameter 72 mm. The distance between the primary and the secondary mirrors is 124 mm, and the distance from the 22.6 mm diameter secondary mirror to the entry of the optical fiber is 49 mm.

possible condensation of the gas that would have been used inside the detector housing of the equivalent commercial spectrometer.

Incoming light with high enough energy, or even thermal excitation, produces electron-hole pairs in a semiconductor material (see the subsection about conduction bands in Section 1.2.1). The positively charged ion that is left behind when an electron is excited has a vacancy to which an electron from a neighboring ion can tunnel. These holes behave like positively charged particles; thus the intrinsic conductivity of a semiconductor is caused by both electrons in the conduction band and by holes. This conductivity has been enhanced by adding impurity atoms which have either more or less electrons than is required by the lattice. The operation of the photodiode is based on a junction between two oppositely doped zones in the semiconductor material: the n-type zone has a surplus of electrons compared to the need of the bonds, and the p-type zone has a deficiency (Fraden 1996). The p-zone is in a higher potential than the n-zone; this potential difference can be either increased or decreased by connecting the junction into an external potential. The number of charge carriers in the photodiode increases as the intensity of incident light is increased. When the n-zone is connected to a positive voltage (reverse biased junction) the potential difference in the junction is increased and electrons start flowing towards the positive voltage and holes to the opposite direction with the current being a function of the number of incoming photons. This current is transformed to a voltage by the amplifier circuit shown in Fig. 2.3. The sensor consists of, in addition to the InGaAs photodiode array and the charge amplifier array for each pixel, an offset compensation circuit, a shift register and a timing generator. During operation, the detector is cooled to a temperature of $-50°C$ to $-70°C$ by passive cooling with a radiator connected to a cooling console by a cooling band; the cooling console is thermally decoupled from the rest of the sensor head.

Table 2.1: Main characteristics of the Hamamatsu G8180-256W (Hamamatsu 2000) and G9208-256W (Hamamatsu 2003) sensors given by the manufacturer.

Number of pixels	256
Spectral range	0.9 μm to 2.55 μm
Pixel size	50 μm $\times$ 250 μm
Pixel pitch	50 μm
Defective pixels	<5%
Peak sensitivity	at 2.3 μm
Photo response nonuniformity	< $\pm$10 %
Saturation charge	30 pC
Feedback capacitance of sensor	10 pF
Voltage range	$\frac{30 \text{ pC}}{10 \text{ pF}} = 3.0$ V

The only part of the instrument located inside the spacecraft is the electronics box. It consists of two subparts: a power supply unit and an instrument control unit (ICU), the latter contains a microprocessor/controller for command handling and health data transfer. The unit also has 16-bit analog-to-digital converters for the detector signals, and it handles the communication between the instrument and the spacecraft.
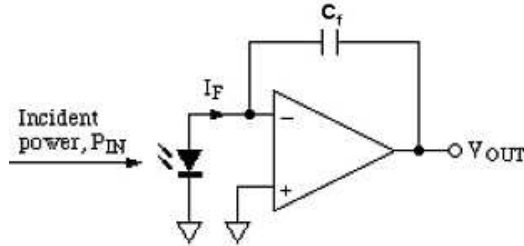
Figure 2.3: Equivalent circuit of a single pixel. Modified from (Hamamatsu 2000). Before an exposure starts the capacitor C_f is reset. Then, photocurrent I_f charges the capacitor and increases the output voltage of a charge amplifier. After the integration time the voltage V_{out} is read and the capacitor is reset again. The photodiode is connected to a bias voltage and the charge amplifier is connected to an amplifier reset voltage, which in the current design are the same (4.5 V).

SIR-2

The SIR-2 instrument uses the same operating principles as the SIR instrument. The radiator is located on top of the Sensor Head / Radiator Unit (SHRU), and it is larger than in SIR. The O-Box is not physically attached to the SHRU, but the three parts are separate as shown in Fig. 2.4. As a consequence, the optical fiber consists of two parts, one detachable between the O-Box and the SHRU and the other (inner optical fiber) permanently fixed in the SHRU. The entrance diameter of the fiber is twice that of SIR in order to increase the amount of light, and thus the field of view is 2.2 mrad compared to 1.1 mrad of SIR. The detector in the SIR instrument was passively cooled, and its temperature was not controlled in any other way; instead in SIR-2 the temperature of the detector (Hamamatsu's InGaAs 9208-256W) is stabilized by an active Peltier element. Furthermore, there is a heater for increasing the temperature of the cooling console to provide a suitable temperature range. Also the analogue electronics has been redesigned. The power consumption is twice that of SIR, almost 11 W, and the mass is 3 kg.

2.2 Response to reflected sunlight from lunar surface

The SIR instruments observe sunlight which is scattered by and reflected from the top few layers of grains in the lunar regolith down to depths of a few micrometers. In modelling the instrument response the first step is to estimate the physical input signal. The irradiance of the incoming sunlight is given by a model which deviates slightly from a black body, see Fig. 2.5. The amount of light incident to the instrument depends on the
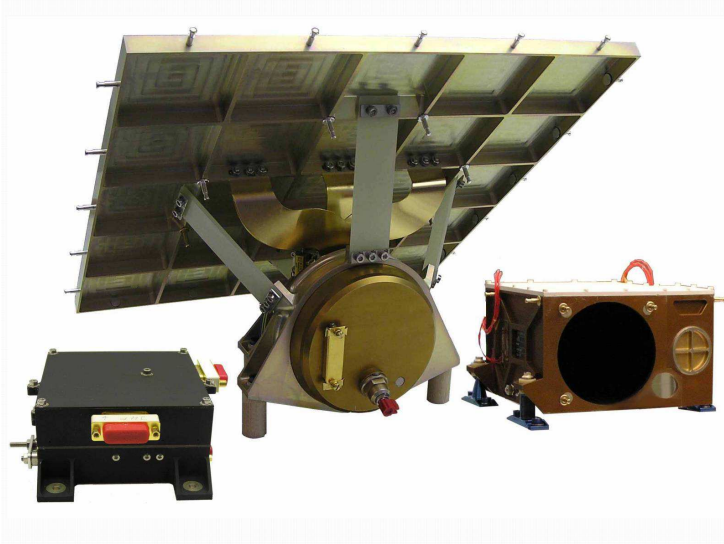
Figure 2.4: The three components of the SIR-2 instrument: Sensor Head / Radiator Unit (middle), O-Box (right), and E-Box (left). The dimensions of the SHRU are 227 mm × 320 mm × 249 mm and the size of the O-Box is 199 mm × 161 mm × 93 mm.

surface properties. A simple model is assumed for the albedo of the Moon. (I. Sebastian, personal communication 2005):

$$a = \begin{cases} 0.0572 + 0.0892\lambda, & 0.5 \leq \lambda < 1 \\ 0.125 + 0.0214\lambda, & 1 \leq \lambda \leq 2.5 \end{cases} \tag{2.1}$$

where λ is the wavelength in μm. The model gives an average reflectance factor based on the data in Neukum et al. (1991). The model 2.1 is compared to the global average of Clementine mission (see Section 1.4.2) data and two Luna soil samples in Fig. 2.6. In calculating the radiance a perfectly diffuse Lambertian surface is assumed for simplicity ($A_L = 1$ in Equation 1.4). Hence, applying Equations 1.2 and 1.5 the radiance from the surface taking into account the albedo of the surface is

$$L = Ja\frac{1}{\pi}, \tag{2.2}$$

where J is the solar irradiance.

Applying Equation 1.1 and taking into account the invariance of radiance the power received by the instrument is
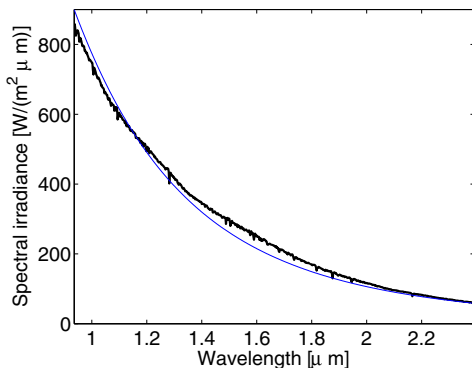
$$P = L\Delta\lambda A\Omega, \tag{2.3}$$

31

Figure 2.5: The ASTM solar irradiance standard at 1 AU from the Sun (thick line) (ASTM 2000) and the black body approximation of a 5900 K Sun (thin blue line).

where $\Delta\lambda$ is the spectral resolution, A is the area of the aperture of the instrument, and Ω is the solid angle of the field of view of the instrument when the surface element is integrated over the whole footprint area. The spectral sampling, or the average difference of center wavelengths between the 256 pixels of the SIR instruments is 6 nm, which is used as the value for $\Delta\lambda$ in this calculation. A small fraction of light is lost in the O-Box due to reflection from the two mirrors (Fig. 2.7). Considering the power, which is received at the beginning of the optical fiber, the area to be used in equation 2.3 is the cross section of the fiber. In this case the *receiving angle* Ω is the maximum observable solid angle seen from the focal point at the beginning of the fiber. The solid angle is calculated as

$$\Omega = \int \int \sin\theta d\theta d\phi \rightsquigarrow \Omega = \pi \sin^2 \Theta = \pi \sin^2 \frac{D}{2f}, \tag{2.4}$$

where Θ is the angle at which the radius of the primary mirror is observed, D is the diameter of the primary mirror, and f is the focal length. Using values $D = 72$ mm and $f = 180$ mm (as per Table 1.4), the value of the solid angle is $\Omega = 0.124$ sr. The radius of the optical fiber is $r = 200$ μm, which gives a surface area of 1.26×10^{-7} m^2. Using these values the calculated spectral density of power received at the beginning of the optical fiber is shown in Figure 2.8.

Simulations show that the actual diameter of the image at the focal point of the O-Box optics (optical disk) at the beginning of the fiber is larger than the fiber area. The radius of the optical disk is about 250 μm (P. Wawer, personal communication 2008). The ratio of incident power that enters the optical fiber is $(\frac{200\,\mu m}{250\,\mu m})^2 = 64\%$. The light goes through the optical fiber, and then enters a second fiber via a connector. At the end of the second fiber there is a slit with dimensions 1000 μm $\times$ 110 μm, which has glue on both sides. The
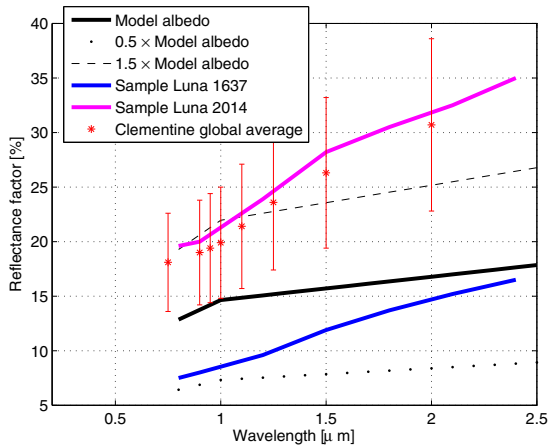
Figure 2.6: Reflectance used in the model calculation together with returned soil samples analysed in laboratory and an average lunar reflectance calculated from the Clementine mission data (Shkuratov et al. 1999a, Cahill et al. 2004).
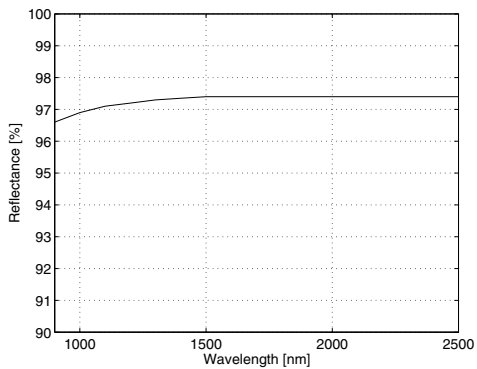

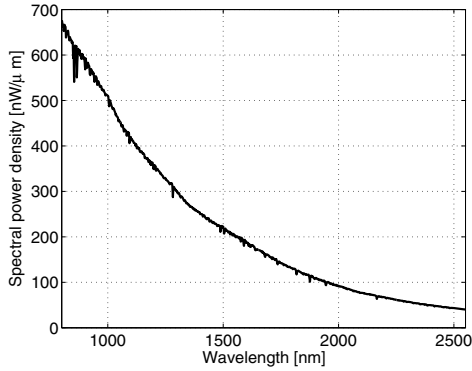Figure 2.7: Reflectance of one of the mirrors in the O-Box (Pleiger company).

Figure 2.8: Power density ($\frac{P}{\Delta\lambda}$) that has entered the optical fiber calculated from Equation 2.3.

fiber does not have a constant diameter and it thins towards the Sensor Head / Radiator unit with a radius at the end of 125 μm. The amount of light through the slit is thus $\frac{2.45\times10^{-8}\ \text{m}^2}{4.91\times10^{-8}\ \text{m}^2} \cong 50\%$. Following the slit there is a filter to block undesired wavelengths, glued to the quartz body (Fig. 2.9). The quartz glass material through which the light traverses has a wavelength dependent transmission curve. There are two absorption bands due to OH, at 1.39 μm and 2.2 μm (see the subsection on vibrational processes in Section 1.2.1). The curved grating (magnification $|M| = 1$) has a reflection coefficient, which is linearly decreasing as a function of wavelength. The combined effect of the quartz body and the grating are shown in Figure 2.10. The image size provided by the concave grating is the same as the slit size, and the length of the illuminated part of the slit matches the width of the detector. In front of the detector there is one more filter, attached by glue, for the longer wavelength half of the detector to block higher order diffractions from the grating. The values of the optical transmissions of the two filters and the glue as a function of wavelength are shown in Figure 2.11. The optically active part of a pixel is 56% of its area leaving the rest of the area for gates (controlling electrodes). The total transmission of SIR-2 spectrometer without the front-end optics, as shown in Fig. 2.12 is calculated as

$$\tau(\lambda) = \tau_{fiber_1}\tau_{connector}\tau_{fiber_2}\tau_{glue}^4(\lambda)\,\tau_{slit}\tau_{blocking\,filter}(\lambda)\,\tau_{quartz}(\lambda)\,\tau_{grating}(\lambda)\,\tau_{2^{nd}order\,filter}(\lambda)\,,$$
$$(2.5)$$

where the individual transmissions are given in Table 2.9 and Figs. 2.9 to 2.11. The quantum efficiency of the detector tells what ratio of incoming photons is transformed to electrons. It is given by the manufacturer and is shown in Figure 2.13 to vary between 23% and 66%. For comparison to other technologies, a photograph has a quantum efficiency in the order of magnitude of 1% and the human eye less than 1% at the most sensitive wavelength (Howell 2006).
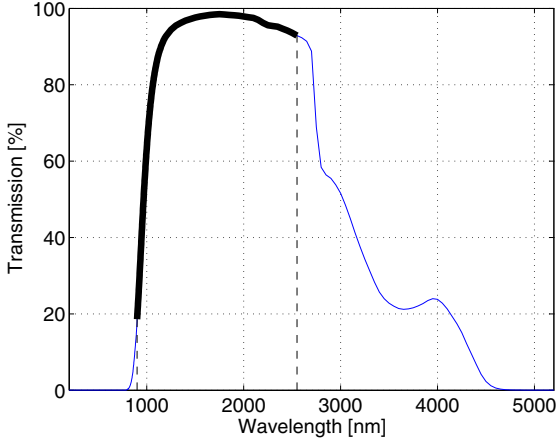
Figure 2.9: Transmission of the RG1000 blocking filter. The thick black curve corresponds to the wavelength range of the Hamamatsu detector (as per Table 2.1).

After passing through the optics, the filters and the detector the instrument output signal s in digital number units is

$$s = \frac{\tau P t}{E_\gamma} \text{QE} \frac{1}{g}, \tag{2.6}$$

where t is the integration time, $E_\gamma = \frac{hc}{\lambda}$ is the energy of one photon, h is Planck's constant, c is the speed of light, QE is the quantum efficiency, and g is the total system gain, and the signal is given in DN units. The gain is calculated as the number of electrons which cover the AD converter range of 2^{16} DN units. To calculate g first the number of electrons for physical saturation is calculated. In the pixel, as shown in Fig. 2.3, the capacitor is collecting the electrons from the photodiode. At maximum it has $N_{sat} = \frac{Q_{sat}}{e}$ electrons, where $Q_{sat} = 30$ pC is the saturation charge (Hamamatsu 2000), and e is the electron charge. This gives 1.8726×10^8 electrons. The value of system gain is thus $g = \frac{1.8726 \times 10^8}{2^{16}} = 2860 \frac{e^-}{\text{DN}}$. The output signal based on the above calculations is shown in Figure 2.14 for the SIR-2 instrument and in Fig. 2.15 for both instruments.
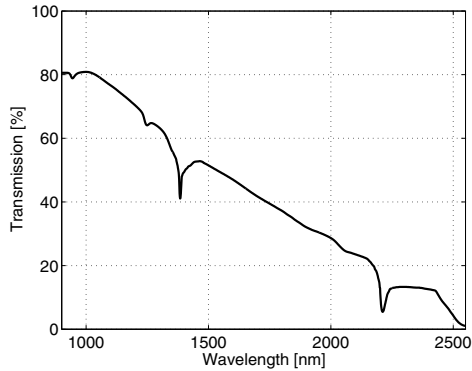
35

Figure 2.10: Combined transmission of the core optics of the spectrometer (reflectance grating and the the quartz body) assuming a total length of the optical path in the glass of 10.9 cm. The absorptions at 1.39 μm and 2.20 μm are caused by OH in the Suprasil quartz glass.

Table 2.2: Optical transmission efficiencies of various parts in the SIR-2 instrument. The blocking filter and the quartz body have a wavelength dependence at short and long wavelengths, respectively. The transmissions of the optical fibers have a weak wavelength dependence, which is ignored in the calculation. As for the SIR instrument, the difference is that only 16% of light enters the lone optical fiber.

| Part	Transm., minimum	Transm., typical	Reference
O-Box optics	94%	95%	Data from Pleiger company
Entry of optical fiber	-	64%	geometrical calculation
Optical fiber	83%	85%	measured by Leoni company
Contact to inner fiber	89%	96%	Diamond LWL data sheet
Inner optical fiber	35%	45%	measured by Leoni company
Optical glue	98%	99%	EPO-TEK 301-2 data sheet
Entry slit	-	50%	geometrical calculation
Blocking filter	30%	97%	Data from Schott company
Diffraction grating	25%	50%	assumption
Quartz body	20%	92%	Heraeus Suprasil 311 data sheet
Active pixel area	-	56%	microscopic inspection
Filter on detector	60%	89%	Zeiss / BK7G18 technical data
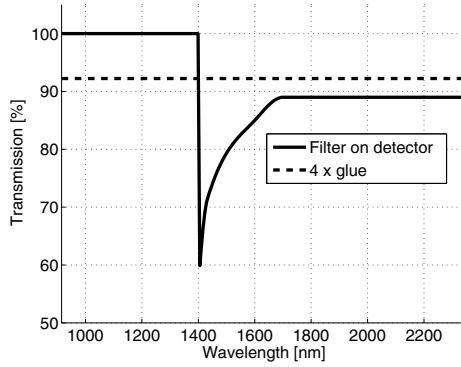
Figure 2.11: Transmission curves of the second order filter of SIR which is partly covering the detector (upper wavelength range), and four layers of optical glue.
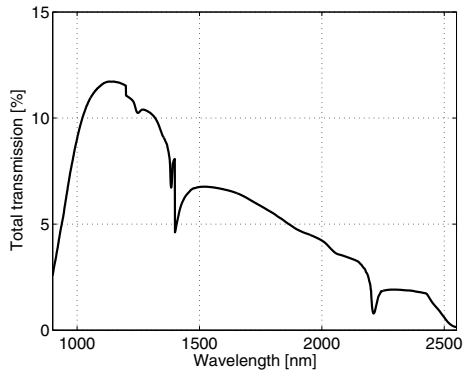

Figure 2.12: Total transmission of SIR-2 from the start of the optical fiber in the O-Box up to the detector. The dip at 1.4 μm is due to the second order filter on the detector, and the dips at 1.39 μm and 2.2 μm are due to an absorption in the glass of the quartz body.
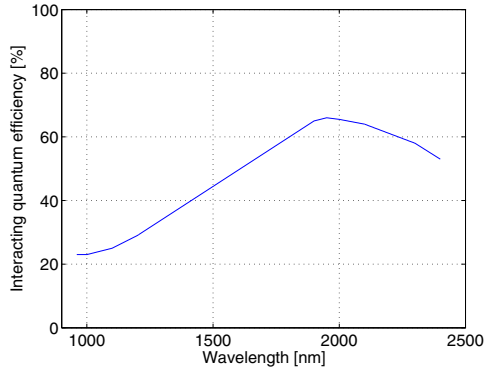
Figure 2.13: Interacting quantum efficiency QE_I of the G9208-256 detector. The QE_I is defined as the ratio of the average number of photons which interact with a pixel and the average number of incoming photons.
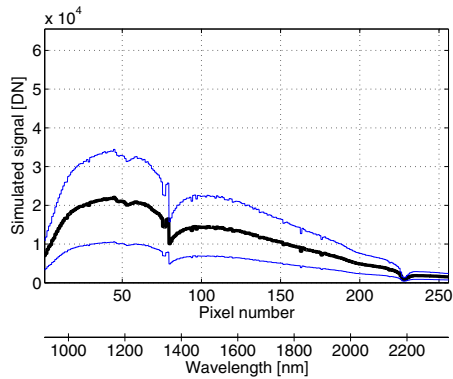

Figure 2.14: Output signal of the SIR-2 instrument as a modeled response to reflected solar spectrum from the lunar surface (black curve). Integration time was 250 ms. The minimum and maximum (blue) values are calculated for dark mare at furthest distance from the Sun and for bright highland at closest Moon distance to the Sun. No thermally induced dark counts are included, that is the detector temperature is assumed to be 0 K. Also the bias is set to zero. The full range of possible DN values is shown in the y-axis.
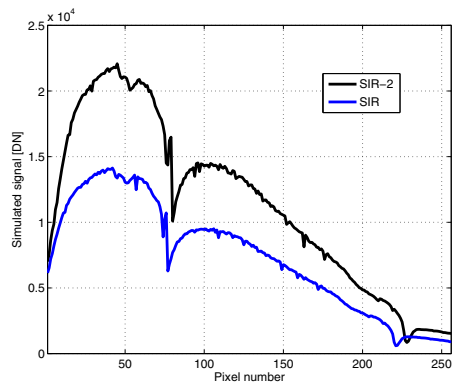
Figure 2.15: Comparison of modeled SIR and SIR-2 observations. The different positions of the absorption bands indicate the difference in the mechanical positioning of the detector during instrument integration.

2.3   Noise processes

Photon noise

The simulated response developed in this chapter has so far neglected noise, which is produced by various processes when a photodiode transforms the incoming photon flux to an electrical signal. The fundamental noise limitation is the quantum nature of the incoming signal: the number of photons k arriving in a unit time interval follows the Poisson statistics (when unit time is long enough so that k is large): $P(k) = \frac{\exp(-n)n^k}{k!}$, where P is the probability of receiving k photons, which are arriving on the average n photons per unit time interval. Both the mean and the variance of the Poisson distribution have the same numerical value n, thus the signal-to-noise ratio (SNR) is

$$\text{SNR}_\gamma = 20\log\frac{\sqrt{\overline{s^2}}}{\sigma} = 20\log\sqrt{n}, \tag{2.7}$$

where $\sqrt{\overline{s^2}}$ is the root-mean-square value of the signal and σ is its standard deviation. The number of photons received and detected by the instrument is $n = \frac{\tau Pt}{E_\gamma}$ QE (from Equation 2.6), and it is a function of wavelength similar to the simulated signal in Fig. 2.14. Using this data, which is based on the average lunar albedo model (2.1) and the ASTM solar irradiance standard, the average over wavelength of SNR_γ is between 98 and 152 dB for integration times from 1 ms to 500 ms, with a logarithmic increase as a function of integration time. The SIR-2 instrument's SNR_γ is approximately 4 dB better than the SIR's, due to improved light gathering power (larger field of view).

Readout noise

Readout noise may consist of many components: the uncertainty in the charge collected by the capacitor of the charge amplifier, the A/D conversion, and fluctuations in the electronics. Any real-life circuit element which has resistivity suffers from thermodynamic noise that arises from thermal motions of charge carriers. When a system is in equilibrium it has an average energy of $\frac{1}{2}kT$ for each degree of freedom, where k is the Boltzman's constant and T the temperature in Kelvin. For a theoretical calculation, there is sufficient data from the manufacturer to estimate the noise of the capacitor of the charge amplifier (C_f in Fig. 2.3), which has the energy due to noise of $\frac{1}{2}C_f V_{\text{noise}}^2$. The only degree of freedom is the noise voltage. Thus, the root-mean-square charge due to noise is (using the capacitor equation $Q = CV$) $Q_{\text{RMS}} = \sqrt{kTC_f}$. Now, the readout noise component in the output signal of the instrument is $s_{\text{READ}} = \frac{Q_{\text{RMS}}}{e}\frac{1}{g}$, where e is the charge of one electron and g is the system gain (electron/DN). However, this noise component of the total readout noise is very small, even at zero degrees Centigrade (0.5 DN).

3 Calibration of the SIR instrument

Measurements in controlled conditions provide an ideal environment for quantifying the response of a remote sensing instrument. Reliable results from inflight data depend critically on calibration. Laboratory based information on instrument's sensitivity curve as a function of pixel number, the bias levels, and the thermal dark count rates are fundamental parameters in the data reduction chain of a NIR spectrometer. The on-ground calibration measurements of the SIR instrument were carried out over one week in the summer of 2002 at the Max Planck Institute for Solar System Research. These calibrations were done separately from the thermal vacuum qualification tests, which had been performed earlier. The calibration procedure was separated into a spectral part and a radiometric part (Sebastian 2002a). The aim of the spectral calibration was to assess the following properties:

- The global spectral coverage of the instrument, that is, its wavelength range.

- The center wavelength of each pixel.

- The spectral point spread function of selected pixels. This shows how the instrument responds to a single-wavelength input.

The aims of the radiometric calibration were the following:

- The absolute spectral sensitivity. This describes the output in instrument units of $\frac{digital\ number}{sec}$ per unit input of radiance.

- The photo response nonuniformity, or spectral "flat-field". This gives the pixel-to-pixel variations in quantum efficiency.

- The linearity with respect to the changes in the level of incoming light intensity.

- The linearity with respect to integration time.

- [With the chamber window closed from incoming light:] the dark count rate and the bias level, and their dependence on detector temperature and integration time.

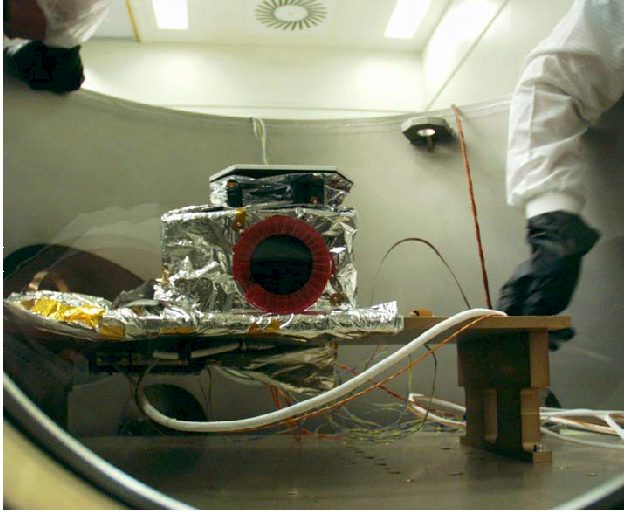The measurement actions are summarised in Table 3.1.

Figure 3.1: SIR instrument on the turntable in the thermal vacuum chamber viewed through a Suprasil window. Adopted from Sebastian (2002a).

Table 3.1: Purposes of calibration measurements. Modified from (Sebastian 2002a).

Purpose	Calibrating device	Activity
Center wavelengths	monochromator	Sweep the wavelength range with line spectra and at each step estimate the (noninteger) pixel numbers of maximum signal level.
Spectral range	monochromator	Take the center wavelength of first and last pixel.
Point spread function	monochromator	Wavelength commanding with sub-pixel steps.
Absolute sensitivity and flat field	integrating sphere	Measure at a specific radiance level, vary integration time and detector temperature to check changes in the response.
Linearity wrt. light intensity	integrating sphere	Keep SIR parameters constant and adjust the light intensity level of the integrating sphere.
Linearity wrt. integration time	integrating sphere	Set a low intensity from the sphere and increase the SIR integration time in steps.
Dark count rate	(closed chamber)	Use a range of SIR integration times at several temperatures.
Bias	(closed chamber)	Intercept, at zero time, of dark level vs. integration time lines at different temperatures.

3.1   The measurement setup and data set

The calibration of the SIR instrument was done in a large clean room of class 10000. The flight model instrument unit (see Fig. 2.1) and the electronics box under a flight spare multi-layer insulation blanket, were placed on a turntable inside the one meter diameter thermal vacuum chamber as shown in Fig. 3.1, and connected to an external Electrical Ground Support Equipment (EGSE) for SIR, located in a check-out room outside the clean room. The pressure in the chamber was in the order of 10 mPa, or 10^{-4} mbar, and the instrument was passively cooled using liquid nitrogen injected into a radiator, a "cooling sky", whose temperature could be lowered to $-170°$ C.

In the spectral set-up shown in Fig. 3.2 the instrument is aligned with the optical axis of the off-axis parabolic collimator 7/1750. Side-mounted to the collimator is the monochromator MS 257 made by L.O.T. Oriel, illuminated by a halogen lamp. It isolates a narrow portion of the incoming light so that the output has an adjustable bandwidth, the minimum being 0.6 nm, and its center lies within ±0.3 nm around the commanded wavelength, according to the calibration of the monochromator done in-house (Sebastian 2002b). The monochromator has three gratings in a motorized turret, one of them covers the NIR with its wavelength range from 600 nm to 2500 nm. That reflection grating has a groove spacing of 600 lines/mm, and reciprocal linear dispersion of 6.4 nm/mm (see Section 1.3). In addition to the plane grating the Czerny-Turner configuration of the monochromator has mirrors for collimating the incoming light to the grating as well as a mirror for focusing the light from the grating to the exit slit. The intensity of the light through the collimator and the monochromator has not been calibrated, because the important parameter in the spectral calibration is the wavelength of the narrow band spectrum. Between the monochromator and the collimator there is a biconvex lens, which is used to get the collimator entrance slit fully illuminated by the monochromator.

In total, 6300 spectra at 20 different wavelengths ranging from 940 nm to 2388 nm were recorded by SIR at three levels of detector temperature: $-55°C$, $-42°C$ and $-2°C$. The average wavelength step was 100 nm. One hundred spectra were measured at one wavelength step of the monochromator, and then the chamber window was covered and ten dark spectra were measured. The purpose of these dark measurements was to subtract the background level from the calibration measurements. Various integration times were in use, which makes the peak intensity levels recorded different but does not affect the wavelength position. Of the measured spectra 85% were useful for calibration purposes, the rest were too noisy or partly saturated. For three pixels, numbers 6, 153 and 248, specific point spread function measurements were made, where the step between commanded wavelengths from the monochromator was 2 nm, in total 1500 line spectra were recorded for point spread function estimation. Overall, 1560 dark spectra were recorded during the spectral calibration for reducing the background level signal of these measurements.

In the radiometric set-up shown in Fig. 3.3, the instrument is sitting in a homogeneous spatial and angular flat-field. In order to know the spectral distribution of the field, the absolute spectral output of the integrating sphere should be known. That was measured during a calibration made by the Physikalisch-Technische Bundesanstalt (PTB 2001), see Fig. 3.4. The PRC Krochmann sphere (serial number 000430) is equipped with four halogen lamps at constant light level and they can be moved mechanically inwards or outwards the sphere to adjust the output light level of the integrating sphere. The sphere also

has photodiodes to measure the exact light level in ultraviolet, visible and NIR. The output of the photodiodes changes as a function of time mainly because the halogen lamps do not have a perfectly stable light output; there is both a short-term and a long-term variability in the sphere output (Nagy 2006). The thermal vacuum chamber has a large 35 mm thick and 265 mm diameter front-end window made of a specific type of quartz glass, Suprasil 1. The window has a deep minimum in its transmission curve near 2.2 μm (see subsection 'Vibrational processes' in Section 1.2.1), where the transmission is lower than 40% (Fig. 3.5). The effect of the window is taken into account in the calibration. The radiometric measurements of 8300 spectra were carried out mostly at three detector temperatures and at seven integration times ranging from 0.5 ms to 151 ms (Fig. 3.6). Dark background measurements were carried out before or after each set of the seven preprogrammed integration times by recording 300 spectra with the chamber window covered. Measurements at short integration times had very low signal-to-noise ratio, especially in the higher temperatures. The linearity with respect to integration time was measured at detector temperature of −50°C using 17 integration times ranging between 5 ms and 503 ms. The linearity with respect to incoming light intensity was measured at detector temperature of −49° C and integration time of 151 ms by mechanically moving the four halogen lamps of the integrating sphere to 18 different positions and recording 300 spectra at each position. The radiance levels achieved by the integrating sphere are suitable for a light linearity study at relatively low light levels compared to the expected radiance of the lunar surface estimated by Equations 2.1 and 2.2, as shown in Fig. 3.7. In order to characterise the dark count rates 67000 dark spectra were measured covering a range of detector temperatures from −58°C to −18°C. The dark measurements are discussed further in Section 3.5.

3.2   Results of the spectral calibration

The wavelength vs. pixel relation as well as the spectral sampling are shown graphically in Sebastian et al. (2002). The center wavelengths as a function of pixel number according to the calibration analysis of SIR are (I. Sebastian, personal communication 2005):

$$\lambda\,(PIX) = (937.72) + 6.26791 \times (PIX-1) - 2.0444 \times 10^{-3} \times (PIX-1)^2 - 7.19 \times 10^{-7} \times (PIX-1)^3,$$
$$\tag{3.1}$$

where PIX is the pixel number between 1 and 256; the difference of this polynomial compared to a straight line is shown graphically in Fig. 3.8. Calculated from this formula, the wavelength range of SIR goes from 938 nm to 2390 nm. The spectral sampling calculated as the difference between the center wavelengths $\lambda\,(PIX)$, varies from 6.3 nm at pixel number 1 to 5.1 nm at pixel number 256. The point spread measurements show that the full width at half maximum (FWHM) is 3 pixels at the center of the array and 5 pixels at the edges (I. Sebastian, personal communication 2005), which means that the Rayleigh resolution is between 18 and 30 nm. According to the Nyquist theorem the maximum information is obtained by sampling the spectrum at one-half of the FWHM, which means 9 to 15 nm depending on the wavelength. Thus, the spectral sampling of the 256 pixels, which is about 6 nm, is small enough not to limit the spectral information obtained; instead the limitation is the Rayleigh resolution of 18 nm.

In determining the pixel number vs. wavelength dependence $\lambda(PIX)$ a Gaussian curve was fitted to the recorded narrow band spectral lines given by the monochromator (see Fig. 4.5 for SIR-2). The center point of this Gaussian is then the decimal pixel number corresponding to the commanded wavelength from the monochromator. For estimating the accuracy of this method, each of the 100 spectra recorded at one instance of commanded wavelength, e.g. at 1940 nm in the figure, were fitted separately and then the center points compared; their standard deviation was 0.01 PIX. When the same wavelength was commanded at three different detector temperatures ($-55°C$, $-42°C$ and $-2°C$) to check possible effects of thermal expansion of the mechanical parts, and with two different integration times, the precision of measurements was ±0.1 PIX. The center wavelengths do not show any change which correlates to temperature. Thus, the main cause of this measurement error would be the accuracy of the commanded wavelength from the monochromator, which has been reported to be 0.3 nm in earlier work (Sebastian 2002b). Since the spectral sampling of SIR is about 6 nm the corresponding error of 0.1 PIX in wavelength units is taken to be 0.6 nm. In order to assess the accuracy of the third order polynomial it is re-fitted to synthetic wavelength vs. pixel number data: 1000 simulated samples of $\lambda(PIX)$ added by Gaussian random noise of standard deviation 0.6 nm gives an average standard deviation of the third order polynomial fit of 0.4 nm. When this is combined with the accuracy of the monochromator output, the center wavelengths are $\lambda(PIX) \pm 0.5$ nm.
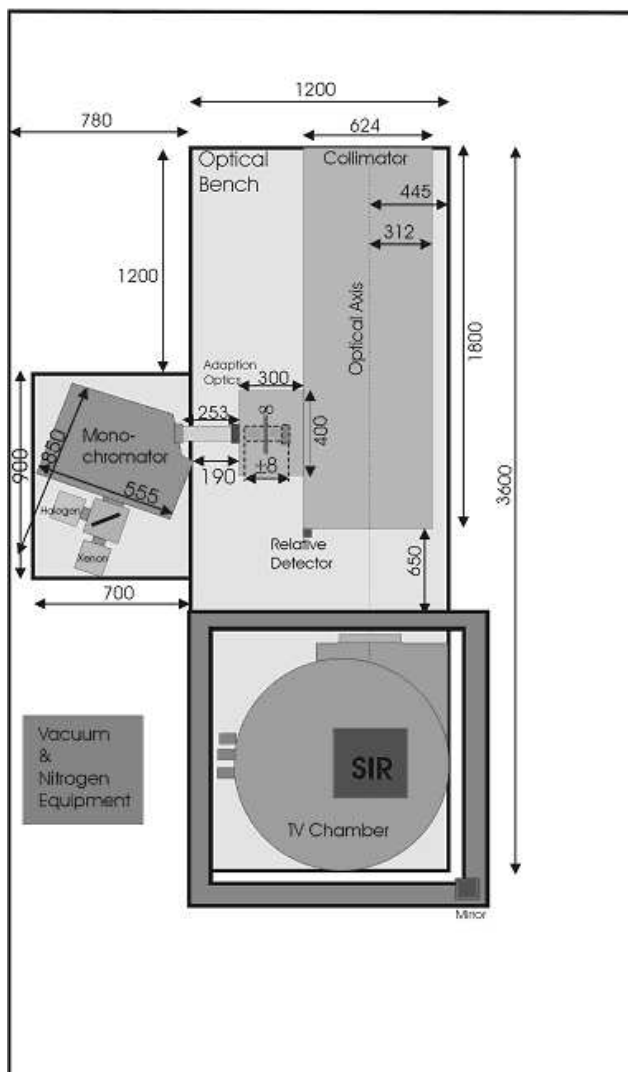
Figure 3.2: Set-up for spectral calibration. The lengths are in millimeters. Adopted from (Sebastian 2002a). The monochromator has an input focal length of 220 mm and an exit focal length of 257 mm. The collimator has a focal length of 1750 mm and its exit slit has a diameter of 22 mm.
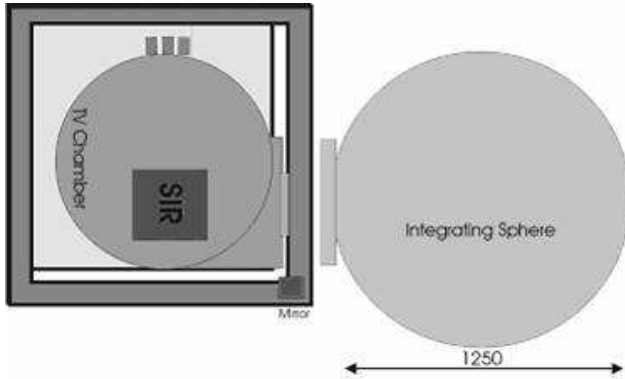
Figure 3.3: Set-up for radiometric calibration. The length is in millimeters. Modified from (Sebastian 2002a).
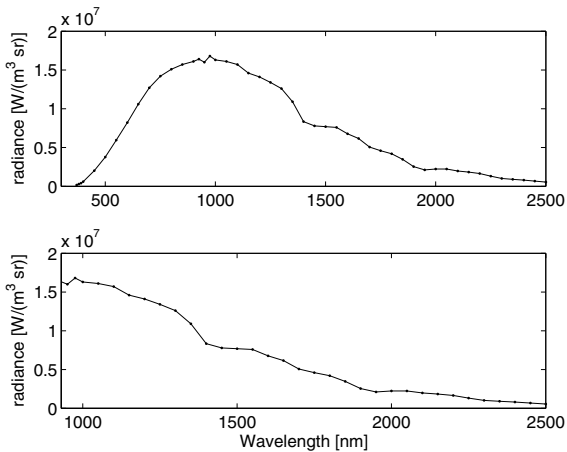

Figure 3.4: The output of the integrating sphere with halogen lamps according to the PTB calibration. The typical wavelength step in the sphere calibration was 50 nm. The accuracy is 0.23 $\frac{W}{m^3 sr}$ or better, and the variations within the angular field are less than 0.5% (Sebastian et al. 2002).
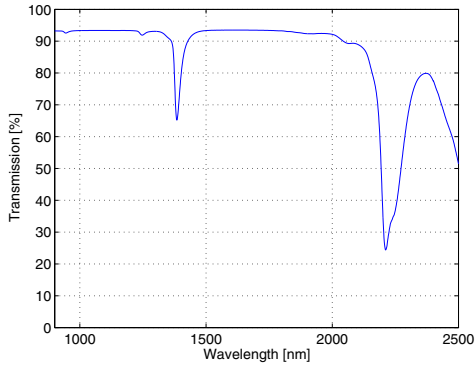
Figure 3.5: Transmission curve of thermal vacuum chamber window made out of Suprasil 1 quartz glass. Calculated for a thickness of 35 mm from data given by the Heraeus company.
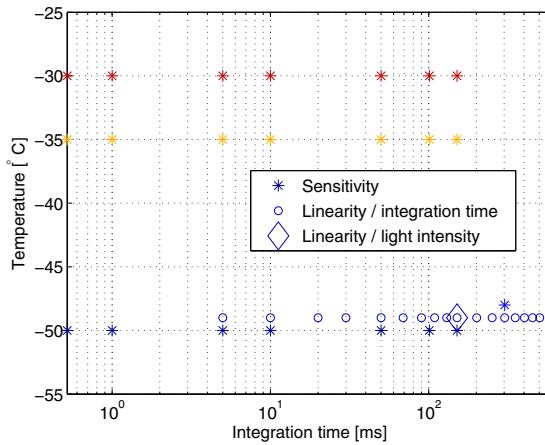

Figure 3.6: The detector temperatures and integration times used in the radiometric calibration of the SIR instrument.
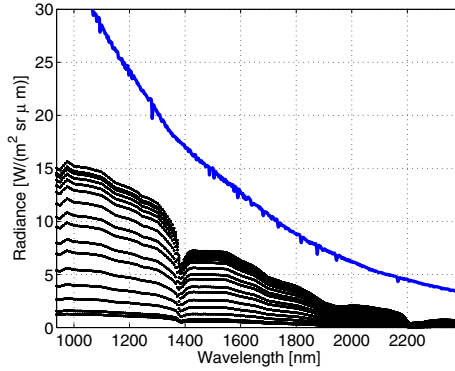
Figure 3.7: Estimated mean radiance from lunar surface (blue) and the radiance available from the Krochmann integrating sphere seen through 3.5 cm of Suprasil glass at different lamp positions (black). The radiance values in other than the standard lamp position have been obtained by multiplying the calibrated radiance by a factor based on measurements at different lamp positions in visible wavelengths (Nagy 2006).
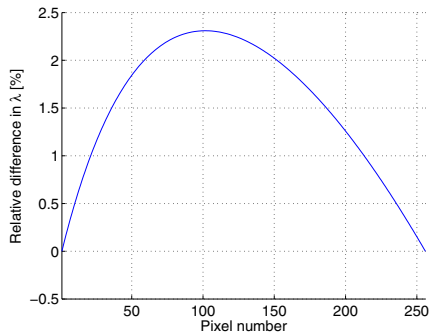

Figure 3.8: The relative difference in wavelength between the third order polynomial used in the pixel number vs. wavelength calibration and a straight line from 938 to 2390 nm. The maximum difference is at pixel number 102 (corresponding to wavelength 1.5 μm), and its value is 36 nm. The differences at pixel 11 (1 μm) and pixel 182 (2 μm) are 5 and 32 nm, respectively.

3.3   Results of the radiometric calibration

The spectral sensitivity curve has been measured repeatedly at different integration times, detector temperatures and amounts of incoming light intensity. The curve is calculated in the following steps: i) reducing the measured dark background from the integrating sphere spectrum recorded by the instrument, making sure that they were measured at approximately the same detector temperature, ii) calculating the average of 300 dark reduced spectra, iii) then dividing by the integrating sphere radiance and window transmission curves, and iv) dividing by the integration time. Examples of several sensitivity curves analysed from the ground calibration data are shown in Fig. 3.9. The results are divided into three categories according to the integration time in order to avoid the possible effect of nonlinearity with respect to integration time. All the curves in this figure were analysed from data measured at the default light level of the integrating sphere. The differences between the curves measured at similar temperatures and integration times are from a few percent up to more than 20% at the longer wavelengths. The signal-to-noise ratios are between 20 and 38 dB, except for the edges of the 256-pixel spectrum. The longer wavelengths (larger pixel numbers) are expected to have worse signal-to-noise ratios due to the lower signal received from the integrating sphere (Fig. 3.4) through the 3.5 cm glass window (Fig. 3.5). Furthermore, the quantum efficiency of the detector is lower at the wavelengths seen near the edges of the photodiode array (Fig. 2.13). When the instrument's sensitivity curve is measured repeatedly at similar conditions the results should be very similar. The repeatability error is defined here as the difference of the maximum and minimum value of the sensitivity curve divided by its mean value; this calculation is shown for three different temperatures in Fig. 3.10. The final spectral sensitivity curve used in the data reduction is shown in Fig. 3.11. When the mean responsivity curves at different temperatures are compared an undesired temperature-related effect is seen in the performance of the SIR instrument: the response is not constant at changing temperatures (Fig. 3.12) as it should be in an ideal case. Although only three temperature levels were in use for this measurement, the probable conclusion is that one or more components in the instrument have an undesired temperature related characteristic, which changes the response up to 50%.

In the case of SIR the photo response nonuniformity was not measured separately before integrating the photo diode array to the spectrometer. Such measurement was carried out in the case of SIR-2 (Sitek et al. 2007), where all the pixels were illuminated by the same spectrum of light directly, without the spectrometer part of the instrument.

Linearity

The measurements for linearity with respect to integration time have been analysed in the integration time range between 20 ms and 500 ms at one detector temperature of $-50°C$. The statistical errors of measurements at a constant integration time compared to the next integration time were generally higher than any detectable nonlinearity effects. However, after first filtering the recorded data with a two stage median filter (Section 5.1) a slight deviation from a straight line could be seen: the 15 data points for each pixel are approximately on a piecewise linear line with the slope of a straight line fit showing a
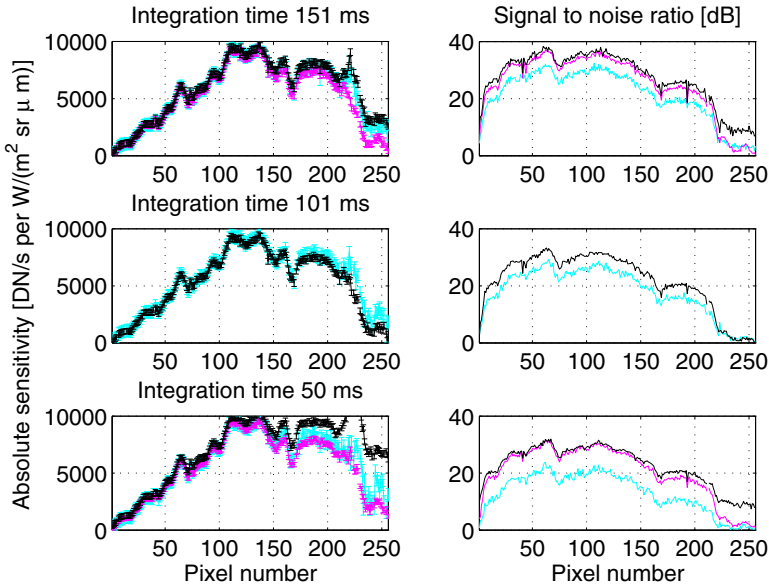
Figure 3.9: SIR spectral sensitivity curves measured at detector temperature $-50°C$ and three integration times. The three colors are from different measurement files to show the repeatability of such a measurement. The corresponding signal-to-noise ratios are shown in the right hand side panels. The decrease in integration time decreases also the SNR level. Measurement file 002 / 31.7.2002 (cyan curve) is constantly at 4 dB higher noise level (lower SNR) than the other measurements. Measurement file 003 / 31.7.2002 (integration times 50 and 151 ms only) has 6 dB lower signal at pixel numbers >215.

higher gradient below 151 ms and a lower one at longer integration times (Fig. 3.13). We define nonlinearity as the maximum deviation of a straight line fit to the whole data set of 15 points from the piecewise linear fit; this is shown in Fig. 3.14.

The linearity with respect to incoming radiance was measured by recording 300 spectra at lamp positions 12, 15, 16, 18, 20, 22, 25, 28, 30, 33, 35, 38, 41, 44, 47, 48, 49 and 50 mm of the integrating sphere during a time period of two hours. These values correspond to different values of radiance as shown in Figure 3.7. The shape of the response curve (Fig. 3.9) suggests that the output values of the instrument as a function of incident radiance change by differing amounts for each pixel, that is, the sensitivity varies over the wavelength range. This can be seen in the output signal versus input
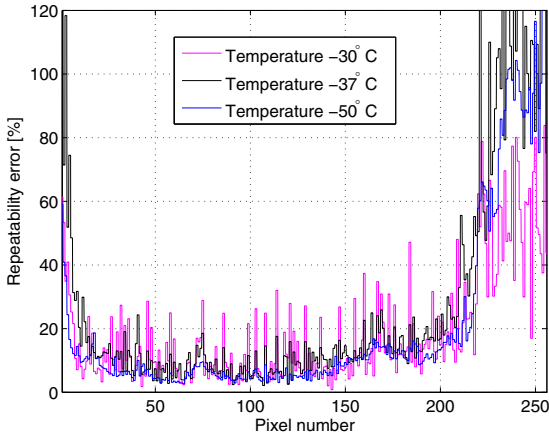
Figure 3.10: Repeatability of the sensitivity curve measurement: relative difference between the maximum and minimum value at three temperatures; at each temperature six to eight curves at varying integration times were taken into account. The repeatability error is between 3% and 20%, except at both edges where the absolute sensitivity calibration becomes unreliable.

radiance representation as different slopes for different pixels (Fig. 3.15). The scattering of data points shows the repeatability of the measurement after filtering for noise peaks (see Section 5.1). There is no systematic nonlinearity at the low light levels used in these measurements (the maximum background corrected signal is 12000 DN out of about 51300 DN), except at extremely low light levels; the minimum light level of the integrating sphere for linear operation of the instrument is 0.06 $\frac{W}{m^2\,sr\,\mu m}$. This value applies for all pixels independent of the level of the signal in DN units which differs for every pixel. Applying Equation 2.3 and using this limit of radiance and the field of view and aperture diameter from Table 1.4 the minimum power incident on the instrument is $P = 0.06 \frac{W}{m^2\,sr\,\mu m} \times 6$ nm $\times \frac{\pi}{4} \times (1.11$ mrad$)^2 \times \pi(\frac{72\,mm}{2})^2 = 1.4$ pW. While the incident radiance was the only changing variable of the measurement two pixels (212 and 223) were identified as gray, that is their output value is almost constant independently of the incoming amount of light.
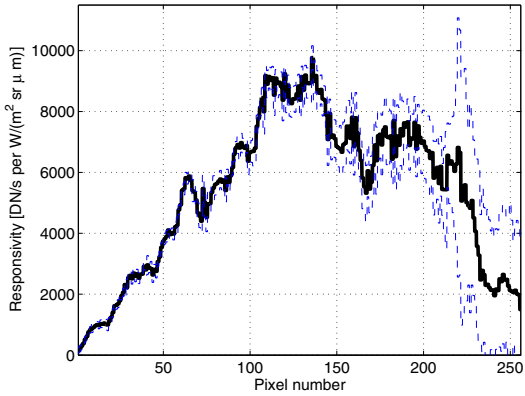
Figure 3.11: The absolute spectral responsivity of the 256 pixels based on ground cali-
bration (Sebastian et al. 2002). The repeatability error at detector temperature −50°C as
a result of the reanalysis of the calibration measurements is shown as a dashed line.
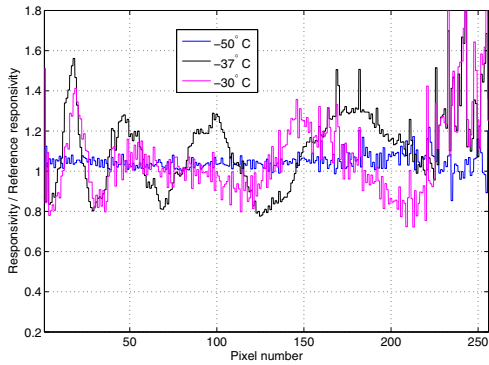
Figure 3.12: Response curves at different detector temperatures divided by the final sen-
sitivity curve (Fig. 3.11). The deviation from a straight line is due to a component in the
instrument which has an undesired temperature characteristic.
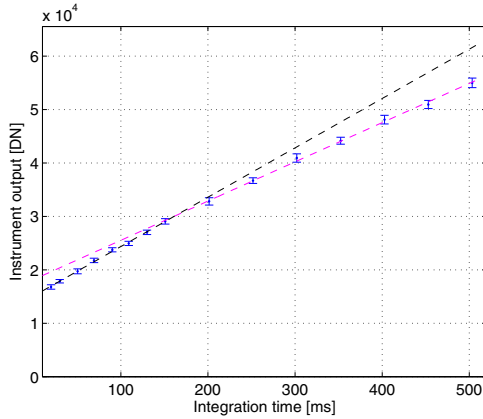
Figure 3.13: Linearity measurements of pixel number 169. Two straight lines have been fitted to the data with the pivot point at 150 ms. The error bars are the 3σ error limits. The scale of the y-axis covers the full range of instrument output; the bias and dark counts have not been corrected in the signal.
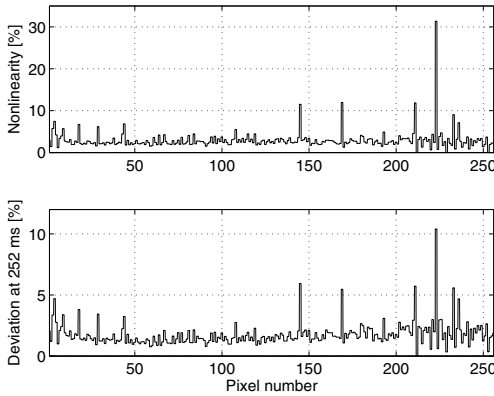
Figure 3.14: The maximum deviation relative to signal level from a straight line fit of the linearity measurements at 15 integration times between 20 and 503 ms. The maximum deviation occurred at the longest integration time for each pixel. The lower graph is the deviation from a straight line fit of each pixel at the most commonly used integration time during the SMART-1 mission.
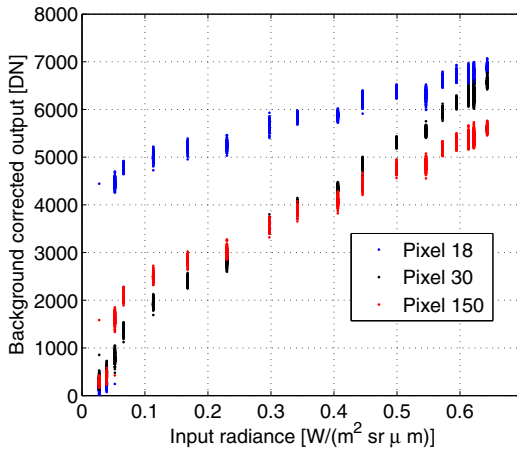
Figure 3.15: Instrument output of three selected pixels as a function of incoming radiance. The output signal of the instrument was first filtered with a two-stage median filter and then the bias levels and the dark counts were reduced. The minimum light level for linear operation is $0.06 \; \frac{W}{m^2 \, sr \, \mu m}$.

3.4   Calibration of detector thermometer

Incoming photons produce electron-hole pairs within the semiconductor of the photodiode array; in addition to that, thermal excitation of electrons to the conduction band due to ambient temperature is also included in the electrical signal. This dark current should be reduced and to accomplish this the temperature of the semiconductor should be known. Inside the detector unit there is a thermistor feeding a 16 bit A/D converter providing temperature data.

The digital reading of the detector's thermistor was calibrated using a PT100 temperature sensor located outside the detector housing: a four-wire system with a S651PDX24A temperature sensor head with an accuracy of ±0.12% at zero degrees centigrade (Telemeter Electronic 2005). The detector's thermistor is in a series connection with a bias resistor, which is connected to a reference voltage, see Fig. 3.16. The input voltage of the 16-bit A/D converter is the voltage across the thermistor. When the resistance of the thermistor changes as a function of temperature, then the voltage division between the two resistors changes as well, which is recorded as changing digital readings. The resistance of the thermistor can be modelled with an exponential function (Hamamatsu 2003):

$$R_t(T) = R_{ref} \exp\left(B\left(\frac{1}{T} - \frac{1}{T_{ref}}\right)\right), \tag{3.2}$$

where R_t is the resistance of the thermistor, T is the absolute temperature, B is a constant and R_{ref} is the resistance at a reference temperature T_{ref}, such that $R_t(T_{ref}) = R_{ref}$. From the division of voltages it follows that the resistance of the thermistor can be written as

$$R_t(DN) = \frac{R_{bias}}{\frac{DN_{max}}{DN} - 1}, \tag{3.3}$$

where DN is the digital reading, DN_{max} the maximum value from the A/D converter, and R_{bias} the bias resistance. Thus, the voltage over the thermistor has been written in terms of the A/D reading and the supply voltage V (Fig. 3.16), which cancels out from the equation. Combining Equation (3.2) and Equation (3.3), and solving for DN yields

$$DN(T) = \frac{DN_{max}}{1 + A\exp\left(B\left(\frac{1}{T} - \frac{1}{T_{ref}}\right)\right)}, \tag{3.4}$$

where $A = \frac{R_{bias}}{T_{ref}}$.

The calibration comprised of four sessions, lasting between five and 25 hours. The temperature was varied between 188 K(−85°C) and 305 K(+32°C). The readings were recorded every 4.4 seconds, but since readings from the PT100 sensor were updated only once every minute, it was first interpolated to the same sampling interval. If the curve in Equation (3.4) is fitted to solve A, B, and T_{ref}, the residual plot shows a systematic error of the form

$$DN = a\exp\left(-\frac{(T - b)^2}{c^2}\right) + Td + e, \tag{3.5}$$

where $a, \dots, e$ are constants. A second fit was made to the systematic part of the residuals. The fitting method used in both fits was the Levenberg-Marquardt iteration. The calibration measurements and the fit are shown in Fig. 3.17. The values of the fitted parameters are given in Table 3.2.
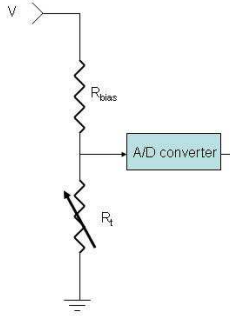
Figure 3.16: Electrical circuit of the thermistor (R_t) inside the detector housing. The bias resistance was 47 k Ohm and the reference voltage was V=4 V.

Table 3.2: Fitted parameter values for temperature calibration.

parameter	initial guess	fitted value
A	$9.4 \frac{\Omega}{K}$	$9.5 \frac{\Omega}{K}$
B	3200.0 K	2976.9 K
T_{ref}	298.0 K	298.0 K
a	1500.0	1667.8
b	240.0 K	238.1 K
c	29.0 K	32.1 K
d	$3.0 \frac{1}{K}$	$6.7840 \frac{1}{K}$
e	-1500.0	-2628.6
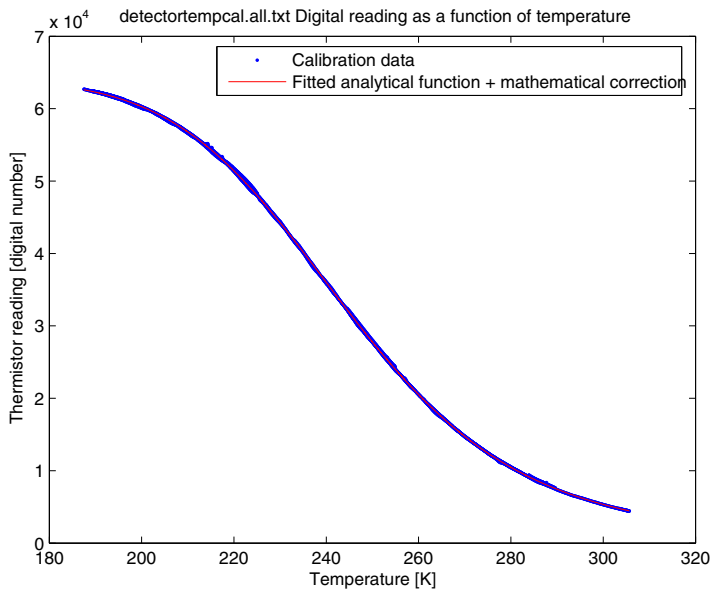
Figure 3.17: Calibration measurements of the temperature sensor. Digital readings from the thermistor inside the detector are modelled as a function of temperature, which is given by a PT100 sensor outside the detector.

3.5 The bias and the dark count rate

The digital reading that a photodiode array produces includes a *bias* value, which is the value that a pixel gives even when the integration time is zero, as well as a dark level, which depends on the integration time and exponentially on the temperature. The combination of the bias and dark levels is called the dark spectrum or *dark background*. Dark spectra were measured at different temperatures and integration times with the window of the thermal vacuum chamber covered. More than 67000 dark spectra measurements have been documented and visually inspected to eliminate those suffering from obvious technical faults. Examples of two dark spectra are shown in Fig. 3.18. The integration times in the calibration measurements were varied from 0.52 ms to 503 ms. In a typical measurement, SIR was commanded to use the following cycle of integration times: 0.52, 1, 5, 10, 20, . . . , 90, 100, 150. At each integration time 40 spectra were measured. This basic cycle was repeated three times; every fourth cycle was longer and had more steps in the integration time reaching 503 ms. The temperature varied typically between $-58°C$ and $-18°C$ with few measurements also made at higher temperatures above $0°C$. The different calibration conditions in a temperature - integration time diagramme are shown in Fig. 3.19.

The higher the temperature and the longer the integration time are, the higher is also the digital output value of a pixel, as shown in Figs. 3.20 and 3.21. When the value exceeds a certain limit, a pixel will saturate, i.e. output the maximum value of 65535 DN, which is probably smaller than the true value would be. The saturation limit cannot exceed the physical saturation, which equals the voltage range (as calculated in Table 2.1) added to the voltage equivalent of 0 DN. The A/D converter is designed so that its maximum digital number is less than the equivalent physical limit. At which temperature and integration time saturation occurs, depends on each individual pixel: if a pixel's saturation region is independent of temperature, that is it saturates always after exceeding a certain integration time, then the pixel is deemed defective. Pixels number 212 and 223 are defective in this way; they had already been classified as gray pixels based on the response to changing amount of incident light (Section 3.3). If a pixel is in saturation more than 10% of the time in one set of measurements at constant integration time, then the average value of that set is not used in the calibration.

The number of consecutive spectra measured at a constant integration time, and practically constant temperature, varied from 9 to 300. The calculation of the average value of the spectra is sensitive to outliers, or other values which lie far from the mean because of either the shape of the distribution of the data points or because of noise: in such cases the median gives a more robust estimate. On the other hand, a median in the case of good quality data is more sensitive to variations than a mean is. Because there are different scenarios with different amounts of spectra in one set with different noisiness properties, a restricted mean is employed. In this case, a Winsorized mean with only values within two standard deviations from the average, are used in calculating the mean value.

The data measured with the chamber window covered are divided into temperature categories with 0.5 K bins. When the dark level data of one such category and one pixel are plotted as a function of integration time, a straight line is obtained. At increasing temperatures the slope of the line increases exponentially, but the intercept at zero integration time, which gives the bias, should be the same. However, in practise the data points do
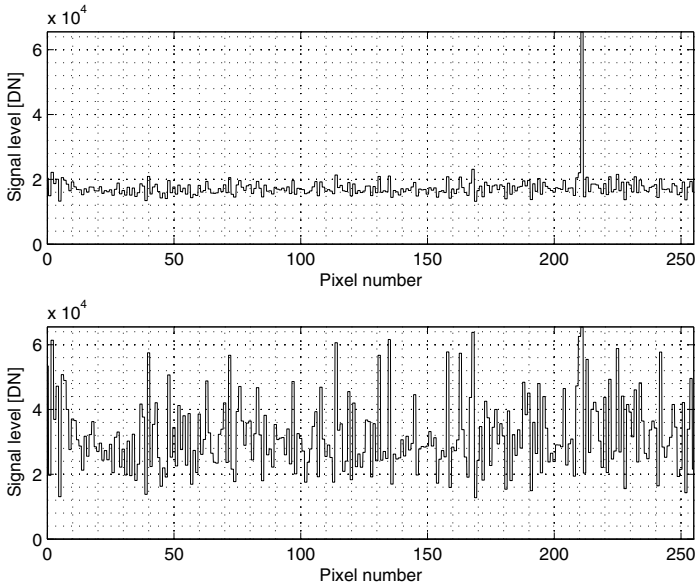
Figure 3.18: Two dark spectra. The integration times are 10 ms and 80 ms for the upper and lower panels, respectively. The temperature was 255.0 K($-18°$C) during both measurements. The strongest peak is the defect pixel number 212.

not obey a straight line, but there is a tendency to a lower slope at higher integration times. Also, there are seven damaged pixels, whose slopes do not increase with increasing temperature. These are pixels number 6, 40, 170, 182, 192, 229, 242, and 253. An example of such instance is shown in Fig. 3.22 where the linear part starts at an integration time of 100 ms, below which the dark signal is not linear, contrary to the example in Fig. 3.21. Furthermore, the intercept values which give the bias are different at different temperatures.

Straight lines are fitted to the data assuming that the measurement errors are not correlated to each other. The residuals are then checked for first order serial correlation using the Durbin-Watson test (Draper and Smith 1981). Even though serial correlation does not affect the consistency of the fitted parameters, it does make the error estimates too optimistic. In first order serial correlation the residuals are assumed to follow a first-order autoregressive process

$$\hat{\varepsilon}_i = \rho \hat{\varepsilon}_{i-1} + z_i, \tag{3.6}$$
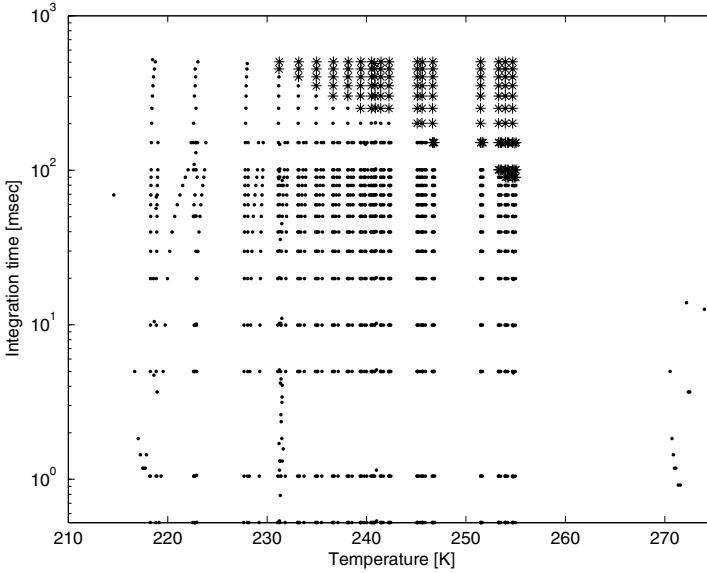
Figure 3.19: Temperatures and integration times used in the 67000 measurements of the dark spectra. The asterisk indicates conditions where pixel number 6 saturates.

where ρ is the correlation coefficient, $z_i \sim N\left(0, \sigma^2\right)$ is a random error term with variance σ^2 and it is independent of $\hat{\varepsilon}_{i-1}, \hat{\varepsilon}_{i-2}, \ldots$ and of $z_{i-1}, z_{i-2}, \ldots$. The mean and variance of $\hat{\varepsilon}_i$ are assumed to be constant which gives $\hat{\varepsilon}_i \sim N\left(0, \frac{\sigma^2}{1-\rho^2}\right)$. The test statistic is

$$d = \frac{1}{\sum_{i=1}^{N} \hat{\varepsilon}_i^2} \sum_{i=2}^{N} \left(\hat{\varepsilon}_i - \hat{\varepsilon}_{i-1}\right)^2 \approx 2\left(1 - \rho\right), \qquad (3.7)$$

where N is the number of data points. The approximation is valid for large N. d gets values in the range from 0 to 4, where d close to 2 means no serial correlation, $d < d_L$ means positive serial correlation and $d > 4 - d_L$ means negative serial correlation, where d_L is the lower Durbin-Watson limit, which is tabulated for $N \geq 15$ by Durbin and Watson (1951). If correlation exists, we estimate the coefficient ρ and calculate a new fit using the general least squares method, where the error term is allowed to be autocorrelated. The non-diagonal elements of the measurement error covariance matrix are constant in each sub-diagonal similar to a symmetric Toeplitz matrix. The elements are ρ^k, where k is the
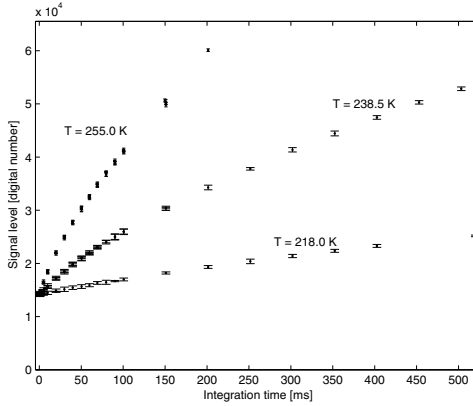
Figure 3.20: Dark signal measurements of pixel number 3. For clarity, only three temperature categories are shown. The error bars are standard deviations of the averaged dark level values.

distance from the main diagonal. The effect of serial correlation is illustrated in Fig. 3.23, where both ways of fitting are shown: the linear fit without taking into account serial correlation and the fit to the same data taking the serial correlation effect into account. The latter case gives a more consistent estimate of the bias value (this estimate is shown in Fig. 3.24), that is the intercept terms are much closer to each other in value. This serial correlation method is often used in time series data analysis; here it is applied to remove the effect of small nonlinearities in estimating the intercept point of straight line fits.
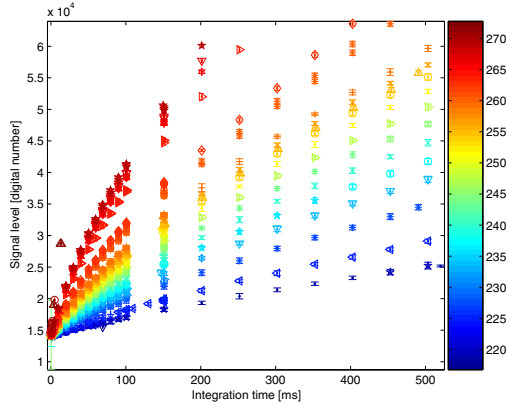
Figure 3.21: Dark signal measurements of pixel number 3. The temperatures are color coded in Kelvin units. The error bars are standard deviations of the averaged dark level values.
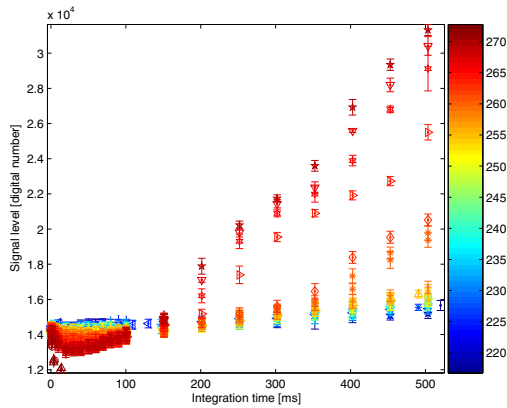
Figure 3.22: Dark signal measurements of pixel number 40 as an example of a defect pixel. The temperatures are color coded in Kelvin units. The error bars are standard deviations of the averaged dark level values.

63
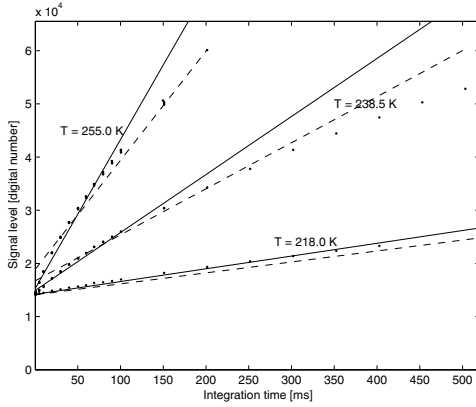
Figure 3.23: Lines fitted to the data of Fig. 3.20. The dashed lines were fitted assuming no correlation between residuals and in the solid lines first order serial correlation has been taken into account.
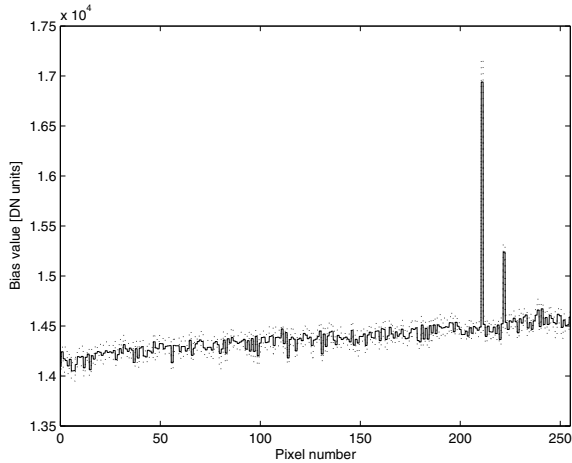
Figure 3.24: Bias values of the 256 pixels. The two peaks are pixels number 212 and 223, which are defect. The average bias is about 22% of the maximum digital number of 65535. The dotted lines are the standard deviations.

The *dark count rate*, that is the dark level in digital number units divided by the integration time, shows an exponential behavior as a function of temperature. To justify such a relation, the behavior of the semiconductor is viewed. There is an increasing probability of electrons to be excited into the conduction band of the semiconductor. The distribution of electrons over the allowed energy states follows the Fermi-Dirac distribution function (Rieke 1996)

$$f(E) = \frac{1}{1 + \exp\left(\frac{E-E_F}{kT}\right)}, \tag{3.8}$$

where E is the energy, E_F is the Fermi level and k is the Boltzmann's constant. In the conduction band, the concentration of electrons is

$$n_c = \int_{E_c}^{\infty} f(E) N(E) \, dE, \tag{3.9}$$

where $N(E) \, dE$ is the density of states in the interval dE. This integral can be simplified by using the effective density of states N_c, located at the conduction band edge, E_c, such that (Rieke 1996)

$$n_c \approx N_c f(E_c) \tag{3.10}$$

because at modest temperatures the conduction electrons occupy only the bottom few states in the band. The effective density of energy states can be shown to be (Rieke 1996, Streetman 1990)

$$N_c = 2 \left(\frac{2\pi m_{eff}(T) kT}{h^2}\right)^{\frac{3}{2}}, \tag{3.11}$$

where m_{eff} is the effective mass of a conduction electron and h is the Planck's constant. The value of kT is relatively low compared to $E_c - E_F$, so approximating f, Equation (3.10) can be rewritten

$$n_c = 2 \left(\frac{2\pi m_{eff}(T) kT}{h^2}\right)^{\frac{3}{2}} \exp\left(-\frac{E_c - E_F}{kT}\right). \tag{3.12}$$

Thus, the concentration of electrons in the conduction band is proportional to $\exp\left(-\frac{E_c-E_F}{kT}\right)$.

Since the parameters E_C and $m_{eff}(T)$ are not given by the manufacturer of the $In_xGa_{1-x}As$ (relative abundance x tunes the band gap) semiconductor and also because there are other contributions to the dark current than the electrons in the conduction band, we give a simplified mathematical model. The dark count rate has an exponential part as well as a power law part like the concentration of electrons in the conduction band:

$$I' = aT^b \exp\left(\frac{c}{T}\right), \tag{3.13}$$

where I' is the count rate, which can be expressed as the dark current if the system gain is known, T is the temperature in Kelvins and a, b, and c are parameters to be fitted. The fit is done for each pixel separately. The result of the fit for pixel number 3 is shown in Fig. 3.25. A combined plot of all fitted dark curves shows the variation between pixels in Fig. 3.26. The values of the parameters are shown in Figs. 3.27, 3.28, and 3.29.
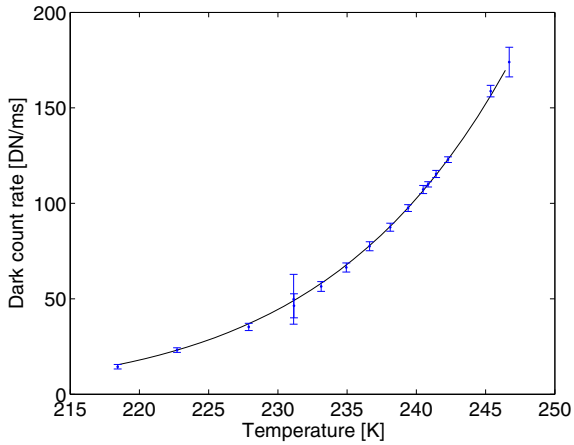
Figure 3.25: Count rate fitted to dark spectra measurements. The initial guess was $a = 1000$, $b = c = 0$, and the result $a = 673$, $b = 2.42$, $c = -3592$.

An error estimate of the dark count rate curve is obtained by taking a total differential of Equation 3.13:

$$\Delta I'(T) = I(T)\left[\frac{\Delta a}{a} + \ln T \Delta b + \frac{1}{T}\Delta c\right], \tag{3.14}$$

where Δa, Δb, and Δc are the error estimates of the parameters.
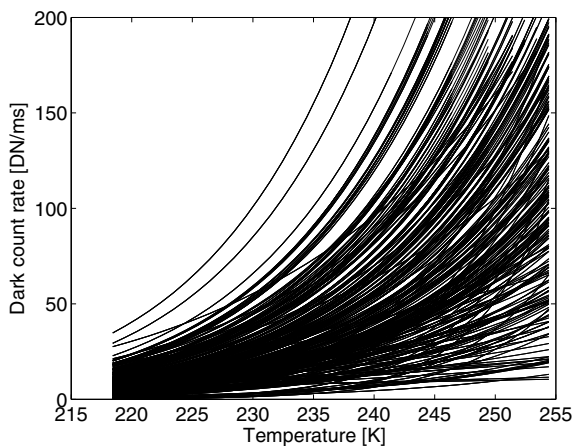
Figure 3.26: Fitted count rate functions of all non-defect pixels.
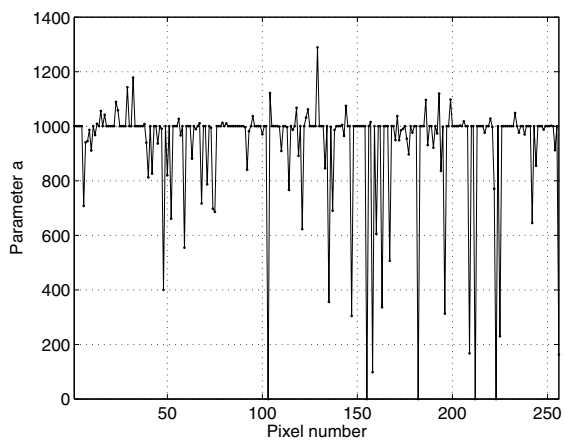
Figure 3.27: The a parameter of dark count rate. Zero value indicates a failed fit due to a defect pixel. The median value is 1000.
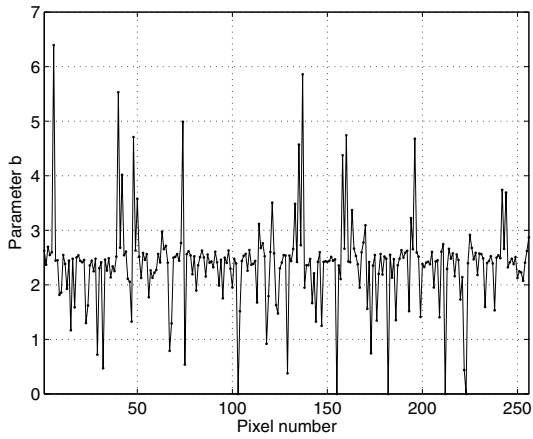
Figure 3.28: The b parameter of dark count rate. The median value is 2.44.
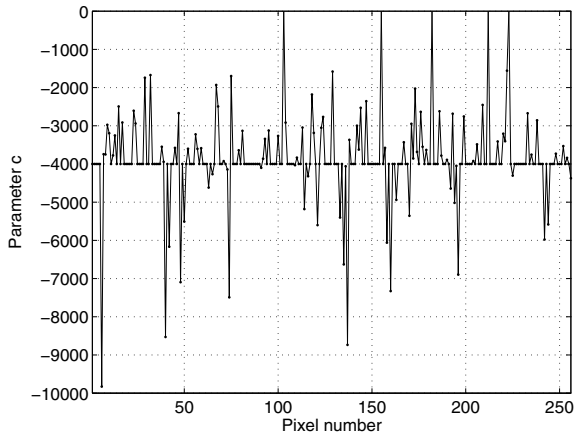
Figure 3.29: The c parameter of dark count rate. The median value is -4000.

4 SIR-2 instrument calibration

Two similar SIR-2 NIR spectrometers have been built and calibrated and one of them was finally selected as the flight model. One of the potential flight models was calibrated in a thermal vacuum chamber during one week in October 2007 at the Space Applications Center of (Indian Space Research Organisation) ISRO in Ahmedabad, India (Fig. 4.1). The calibration included a spectral and a radiometric part as well as dark background measurements with closed window of the chamber. The goals and purposes of calibration measurements are described in Chapter 3 and Table 3.1. The other potential flight model, after replacing an optical blocking filter (Section 2.2), was calibrated in May 2008 in the same facility as the SIR instrument had been calibrated (Chapter 3).

The potential flight model of the SIR-2 instrument was placed in the calibration chamber, covered with test multi-layer insulation blanket. An interior view of the chamber is shown in Fig. 4.2. Each of the three components (Fig. 2.4) were at different operative temperature environments controlled by the vacuum chamber equipment. A cooling shroud was used for the O-Box and E-Box, and a liquid nitrogen cooling plate for the Sensor Head / Radiator Unit (SHRU). The pressure was smaller than 2 mPa. Thermal analysis shows that without temperature control the temperature of the detector in a 100 km lunar noon-midnight orbit ranges between $-54°C$ to $-42°C$ (Das 2007) but in other orbits it is lower. The detector temperature during calibration was actively controlled to be either $-50°C$ or $-60°C$. The software version of the instrument was version 0.4. from the University of Bergen, Norway, and the ground support equipment was controlled by a computer running an IDA GSEOS 5.29 software which was configured for the SIR-2 instrument.

4.1 Spectral calibration

The main purpose of spectral calibration was to determine the dependence of the pixel number on wavelength. Other purposes were to determine the spectral range and spectral sampling of the instrument as well as the point spread function of a few pixels.

A grating monochromator and a collimator were located in front of the window of the thermal vacuum chamber as shown in Fig. 4.3. The double monochromator was a Bentham DTMc300 / UMS UV to FIR spectroradiometer calibrated to an accuracy of 1 nm. The light source was a Bentham illuminator IL 6D, and the collimator was Optronic Laboratories Inc. 740-4.

Several data sets were measured during two days (see Appendix B for a complete list). Since the monochromator could not accomplish a sweep of the whole wavelength range with one setting, the measurements had to be divided into smaller parts in the range

Figure 4.1: The 1.7 meter thermal vacuum chamber at ISRO. The window of the chamber is on the left (not shown).
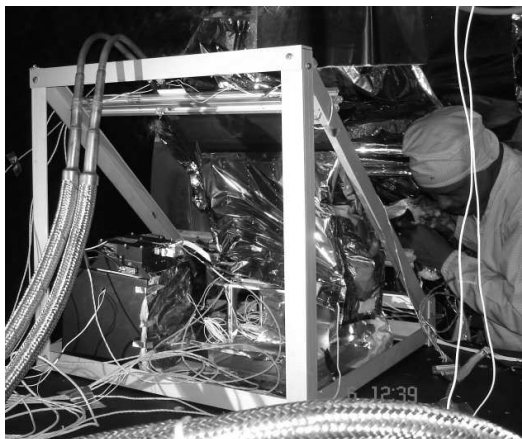
Figure 4.2: Installation of the instrument into the thermal vacuum chamber. The two pipelines are liquid nitrogen in the cooling radiator.
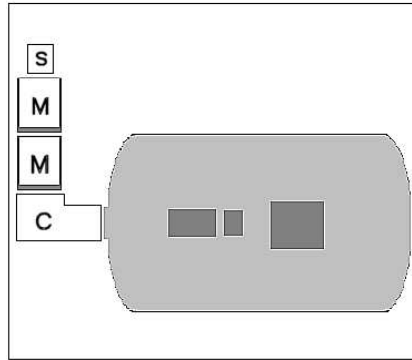
Figure 4.3: Set-up of the spectral calibration. S=light source, M=monochromator, C=collimator. Inside the chamber the three components of the instrument from left to right are O-Box, E-box, and the Sensor Head / Radiator Unit. The distance between the O-Box and the window was 97 cm.

between 900 nm and 2500 nm. At detector temperature of −60° C and quartz body temperature of −40° C the number of measurement runs was 21, out of which 9 were useful for calibration purposes in terms of signal-to-noise ratio and distinguishability of spectral lines at the beginning and at the end of the sweep. Another set of data was obtained at detector temperature of −50° C. A typical example of the recorded spectral line is shown in Fig. 4.4. Using four measurement runs, numbers 72, 73, 75, and 113 in Appendix B, with transitions between data sets at 1250 nm, 1700 nm, and 2000 nm, the position of the recorded line as a decimal pixel number was obtained by making a Gaussian fit to each line spectrum observed by the instrument. A typical fit is shown in Fig. 4.5, and the locations of the centers of the Gaussians are shown in Fig. 4.6. To determine the wavelength as a function of pixel number a third order polynomial was fitted to the data. The following result was obtained for the wavelength as a function of pixel number:

$$\lambda(\mathrm{PIX}) = 909.27 + 6.4421 * \mathrm{PIX} - 2.9386 \times 10^{-3} * \mathrm{PIX}^2 - 1.1334 \times 10^{-6} * \mathrm{PIX}^3 \quad (4.1)$$

as is shown in Fig. 4.7. The spectral range according to this formula is from 916 nm to 2385 nm. The difference between the 242 values and the polynomial fit is shown in Fig. 4.8 while the spectral sampling as calculated from Formula 4.1 is shown in Fig. 4.9. The residuals are smaller than the spectral sampling, that is the difference between adjacent pixels, and their absolute value is decreasing as a function of pixel number as does the spectral sampling.
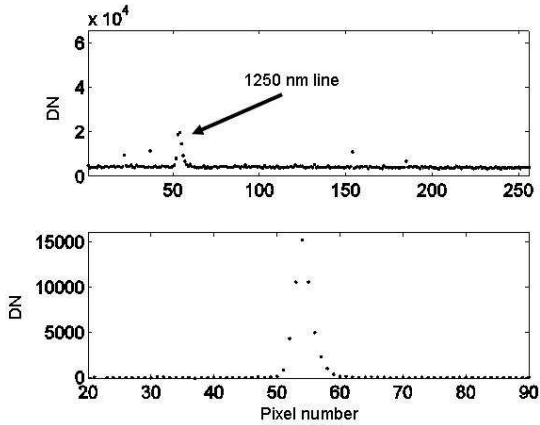
Figure 4.4: The spectral line at 1250 nm recorded by the SIR-2 instrument. The upper panel shows the raw measured values in the full dynamic range of 2^16 DN, and the lower panel shows a zoomed and background corrected image of the line.
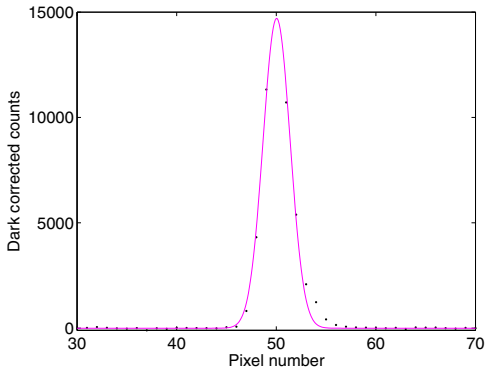
Figure 4.5: A Gaussian fit to the spectral line measurement. The parameters are: height 14700 DN units, center position 50.0 PIX, width 1.92 PIX.
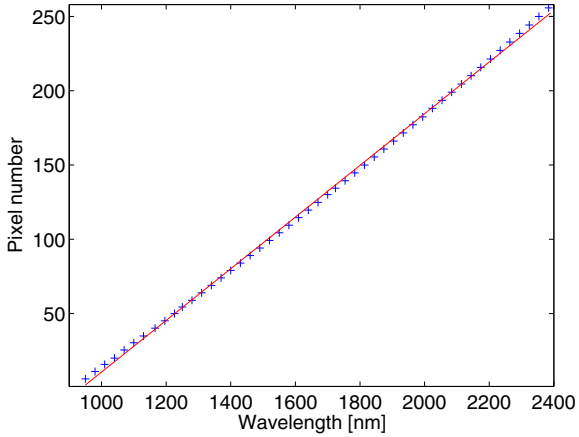
Figure 4.6: Centers of line spectra calculated from fitted Gaussians (blue crosses). Every fifth point is shown in the graph. The wavelength values are given by the monochromator with steps of 6 nm. The fitted straight line is $\mathrm{PIX}\,(\lambda) = 0.174\lambda - 163$.
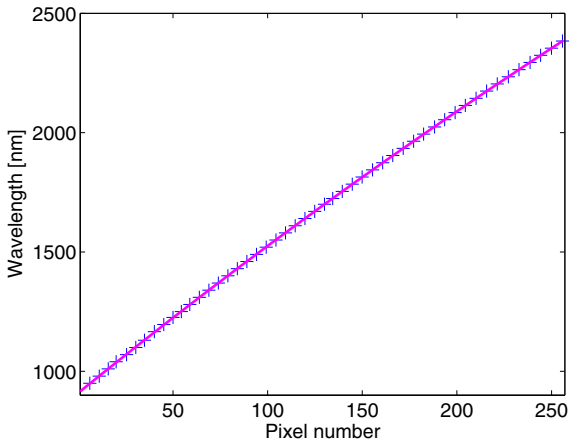
Figure 4.7: Third order polynomial to determine the wavelength vs. pixel number relation. Only every fifth data point is shown.
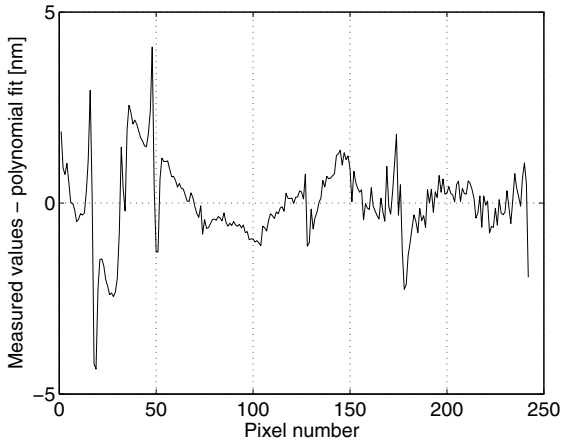
Figure 4.8: Residuals of the polynomial fit. The transitions of the four data sets occur at pixel numbers 54, 130, and 184.
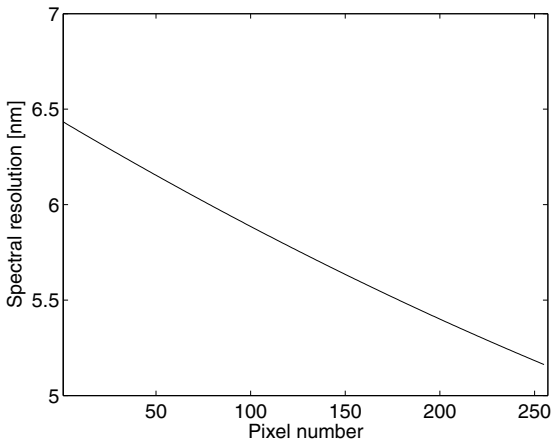
Figure 4.9: Spectral sampling as a function of pixel number. The resolution is calculated by taking the difference between pixels in the third order polynomial.
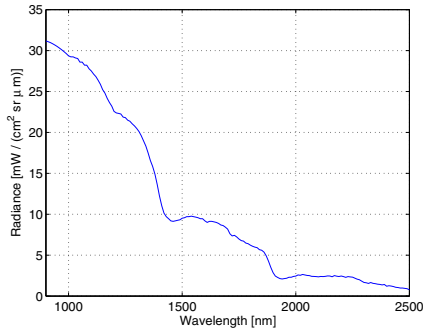
Figure 4.10: Radiance of the integrating sphere with the adjustable lamp at maximum power, and other lamps switched off.

4.2   Radiometric calibration

For the radiometric calibration an integrating sphere was placed in front of the chamber window. The sphere manufactured by Labsphere has four halogen lamps, each with 600 W of power. Three of the lamps are in a fixed position, and one lamp is adjustable with the options of eight different physical positions. By changing the physical aperture of the lamp into the sphere, the intensity of light can be changed without affecting the spectrum of light. The distance between the sphere and the window was about 10 cm, and the total distance to the O-Box inside the chamber about 107 cm. The radiance of the integrating sphere is shown in Fig. 4.10 and the transmission curve of the window is shown in Fig. 4.11.

Measurements (Appendix C) to determine the absolute spectral sensitivity were made at detector temperatures −40°C, −50°C, and −60°C. Linearity with respect to integration time was measured at detector temperatures −50°C and −60°C detector temperature. An absolute spectral sensitivity curve at 120 ms integration time, calculated using the steps listed in Section 3.3. is shown in Fig. 4.12. Absolute sensitivity curves at different integration times normalised by the curve at 250 ms integration time are shown in Figs 4.13 and 4.14 for detector temperatures −50°C and −60°C, respectively. Similar to the SIR instrument calibration the repeatability error is significant after pixel number 200 as is seen in both of these figures. A temperature related effect was seen in the radiometric calibration data: measurements with constant integration time and detector temperature do not remain constant as temperature of the instrument is changing (Figs. 4.15 and 4.16).

In comparison with SIR, the redesigning of the analogue electronics in SIR-2 increased the signal quality considerably. In Fig. 4.17, 300 spectra of a constant radiation field from the integrating sphere have been used to calculate the bias and dark level corrected mean signal and and its noise level, and to represent them as the signal-to-noise ratio for each pixel.
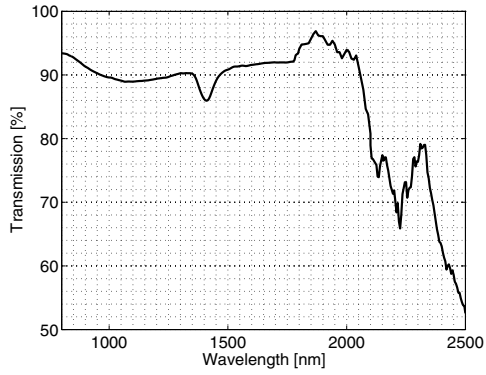
Figure 4.11: Transmission curve of the quartz glass window. There is a small dip at 1410 nm, and after 2000 nm a significant decrease in the transmission.
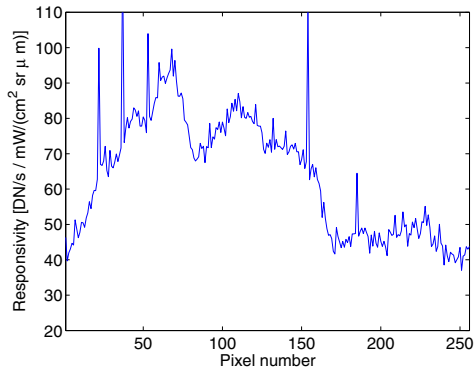
Figure 4.12: Absolute spectral sensitivity curve of the SIR-2 instrument. The detector temperature was $-60°C$, and integration time 120 ms. Pixels 22, 37, 53, 154, and 185 are gray pixels.
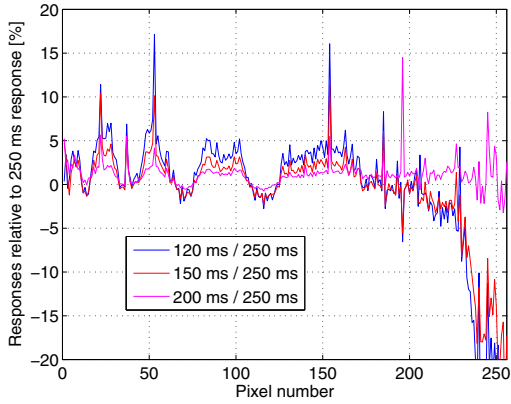
Figure 4.13: Absolute spectral sensitivity divided by the sensitivity curve at 250 ms integration time. Detector temperature was -50 C.
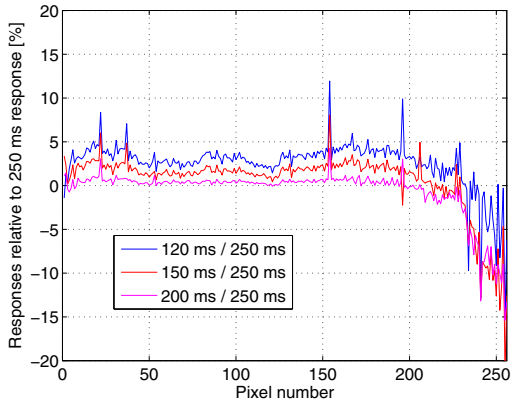
Figure 4.14: Absolute spectral sensitivity divided by the sensitivity curve at 250 ms integration time. Detector temperature was -60 C. The graph shows clearly that the noise in SIR-2 data is less than in SIR data. The curves are not directly comparable due to different input of two integrating spheres.
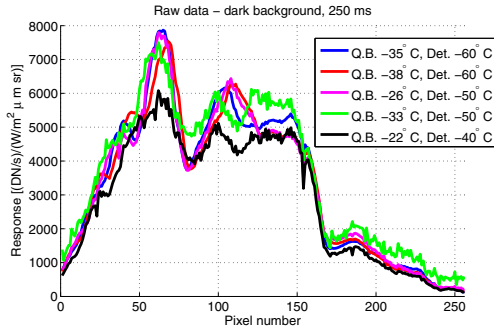
Figure 4.15: Output signal of SIR-2 when illuminated by an integrating sphere with constant light level and constant integration time of 250 ms. The detector temperature has been changed by the active controller and also the core optics temperature (QB=quartz body) was different in the the measurements compared. An undesired temperature related effect changes the shape of the output spectrum. This is observed at different QB temperatures at the same detector temperature (blue and red or magenta and green lines).
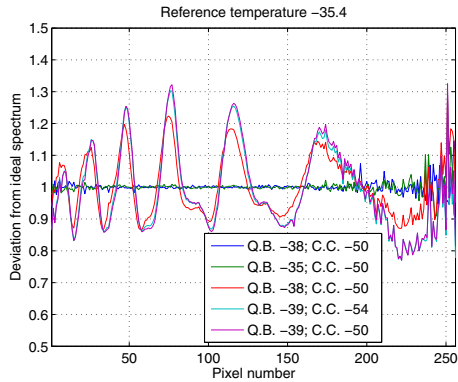
Figure 4.16: SIR-2 output (an average of 500 to 1000 spectra, depending on the recording) divided by an output at a reference temperature. This shows that the temperature related effect at constant detector temperature ($-61.1°C$) depends on the temperature of the other parts of the instrument than the semiconductor detector (CC = cooling console).
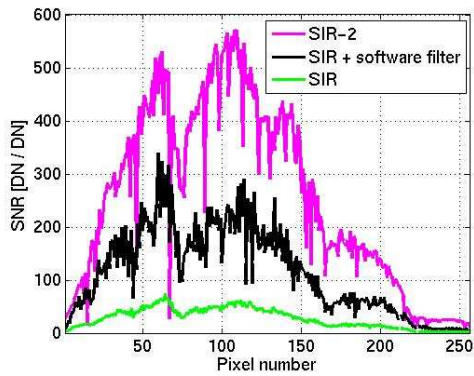
Figure 4.17: The improved signal-to-noise ratio of SIR-2 has been achieved because of the redesigned analogue electronics. A digital filter (Section 5.1) improves the original SIR signal considerably.

Table 4.1: Ranking of the three detectors tested. Detector no. 06C4548 is the best in five out of six tests and always among the best two detectors.

Test	Best	Second best	Third
Hot, grey, dead, unstable, and anomalous pixels	06C4548	06C4547	06C4546
Minimum and maximum relative noise	06C4548	06C4546	06C4547
Signal-to-noise ratio	06C4548	06C4547	06C4546
Nonlinearity with respect to integration time	06C4546	06C4548	06C4547
Dark count rate nonlinearity	06C4548	06C4546	06C4547
Photo response nonuniformity	06C4548	06C4547	06C4546

4.3   Detector comparison

There were three individual detectors of type Hamamatsu G9208-256W as potential choices to be used in the flight model and the flight spare model of SIR-2. To assess and rank the detectors, a measurement set-up was built to use one detector at a time with a controlled light source illuminating the InGaAs semiconductor array directly without the spectrometer part. A very small thermal vacuum chamber encasing the detector was placed in a test chamber with a LED light source operating in ambient pressure (Fig. 4.18). The measurements were carried out at detector temperatures between $-50°$C and $-20°$C with intervals of 5°C and using integration times ranging from 0.1 to 250 ms. The properties investigated in this study were the following:

- Find hot, dead, and gray pixels

- Estimate the photo response nonuniformity of each detector array

- Find pixels with irregularities in dark background level versus temperature behavior

- Find pixels with higher-than-average noise characteristics (low SNR)

- Estimate for each pixel the linearity with respect to integration time

The photo response nonuniformity of detector 06C4546 is shown in Fig. 4.19. The comparison is outlined in Table 4.1. The potential SIR-2 flight model that was calibrated in India included detector number 06C4547, which is the second best in the comparison; the other potential SIR-2 flight model had detector number 06C4546.
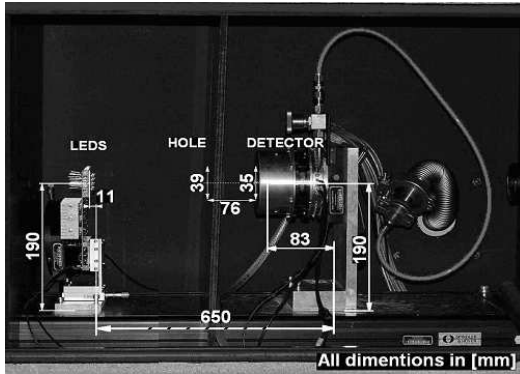
Figure 4.18: Test chamber for NIR detectors. The peak wavelengths of the five LEDs are 1.05, 1.35, 1.55, 1.75, 2.05, and 2.35 μm. The LEDs were in a fixed position, the mechanical tolerance of the detector positioning is ± 2 mm (adopted from Sitek et al. 2007).
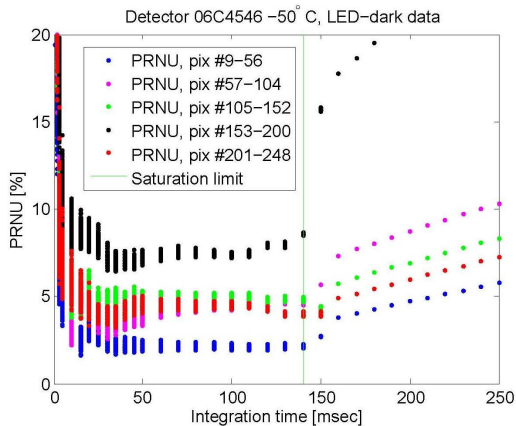
Figure 4.19: Worst case example of photoresponse nonuniformity. The 240 of the 256 pixels of detector 06C4546 have been taken into account; they are divided into five blocks (the colors) and for the pixel in each block the relative difference of output values within that block are plotted as a function of integration time. The input light had the same spectrum for each pixel. The green vertical line shows the saturation limit, after which values of PRNU are not taken into account.
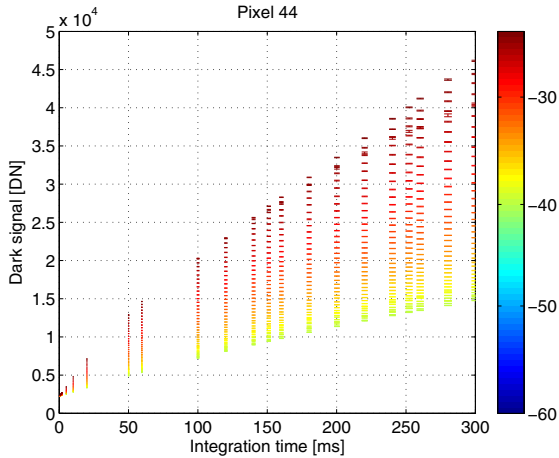
Figure 4.20: Dark measurements as a function of integration time and temperature. The temperatures are color coded in degrees centigrade.

4.4   The bias and the background level

The same principles of characterising the bias and dark counts that were used in calibrating the SIR instrument are directly applied to the SIR-2 instrument; these are explained in Section 3.5. During the session dedicated to dark measurements the temperature of the detector was not actively stabilized for safety reasons: the detector temperature set by the active controller in SIR-2 was not allowed to deviate from the cooling console temperature more than a specified safety limit. The measurements of one pixel are shown in Figure 4.20. For the bias and dark count rate calculations the data have been divided over the range of temperatures into 33 bins between $-40.5°$C and $-24.0°$C, with bin size of half a degree. Each temperature bin has 26 to 54 measurements at 26 different integration times ranging from 0.5 to 300 ms. The bias values of the 256 pixels are shown in Figs. 4.21 and 4.23: they show similar behavior as a function of pixel number at different temperatures. The lower overall level compared to SIR (its bias was more than 14000 DN) is due to changes in the electronics from SIR to SIR-2. The three sigma error estimates are small compared to the actual values as shown normalised to zero in Fig. 4.23.

The background signal without any incoming light is shown for three pixels in Figure 4.24. A major advantage of the active temperature controller in the detector is that when operated at temperatures where the dark background has been measured it is enough to subtract the laboratory dark of the same temperature in DN units from the instrument output in DN units; no modeled dark counts need to be calculated contrary to the SIR case.
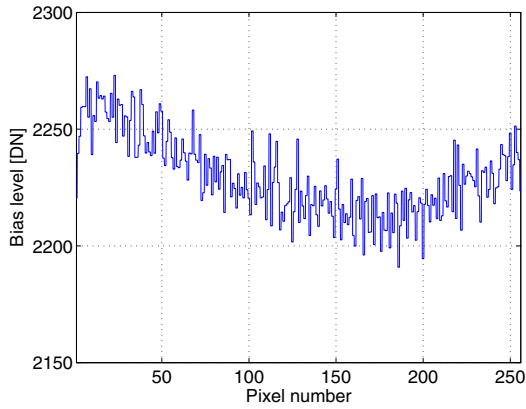
Figure 4.21: The bias values of the SIR-2 instrument. The values are an average at −40.5°C, −40.0°C and −39.5°C. Comparison with the SIR instrument (Fig. 3.24) shows that the bias is remarkably lower.
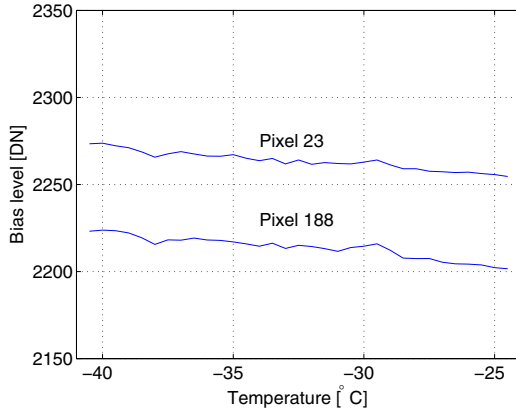
Figure 4.22: Bias values of pixels 23 and 188 as a function of temperature. There is a slight temperature dependence in the estimates, which is similar for all pixels.
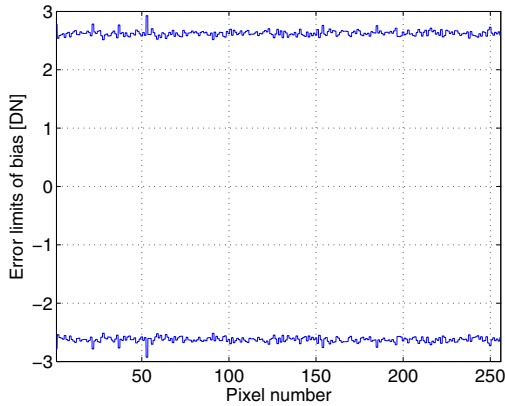
Figure 4.23: The three sigma error estimates of bias values.
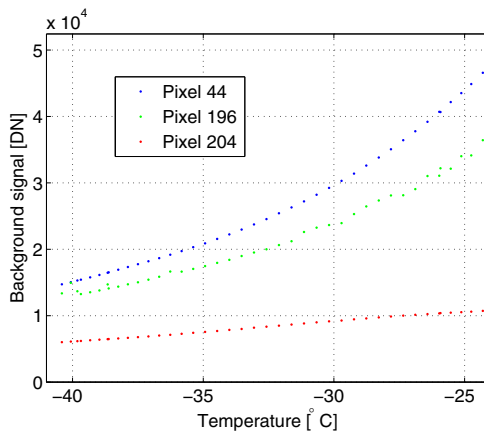
Figure 4.24: Dark background measurements of pixels 40, 196, and 204 as a function of temperature at integration time 300 ms. The DN scale (y-axis) is 80% of the full dynamic range. Pixel 40 (like 94% of all pixels) shows nominal behavior (see also Fig.4.20), pixel 196 is unstable (random jumps in signal level), and pixel 204 shows anomalous behavior as a function of temperature.

5 Data reduction

The SIR spectrometer was calibrated in laboratory conditions in 2002, two and half years before the start of its scientific mission. The spacecraft had travelled through Earth's radiation belts 150 times during the 16 month journey after it was launched in September 2003. The spectral response was expected to have changed from that measured in the laboratory both during the journey and while orbiting the Moon. For instance, during the Clementine mission to the Moon in 1994, the preflight calibration of the NIR camera had to be "heavily corrected", and there was a detector sensitivity drift which changed the calibration of the UVVIS camera from month to month (Shkuratov et al. 2001). Inflight calibration may use stars, planets, solar corona or areas on the Moon where ground based observations, or samples from the Apollo landing sites, exist.

Data reduction procedure

The data reduction is carried out by a specific software developed during this work using MATLAB, which is a language for technical computing and visualisation. The main functions of the data reduction routine are:

- Filtering of noise spikes

- Correction of the bias level (offset)

- Correction of the contribution of dark counts

- Absolute sensitivity calibration

- Division of the spectrum by the solar irradiance

- Division of the spectrum by the photometric function

- Transformation to reflectance factor

- Multiplication by an inflight correction factor

- Optional filtering

The bias level and dark count corrections are discussed in Chapter 2. Either preflight calibration data, together with temperature data from the detector or so called flight dark background measurements are used to make this reduction. After the absolute sensitivity calibration step the spectrum is expressed in the units of spectral radiance. To get the reflectance factor, the spectra are further divided by the solar irradiance and the Lambert

reflectance, and a necessary correction for the observation geometry is applied. If only relative spectra (spectra from one orbit divided by the mean spectrum of a reference area from the same orbit) are required, the necessary and sufficient steps of data reduction are: i) noise filtering, ii) bias correction, iii) dark background correction, and iv) applying the photometric function for reducing the spectra to a standard viewing geometry.

Instrument output

The reflectance factor can be written as (Equations 1.2, 1.4 with $A_L = 1$, and 1.5):

$$\text{REFF}(i, e, \alpha) = \frac{\pi}{\cos(i) \, J(i, e, \alpha)} L(i, e, \alpha). \tag{5.1}$$

The instrument output after the absolute sensitivity step of data reduction is given in the units of reflectance factor at the illumination geometry of the observation. Taking this into account the reflectance factor is rewritten as:

$$\text{REFF}(i, e, \alpha) = \frac{\pi}{\cos(i) \, f(i, e, \alpha) \, J} L_{SIR}, \tag{5.2}$$

where f is the photometric function defined in Section 5.4 and L_{SIR} is the instrument's output. It should be observed that this result has been normalized to zero phase angle. Another common normalisation is $(i, e, \alpha) = (30°, 0, 30°)$, which is used by the Clementine mission and many laboratory lunar regolith or reference spectra. In order to change the normalization Equation 5.2 is multiplied by $f(i', e', \alpha')$, where i', e', and α' are the incidence, emergence and phase angles of the new normalisation.

Finally, the spectrum of reflectance factor may need to be filtered in order to remove pixel-to-pixel noise. The trade-off is then reduced spectral resolution. For example, if a 9-pixel long median filter is applied, the narrowest absorption band that can be distinguished is 30 nm wide.

5.1 Noise filtering

A characteristic of the SIR electronics is that each pixel has noise peaks seen as abnormally high or low DN value, which appear randomly and infest about 30 or 60 pixels at a time as shown in Figs. 5.1 and 5.2. Because of this, the first phase of data reduction is a two-stage filter applied to each pixel individually: first the data are divided into blocks of, for instance, 100 spectra; then each block is filtered with a three-pixel median filter. If a filtered value deviates from the unfiltered one more than 40% of the standard deviation over one block, then such a value is discarded from the data set. In the second stage, a five pixel median filter is used and the limit is the standard deviation of the reduced data block after the first stage. The example data of Fig. 5.2 after filtering, is shown in Fig. 5.3. Another property of the SIR electronics is that sometimes a pixel value has jumps of 400-600 DN upwards from the expected value. An example of these sort of jumps is shown in Fig. 5.4.
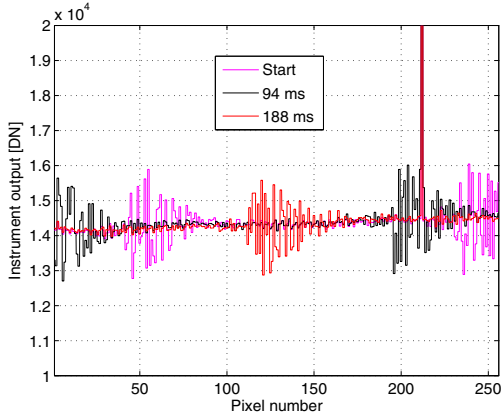
Figure 5.1: Appearance of noise spikes as sets of disturbance wavelets in three consecutive spectra; the integration time was 0.5 ms and detector temperature $-30°C$. The time of recording is shown in the legend.
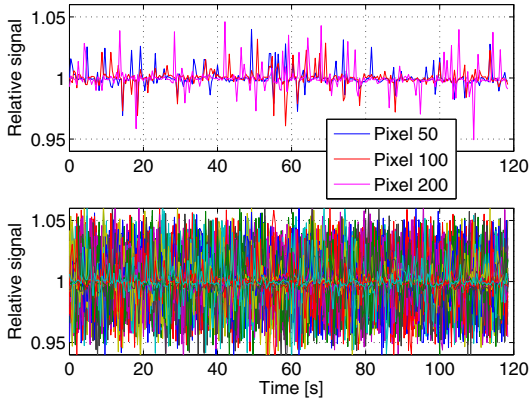
Figure 5.2: Unfiltered measurement of a constant light source. The instrument was looking into an integrating sphere for two minutes recording 300 spectra with integration time 252 ms. All spectra are divided by the first spectrum, so that in an ideal case the response should be 1. The upper graph shows selected pixels whereas the lower graph is a combination of all pixels.
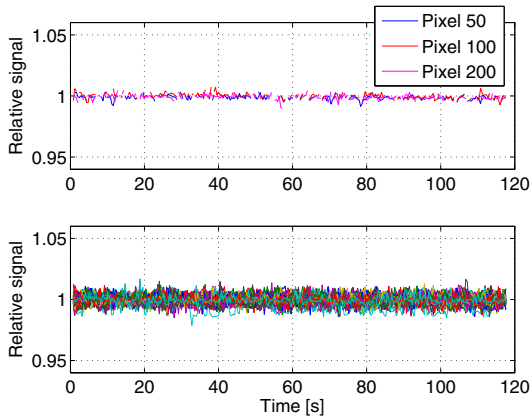
Figure 5.3: The data from Fig. 5.2 after noise filtering. With a noise level of less than 0.01, the signal-to-noise ratio has been improved by 25 dB by the two-stage median filtering process.
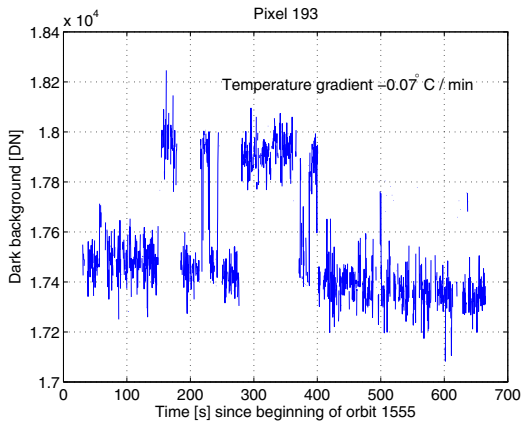
Figure 5.4: An example of DN value jumps due to the electronics.
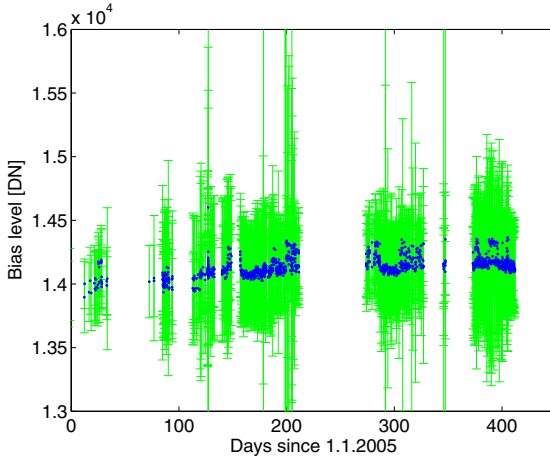
Figure 5.5: Bias values of pixel number 50 from flight data measurements with short integration times. The errorbars show the standard deviations of unfiltered data, which are significantly larger than in the laboratory bias.

5.2 The bias level and the dark count rate

The bias is the digital reading that the instrument gives at zero integration time. During the SMART-1 mission very short exposures were taken typically at the beginning of an orbit; sometimes an entire orbit was dedicated to those measurements taken with 0.0655 ms or 0.1311 ms integration time. The bias estimates for one pixel are shown in Fig. 5.5. There is a small variation of about 1%, which correlates with changes in detector temperature (Fig. 5.6). According to laboratory measurements of dark count rate at $-50°$ C the rate is $< 40 \frac{DN}{ms}$ for almost all pixels (Fig. 3.26), which means only about five DN counts in the estimated bias measurements. Thus, observations at an integration time of 0.1311 ms give a reliable estimate of the bias.

During the calibration measurements of the SIR instrument the bias level and the dark count rate were analysed separately. This was done to investigate the contribution to the total count rate of both sources of digital counts. During the SMART-1 mission, part of an orbit was sometimes dedicated to a dark measurement by either looking at empty space or the non-illuminated side of the moon; there are 43 such orbits. When the sum of calculated bias and dark counts is compared to the background measured during the mission, it becomes evident that some refinement is needed. This is partly due to the fact that temperatures during the mission (usually between $-70°$ C and $-50°$ C) are lower than during the calibration measurements (from $-55°$ C to $-15°$ C). An example where only a
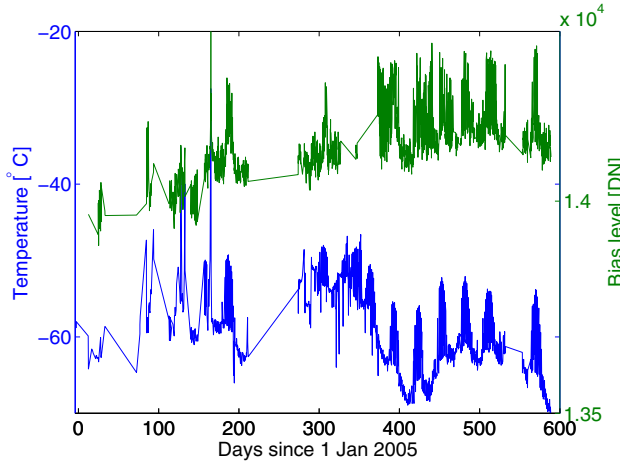
Figure 5.6: Measured biases (upper curve) and detector temperatures (lower curve) during the mission for pixel number 50. Similar behavior is seen with the other pixels. The changes in bias level are of the order of 1%.

slight refinement is required is shown in Fig. 5.7. The data has also been used to identify pixels which have became defective since the laboratory calibration. The characteristic of a defective pixel is that it suffers from an abrupt step in its background level when compared to other orbits. One such case is pixel number 18, which is shown in Fig. 5.8, the others are pixels 41, 65, 102, 117, 124, 145, 149, 187, 204, and 243. The new parameters based on flight dark data are fitted to a modified version of function 3.13:

$$I = d + aT^b e^{\frac{c}{T}}, \tag{5.3}$$

where T is temperature in Kelvins, and a, b, c, and d are the new fitted parameters whose numerical values are given in Appendix D. New fits have been made to all pixels.
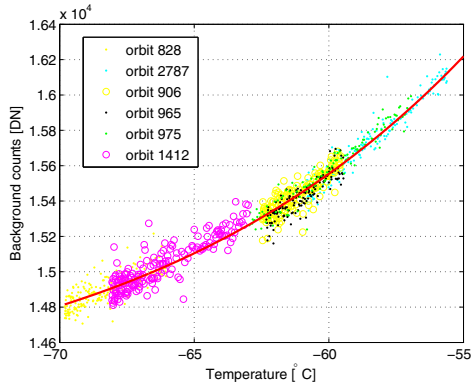
Figure 5.7: Flight dark background of pixel 33. The red solid line is the laboratory background level. The electronics noise has been filtered out from the data.
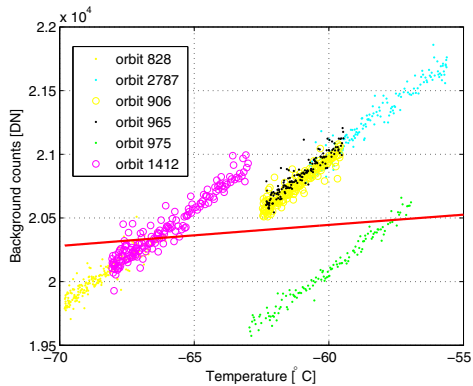
Figure 5.8: Flight dark background of pixel 18. The red solid line is the laboratory background level. The electronics noise has been filtered out from the data.
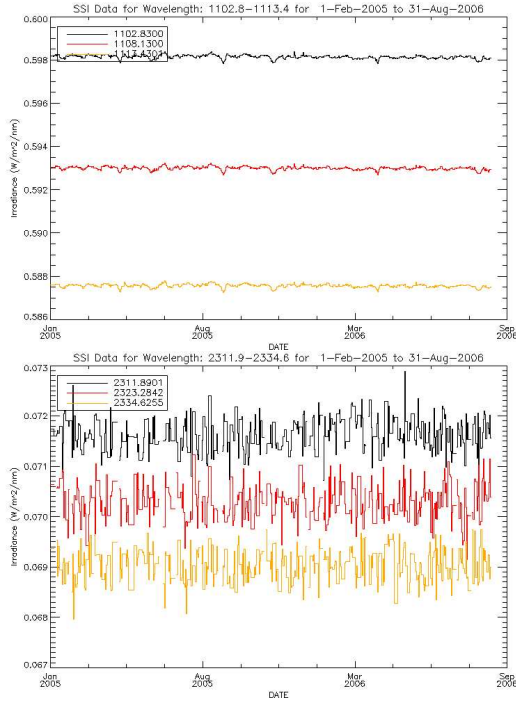
Figure 5.9: Solar variability at 1103 nm, 1108 nm, and 1113 nm (upper panel), as well as 2312 nm, 2323 nm, and 2335 nm (lower panel). The data were measured by the SORCE (Solar Radiation and Climate Experiment) spacecraft's SIM (Spectral Irradiance Monitor) instrument (SORCE data, 2008).

5.3   Solar irradiance model

The irradiance assumed is the ASTM E-490 standard (Fig. 2.5). During the SMART-1 mission when the SIR instrument was operating solar activity was decreasing, which resulted in a slight decrease in all wavelengths other than between 1 and 3 μm, where irradiance is actually increasing when approaching solar minimum (Fig. 5.9). However, the trend during the mission from February 2005 to September 2006 was negligible compared to daily variations and the range of variability was smaller than 2% even at the more variable wavelengths. More important effect than the changing solar variability is the changing Sun-Moon distance, which causes a ±4% change in the overall level with time periods of two weeks.

5.4   Photometric correction and Shkuratov's model

The conditions of illumination geometry have an effect on the overall brightness and the continuum slope of an observed spectrum. In order to bring the observed spectra to the same photometric conditions a photometric correction is applied, which depends on the geometry of illumination as well as on the properties of the surface (see Section 1.2.2).

The photometric function is the ratio of the bidirectional reflectance (Equation 1.2) observed at a fixed angle of emergence e, but varying i and α, to its value at zero phase angle (Hapke 1993):

$$f(i, e, \alpha) = \frac{r(i, e, \alpha)}{r(e, e, 0)}.$$ (5.4)

The photometric function used here is the semi-empirical Shkuratov function in the form $f(\alpha, b, l) = H(\alpha) D(\alpha, b, l)$, where D is the Akimov disk function (no parameters) and H (three parameters) contains the shadow hiding part and the coherent backscatter part (Shkuratov et al. 1999). This is a convenient way to separate the phase angle dependence from the other angles when a fractal like particulate surface is illuminated. The H function depends on the phase angle α, and Akimov's disk function depends on the phase angle as well as on b and l, the photometric latitude and longitude, respectively. These angles are calculated from the angles of incidence and emergence by the following relations (Kreslavsky et al. 2000):

$$\tan l = \frac{\frac{\cos i}{\cos e} - \cos \alpha}{\sin \alpha}$$ (5.5)

$$\cos b = \frac{\cos e}{\cos l},$$ (5.6)

where the photometric latitude b is the angle between the normal of the lunar surface and the scattering plane, while the photometric longitude l is the angle in the scattering plane (determined by source, surface point and observer) between the projection of the normal on the scattering plane and the direction from the surface element to the observing instrument. The planes of incidence and emergence are parallel only in special cases, and there is a relation between the angle between the planes ψ and the phase angle and the angles of incidence and emergence (Shkuratov et al. 1999):

$$\cos \alpha = \cos i \cos e + \sin i \sin e \cos \psi.$$ (5.7)

The angles covered during the SMART-1 mission are shown in Fig. 5.10 and Fig. 5.11.

The brightness distribution over the lunar disk by Akimov is (Shkuratov et al. 1999):

$$D(\alpha, b, l) = \frac{\cos\left(\frac{\pi}{\pi - \alpha}\left(l - \frac{\alpha}{2}\right)\right)}{\cos l} (\cos b)^{\frac{\alpha}{\pi - \alpha}}.$$ (5.8)

Akimov's disk function at photometric longitudes 0, 30° and 60° are plotted in Fig. 5.12. When $\psi = 180°$ the incident direction and the emergent direction are on opposite sides of the surface normal, when $\psi = 0$ they are on the same side of the normal.

The phase function H is (Shkuratov et al. 1999):

$$H(\alpha) = \frac{\exp(-k\alpha)}{2 + \exp\left(-\frac{d}{L}\right)}\left(2 + \frac{\exp\left(-\frac{d}{L}\right)}{\sqrt{1 + \left(\frac{4\pi L}{\lambda}\sin\frac{\alpha}{2}\right)^2}}\right),$$ (5.9)
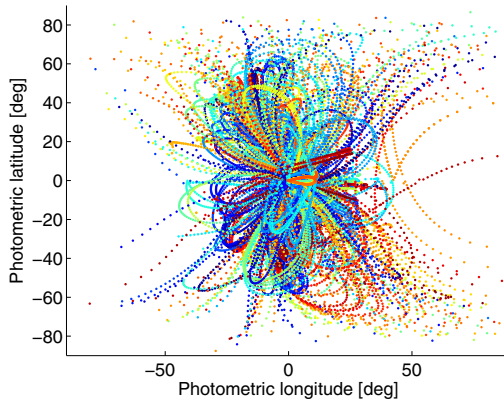
Figure 5.10: Coverage of photometric latitude and longitude space during the SMART-1 mission.
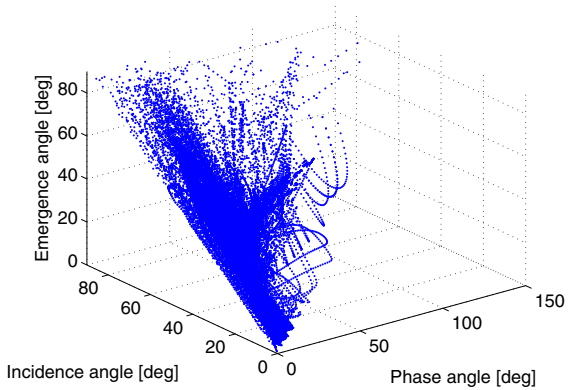
Figure 5.11: Phase, incidence and emergence angles of spectra measured during the SMART-1 mission.
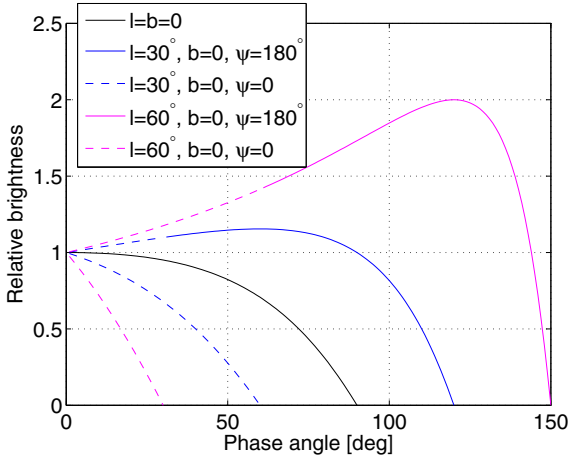
Figure 5.12: Akimov's disk function at different geometries with zero photometric latitude (scattering plane perpendicular to the surface), that is the photometric longitude equals the angle of emergence. The angle of incidence is calculated from relation 5.7. ψ is the angle between the plane of incidence and the plane of emergence. The apparent ambiguity (dotted lines below the $l = b = 0$ curve) is due to angles of incidence larger than angle of emergence in cases where incidence and emergence are on the same side of the normal ($\psi = 0$); these are sometimes defined as negative phase angles.

where d is the radius of the volume in which single scattering is formed, and no coherent backscatter effect takes place. If the characteristic size of particles is of the order of, or less than, the wavelength λ, then it is assumed that $d \approx \lambda$. If the particles are much larger than λ and structureless, then d is the effective radius of the particles. L is the characteristic scale of light diffusion characterizing the attenuation of light due to absorption and scattering. The coherent backscatter part with the d and L parameters is important in modelling the opposition effect at small phase angles, where the behavior of the H function relates to surface irregularities in the size of the mean lunar soil particle size. The term $\exp(-k\alpha)$ describes the shadow hiding effect, which is a geometric optics effect having the main role in the photometric studies of regoliths. It is assumed that the effective roughness coefficient k depends on the albedo A as $k = k_0(1 - A)$, where k_0 does not depend on the albedo.

The parameters k, d, and L of Equation (5.9) have been estimated by fitting Clementine visible wavelength data from three channels 0.415 μm, 0.750 μm, and 0.950 μm (Shkuratov et al. 1999); they used an average of overlapping images with different phase angles, ranging from 3° to 50°. The latitude on the Moon was restricted to ±50°, because at higher latitudes the Sun is always low and local topography has a profound effect on

Table 5.1: Spectral dependence of the Shkuratov function parameters at $\frac{d}{\lambda} = 1.5$. Modified from Table I of (Shkuratov et al. 1999).

λ [μm]	k	$\frac{L}{\lambda}$	k_0
0.415	1.042	3.33	1.20
0.750	0.871	6.01	1.01
0.950	0.813	6.09	0.95
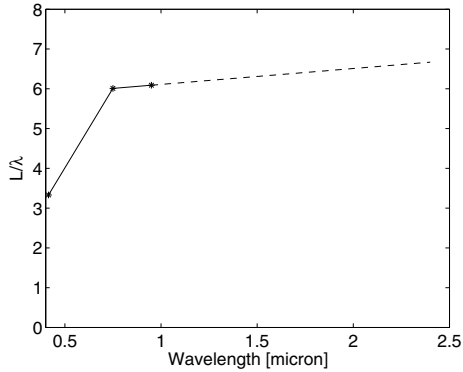
Figure 5.13: Shkuratov function parameter $\frac{L}{\lambda}$ extrapolated into NIR.

the apparent radiance. Several parameter values gave a good fit, so first a value for d was set so that $\frac{d}{\lambda} = 1.5$. Under that constraint k and L were fitted. The results of (Shkuratov et al. 1999) are shown in Table 5.4. For NIR the values of $\frac{L}{\lambda}$ are extrapolated with the help of the 0.75 μm and 0.95 μm values as shown in Fig. 5.13. The roughness parameter k depends on the albedo A of the surface as well as on surface properties, which are independent of albedo: $k = (1 - A)k_0$, where k_0 does not depend on albedo. The lunar albedo at visible wavelengths has been widely observed, and it can be extrapolated using the model 2.1; using this model the values of k_0 corresponding to the fitted values of k are calculated in the last column of Table 5.4. In the first approximation the extrapolated value of $k_0 = 0.85$ is used here, and it is assumed to be constant within the instrument's wavelength range. The values of the phase function $H(\alpha)$ at different phase angles are illustrated in Fig. 5.14.

Another way to estimate the roughness parameter is to use the SIR data from the SMART-1 mission and do a fit. For this purpose 15 areas (Appendix E) on the Moon have been selected with the criteria of having several recorded spectra from the same location and with changing phase angle (Figs 5.15 and 5.16). In this work no model for albedo is needed because it is estimated from the data, too. Using the 15 areas an estimate for the parameter is: $k = 1.07 - 1.5 \times 10^{-4}\lambda$, where λ is the wavelength in nm within the range $1080 < \lambda < 2240$.
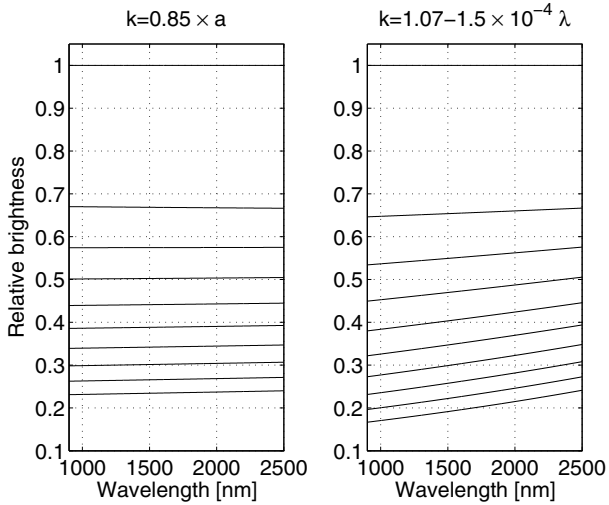
Figure 5.14: Shkuratov phase function $H(\alpha)$ using two different approaches of the shadow hiding parameter. The phase angles range from 0 to 90° from top to bottom with steps of 10°. Observe the reddening due to the shadow hiding part at high phase angles. Albedo a was calculated from model 2.1. This model may give a too modest spectral slope (see Fig. 2.6), thus the parameter on the right hand side figure is recommended to be used.
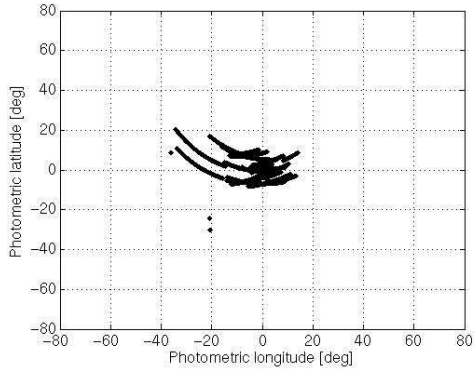
Figure 5.15: The photometric coordinates of all spectra from the 15 sites used to estimate the value of the shadow hiding parameter k.
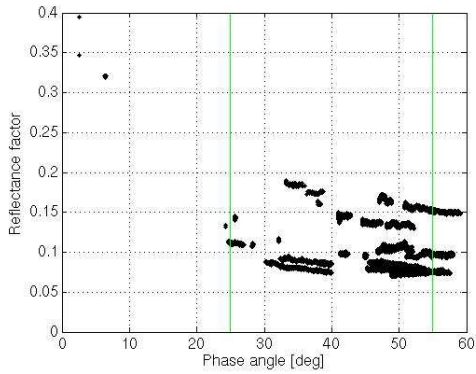
Figure 5.16: The phase angle dependence of reflectance factor of all the 15 sites used to estimate the value of the shadow hiding parameter k.

5.5   Inflight calibration

The SIR instrument, because of its requirement of light weight and compact size, does not have any diffuser plate or other equipment for inflight calibration. The only possibility is to observe objects whose radiance is well known by telescopic observation or by returned samples. Two approaches have been tried during the SMART-1 mission: target tracking of Apollo landing sites and observations of Jupiter, Sirius and Vega.

5.5.1   Apollo landing sites

On orbits number[1] 366 and 368 the SIR instrument observed the Apollo 16 landing site in a target tracking mode, that is by keeping the pointing approximately on the same area on the lunar surface. A subset of these observations were selected so that the center point of the footprint remained within an area of 290 m × 40 m. The pointing on the surface and the average footprint size are illustrated in Fig. 5.17. The angles of incidence, emergence and phase are shown in Figs. 5.18 and 5.19. The difference in emergence angles of the two orbits is about 5°, and less than that for the phase and incidence angles. The resulting difference in the calculated photometric function between the two orbits is about 0.5%. A multiplicative correction factor is calculated using Apollo 62231 soil sample (also used by the previous Clementine mission), which was taken from a location less than 6 km southeast of the SIR observation (Fig. 5.20). The difference between the two SIR observations is about 5%. The disadvantage of this calibration correction is that the sample is not from exactly the same location as the observation. Furthermore, a comparison to other Apollo sites and samples shows that there is a difference in the absolute level of the correction if it is calculated using a different Apollo sample (Fig. 5.21).

---

[1]Numbering of orbits in the SIR data is defined from perilune to perilune until orbit number 1341, and from apolune to apolune thereafter.
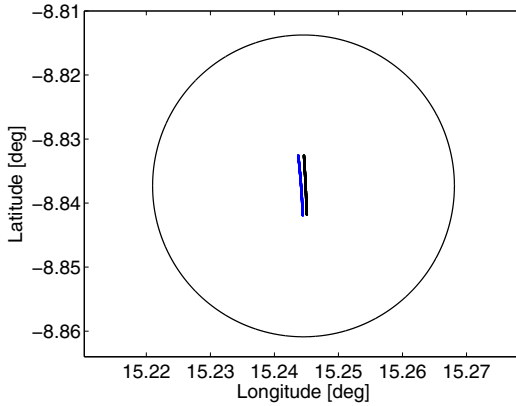
Figure 5.17: Target tracking observations of an area near the Apollo 16 landing site at a highland near the Cayley plains and the Descartes mountains. The two tracks shown are parts from orbits 368 (March 28, 2005) and 366 (March 27, 2005), from left to right respectively. The circle shows the average size of the footprint, which is 1.4 km.
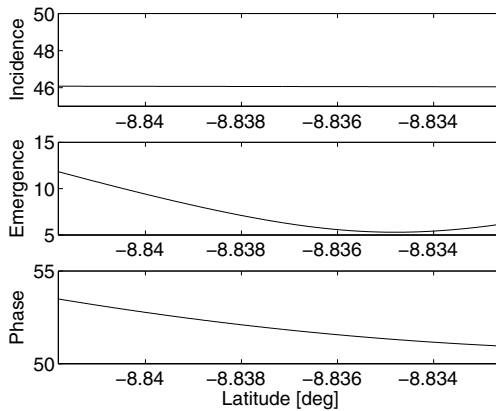
Figure 5.18: The angles of incidence, emergence and phase of the SIR observations from a part of orbit 366 of the Apollo 16 landing site in target tracking mode. The angle of emergence varied less than 7° and the phase angle varied less than 3°.
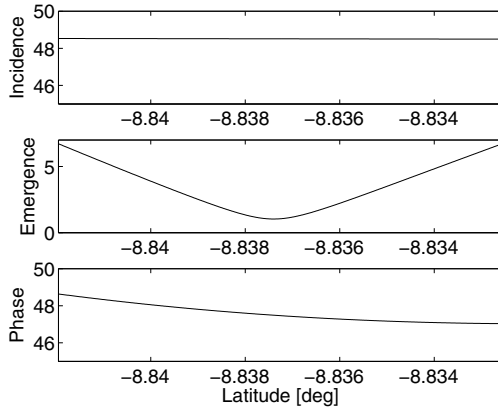
Figure 5.19: The angles of incidence, emergence and phase of the SIR observations from a part of orbit 368 of the Apollo 16 landing site in target tracking mode. The angle of emergence varied less than 6° and the phase angle varied less than 2°.
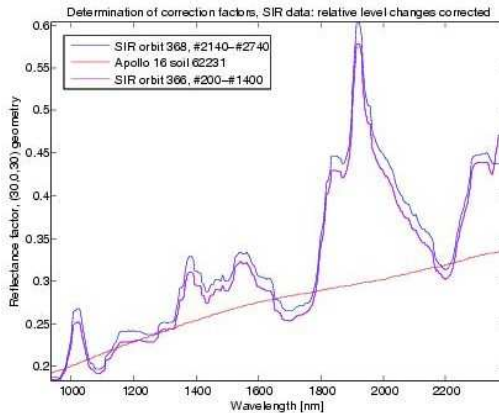
Figure 5.20: SIR observation of Apollo 16 landing site from two orbits and the laboratory measurement of soil sample 62231 (RELAB/ Brown University).
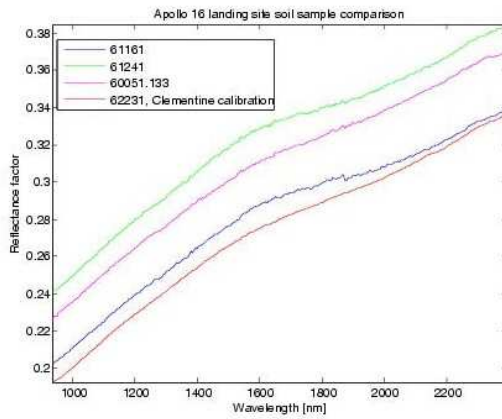
Figure 5.21: Differences between lunar soil samples near Apollo 16 landing site. The different levels are due to different locations as well as to the processing of the samples before measuring at laboratory conditions. Data from RELAB (Brown University).

5.5.2   Celestial objects

When celestial objects, other than the selected sites on lunar surface which fill the field of view of the instrument, are used for calibration purposes the radiance of the source should be strong enough to be detected by SIR. In order for the signal to be on the linear range of the instrument its power should exceed 1.4 pW as calculated in Section 3.3. Another constraint is the pointing accuracy; since the instrument is fixed the whole spacecraft had to be re-oriented. The accuracy of pointing was only about 4.5 mrad for two axis and 18 mrad for the third (SIR team 2000), whereas the field of view of SIR is 1.1 mrad. The relative pointing accuracy over 100 ms is about 0.05 mrad, which is accurate enough. For this reason the target had to be observed on several occasions with a slightly different pointing of the spacecraft. In total, there are 11 orbits for Jupiter, 7 for Sirius, and 3 for Vega.

The spectral radiance per unit wavelength measured by the NIMS instrument (Section 1.4.1) onboard the Galileo spacecraft shows that Jupiter's radiance is highly varying depending on the wavelength. It has maxima of 250, 150, 90 and 23 $\frac{\mu W}{cm^2\, sr\, \mu m}$ at 1.05, 1.3, 1.6 and 1.9 μm, respectively (Irwin et al. 1998). Between the maxima there are steep minima, each less than 12 $\frac{\mu W}{cm^2\, sr\, \mu m}$. The signal power P received from Jupiter according to Equation 2.3 is

$$P(\lambda) = L_\lambda(\lambda)\, \Delta\lambda \Omega_{Jup} A_{SIR}, \qquad (5.10)$$

where L_λ is the radiance per unit wavelength, $\Delta\lambda = 6$ nm is the spectral sampling, $\Omega_{Jup} = 23.1$ nsr is the solid angle of Jupiter seen by SIR, and $A_{SIR} = 40.7$ cm^2 is the instrument's aperture area. The signal power received from Jupiter is on the order of 1.5 pW, which is at the limit of linear operation of the instrument but due to noise in the observations the signal is too weak. The radiances of Sirius and Vega are even less than Jupiter's so they were unuseful in checking the calibration.

At the very end of the SMART-1 mission the spacecraft was pointed at the Sun but this caused the saturation of almost all pixels and could not be used for inflight calibration either.

6 Sample spectra from selected lunar sites

6.1 Comparison with Clementine data

The Clementine mission carried on board two cameras, one for visible and the other for NIR wavelengths (Section 1.4.2). This data, albeit from only a few filter channels, can be used to adjust the overall level of the SIR reflectance factor calculated using the steps explained in Chapter 5. This reflectance factor appears somewhat lower than the Clementine data (Fig. 6.1) due to differences in the data reduction procedure. Furthermore the temperature related effect present already in the ground calibration (Fig. 3.12) is present in the SIR spectra of orbits 2374 and 2506. This effect can be overcome by using spectra from a reference area in the same orbit and calculate a relative spectrum.

6.2 Relative spectra of Reiner Gamma

Relative spectra are useful in absorption identification because absorption features are relatively weakly observed in spectra presented in units of reflectance factor, relative spectra are useful in absorption identification. Spectra measured on the Reiner Gamma swirl are divided by a reference spectrum, which is an average of tens of spectra taken on an area outside the swirl where prominent absorptions are not expected.

Swirls are albedo features of bright and dark material on the surface without an apparent corresponding topographic feature; they also have diffuse boundaries and magnetic anomalies associated with them. Swirl patterns range in size from 50 m to 10 km across and form ribbon-like patterns as well as open and closed loops. Sometimes the swirl patters form a larger fan-shaped system of such patterns which extends hundreds of kilometers from the core feature; the distribution of these swirls provide a clue on the direction of the assumed cometary impact and the dust and gas tails of the impactor (Schultz and Srnka 1980). The most investigated swirl on the Moon is Reiner Gamma (5° S, 60° W) on the nearside (Fig. 6.2), since the other swirls are on the farside of the Moon, near Mare Marginis (15° N, 90° E) and Mare Ingenii (35° S, 180° E). There have been many theories about their origin: they have been considered volcanic ash deposits, volcanically derived sublimates, highland debris from impact ejecta, or the results of magnetic shielding of fresh mare materials from the solar wind ion bombardment (Basilevsky et al. 2004). Other theories suggest that they are remains and imprints of recent cometary impacts, less than 100 million years old, and that the magnetic field associated with them is of cometary
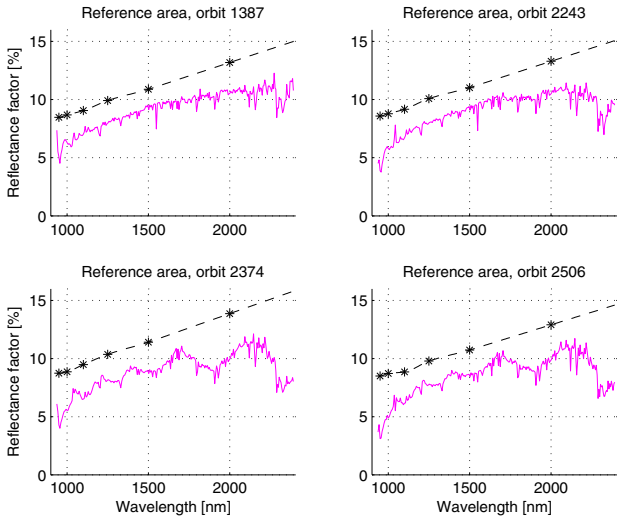
Figure 6.1: SIR observations (magenta) compared with the earlier Clementine mission; the six Clementine channels (*) are used to interpolate a spectrum at the SIR wavelengths. The reference areas are in Oceanus Procellarum north of Reiner Gamma.

origin.

   Relative spectra from four orbits over the Reiner Gamma swirl are shown in Fig. 6.3. The reference areas are from the same orbits but beyond the area shown in the figure. The overall relative spectra show that the swirl is 20 to 70% brighter than the reference area. Furthermore, the relative spectra have negative slopes, which indicate that they are spectrally bluer than the reference area. A well known effect of space weathering (e.g. micrometeorite impacts, solar wind particles, galactic cosmic rays) modify the reflectance properties of the lunar regolith over time, leading to darkening of the visible spectrum, reduction of the absorption bands, and an increase in the continuum; these factors modify the reference spectrum. The effect of 1 μm and 2 μm absorption bands is seen in the middle spectrum of orbits 2243 and 2506.
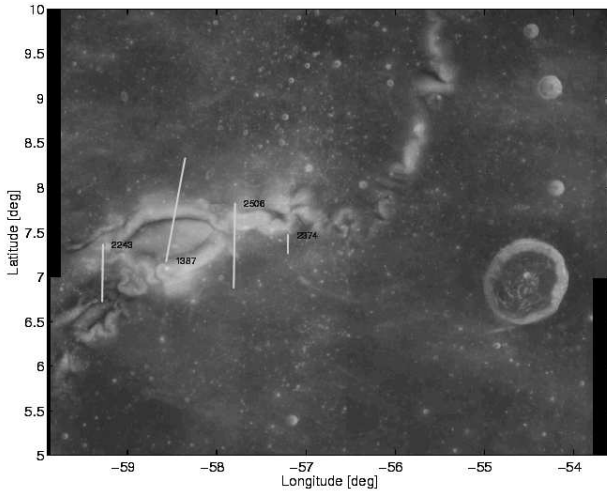
Figure 6.2: Reiner Gamma Swirl at 1.5 μm wavelength. The locations of four selected parts of four SIR orbits are shown as yellow line. The coordinates used by the Clementine mission differ somewhat from the coordinates used by SIR. The flight direction is south to north for orbit 1387 and north to south for orbits 2243, 2374, and 2506. Photo courtesy of NASA / Clementine mission.
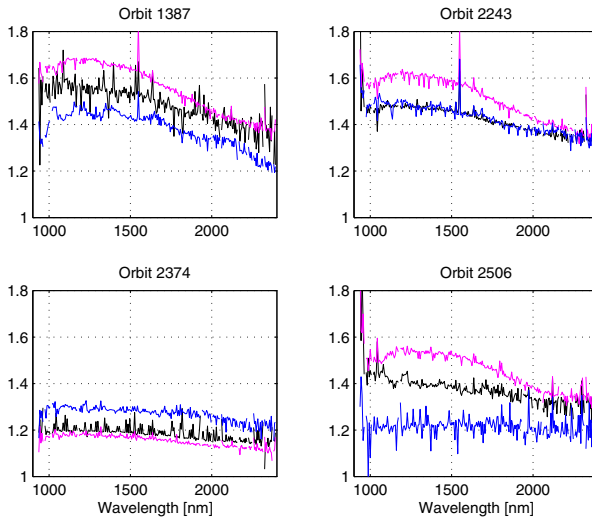
Figure 6.3: Relative spectra over Reiner Gamma from the fractions of orbits shown in Fig. 6.2. The spectra are from the beginning of the fraction (black), from the middle (magenta) and from the end (blue).

7 Conclusion

The SIR instrument was the first high resolution spectrometer on lunar orbit, flown in 2005-2006. The center wavelengths of the 256 pixel detector have been estimated and presented by a third order polynomial as a function of the pixel number; the wavelength ranges of SIR, SIR-2 flight model and SIR-2 flight spare instrument are 938 to 2390 nm, 934 to 2411 nm and 916 to 2385 nm, respectively. The spectral sampling is 5 to 6 nm and decreasing as a function of wavelength. The accuracy of the third order polynomial method could be, according to simulations, as good as 0.5 nm, but residuals of measured data and the polynomial indicate deviations in some cases up to 4 nm for the SIR-2 flight spare and up to 2 nm for the SIR-2 flight model. However, the point spread function due to the optics is as wide as 18 to 30 nm.

The noise level of the digital output signal of SIR-2 is tens of times better (lower) than that of SIR. The best sensitivity of SIR is limited between wavelengths 1.05 and 1.90 μm. The repeatability error in the absolute sensitivity calibration was 3 to 10% in the best sensitivity region of SIR. Due to the characteristic output spectrum of the calibrating devices, the absolute sensitivity calibration has a repeatability error of greater than 20% at pixel numbers higher than 200 (corresponds to 2.1 μm) for all three instruments. The dynamic range of instrument output with the 16-bit A/D converters ranges from 0 to 65535. The bias of SIR is more than 14000 DN which consumes 22% of the full range, whereas for SIR-2 the bias is 2250 DN (3%). The nonlinearity up to signal levels of 55000 DN is 5 to 10% depending on the pixel. It increases toward the maximum DN but the nonlinearity close to the maximum could not be evaluated due to the low light level available from the calibrating devices. Thus, the useful dynamic range of SIR is 14000 to 55000 DN (the exact values are pixel dependent), which is 63% of the total dynamic range. The power incident to the instrument should be at least 1.4 pW to ensure linear operation of the output.

The minerals detected with the SIR and SIR-2 instruments are pyroxenes, olivines, ilmenite and feldspars. Iron bearing orthopyroxenes have their first NIR absorption minimum at 0.90 nm so they are outside the sensitive region of the instrument. The second NIR absorptions of three orthopyroxenes (enstatite-bronzite, Cr-enstatite and hypersthene) are at 1.82, 1.80 and 1.78 μm, respectively; they are at the sensitive region of the instrument but cannot be reliably distinguished from each other because the point spread function is the same size or wider than the differences of these wavelengths. The pyroxene pigeonite has its absorption minima at 0.93 and 2.00 μm, so the second minima can be observed and distinguished from the orthopyroxenes. Subcalcic augite has its minima at 0.99 and 2.18 μm, which can be distinguished both from pigeonite and diopside, whose minima are at 1.02 and 2.30 μm. The clinopyroxenes diopside and augite can also be classified: augite's minima are at 1.05 and 2.35 μm. Olivines can be detected as well: they

have their first minimum between 1.05 (forsterite) and 1.08 μm (fayalite) and a weak second minimum at 1.95 μm. Ilmenite has a band at 1.55 μm and Ca-plagioclase at 1.25 μm, which are well within the high-sensitivity wavelength range but may remain undetectable by SIR because of its moderate signal-to-noise ration and the weakness of these bands.

A software for the data reduction of near-infrared spectrometers has been developed as part of this work. The SIR instrument was a technology demonstration whose electronics produced spikes and jumps in the output signal. The spikes in signal level, which lasted for one or two spectra and were uncorrelated between pixels, were filtered out with a two-stage digital filter. This filtering improved the signal-to-noise ratio by up to 25 dB. However, another effect, the long-lasting jumps in signal levels, which occur in some orbits, are not removed by this filter. Another characteristics of the SIR instrument was a temperature related distortion, whose origin was not known and it affected the signal levels of most pixels in an oscillatory way.

The SIR-2 instrument is based on the same general design as the SIR. The analogue electronics was redesigned and the spikes and jumps in signal level are not present in the data. Two copies of the instrument were built: the first one, which was calibrated in India in October 2007, showed similar signs of temperature related distortion as SIR. Based on data from qualification tests in a thermal vacuum chamber, it was hypothesised that the transmission coefficient of the blocking filter was changing as a function of temperature. For the second copy of SIR-2 this multilayer optical glass filter was replaced by another type of multilayer glass. This instrument was calibrated at the Max Planck Institute for Solar System Research in May 2008 and found to be free of the temperature related distortion. The temperature related oscillations of SIR data may be possible to model using both the SIR and SIR-2 calibration measurements at different temperatures of the instrument; this would eliminate the need to use data from other missions to check the absolute reflectance factor given by SIR, which is generally lower than Clementine's reflectance factor.

For the photometric correction the approach of Akimov and Shkuratov was chosen against the more prevalent Hapke function. The three parameters required of this are not well known in near-infrared and the shadow hiding parameter has been estimated using the SIR data set. The challenge is to obtain a data set which covers a wide range of angles of incidence and emergence. A new value for the shadow hiding parameter as a function of wavelength has been established.

A major advantage of the active temperature controller in the upgraded SIR-2 detector is that when operated at temperatures where the dark background has been measured it is enough to subtract the laboratory dark of the same temperature in DN units from the instrument output, i.e. unlike with SIR no modeled dark count rate needs to be calculated. The SIR dark corrections based on laboratory measurements are not used in the final version of data reduction, instead flight darks looking at the dark lunar surface or space have been utilised to calculate new parameters for the dark reduction. According to dark background calibration of SIR 4% of the pixels were deemed to be defective (5% for SIR-2, 4% for SIR-2 flight spare); failing to show the expected exponential increase in their dark background levels as a function of temperature. During the refinement of dark background calibration using flight data from SIR a further 4% were classified as defective.

A data reduction procedure has been developed for the SIR data set, which covers 18%

of the lunar surface. The data reduction may be further improved by refined modelling of the temperature and electronics related effects in SIR. SIR-2 is expected to observe 20% of the lunar surface in the next two years. This new data could also be used to further improve the original SIR data reduction and inflight calibration. The combined data of SIR and SIR-2 add an important new data set towards the understanding of the lunar mineralogy.

A   Calculation of surface area covered by SIR on the SMART-1 mission

A.1   Introduction

In order to estimate the area covered by the point spectrometer SIR the coordinates and geometrical data given by the SMART-1 mission team have been utilised. The calculation of the area is done in two different ways depending on the separation of neighboring footprints. If they are separated in distance then the area of the footprint ellipse is calculated. If neighboring footprints are overlapping, then a rectangle approximation of an area which is covered by the footprints is calculated. The assumptions of the calculation are:

- The Moon is a sphere with an exact radius of 1737 km. The true large-scale topographic variations on the Moon have an amplitude of 16 km.

- The area illuminated by one footprint is a flat plane surface. Typical footprint areas have a characteristic size of 300 - 3000 m, where the local topography can in reality vary and affect the actual footprint size, especially at large angles of incidence or emergence.

- The footprint has the shape of an ellipse, whose major axis is perpendicular to the direction of motion of the spacecraft. In this work the change of orientation of the spacecraft in the direction of motion during target tracking is not taken into account. This may cause a slight underestimation of the area.

A.2   Calculations

Distance of footprint centers

The coordinates on the lunar surface are known for each spectrum. These coordinates are assumed to be the center of the footprint. The distance on a sphere between two points (θ_1, ϕ_1) and (θ_2, ϕ_2) is

$$s_{1,2} = R_{Moon} \sqrt{2} \sqrt{(1 - \sin(\theta_1) \sin(\theta_2) - \cos(\phi_1 - \phi_2) \cos(\theta_1) \cos(\theta_2))}, \qquad \text{(A.1)}$$

where s is the distance on the ground and R_{Moon} is the radius of the Moon.

The size of an isolated footprint

The size of the footprint is the size of the area of the field of view of the instrument projected on a surface which is tangent to a sphere at the center point of the footprint. It is calculated as

$$A_1 = \pi \frac{a}{2} R \tan \frac{FOV}{2},$$

(A.2)

where a is the major axis of the ellipse, R is the altitude of the spacecraft, and FOV is the field of view angle of the SIR instrument (1.11 mrad). The major axis is

$$a = d \sin \frac{FOV}{2} \left(\frac{1}{\cos \left(e + \frac{FOV}{2} \right)} + \frac{1}{\cos \left(e - \frac{FOV}{2} \right)} \right),$$

(A.3)

where d is the distance between the spacecraft and the footprint center and e is the angle of emergence, that is the angle between the surface normal observed and the spacecraft. All these values are available in the geometry files calculated by the mission team.

The area of overlapping footprints

The criteria that neighboring footprints are overlapping is based on the distance between their centers compared to the length of the major axis. If $s_{i,i+1} < a_i$ (refer to Eq. (1)) for footprints i and j, then the area is calculated as a rectangle:

$$A_i = s_{i,i+1} \left(a_i \frac{\sqrt{\pi}}{2} \right).$$

(A.4)

The factor $a_i \frac{\sqrt{\pi}}{2}$ is the length of a side of a square, whose area is the same as a circle with diameter a_i would have. When there is a sequence of overlapping footprints the total area of them is ΣA_i. In this way the overlapping elliptical footprints have been replaced by a series of rectangles, which have approximately the same total area as the area covered by the overlapping footprints.

A.3   Results

The end result of the area calculation depends on the constraints set to the observations. As a first example, if the maximum major axis length of a footprint is limited to 3 km, and the angle of incidence is limited to 90°, then the total area from the above calculation is 18% of lunar surface. Independently of the area calculation the maximum east-west separation between orbits has been determined to be 60 km in the SIR observations.

B   Spectral calibration measurements of SIR-2

Table B.1: Measurements for spectral calibration of SIR-2 on 4.-5. October, 2007 at Space Applications Center of ISRO, India.

Meas. no.	Start wavelength [nm]	End wavelength [nm]	Interval [nm]	Detector temperature [C]	Core optics temperature [C]
66	900	1200	50	-60	
67	900	1200	50	-60	
68	900	1200	50	-60	
69	Dark background			-60	
70	900	1200	10	-60	
71	900	1200	6	-60	
72	800	1700	6	-60	-40
73	800	1250	6	-60	-40
74	1250	1700	6	-60	-40
75	1700	2100	6	-60	-40
76	800	2100	6	-60	
77	1100	1400	0.5	-60	-40
78	1500	1800	6	-60	-40
79	1800	2100	6	-60	-40
80	1500	2100	6	-60	-40
81	Dark background			-60	
82	900	2100	6	-50	
83	900	1700	6	-50	
84	900	1250	6	-50	
85	1250	1700	6	-50	
86	1700	2100	6	-50	
87	900	2100	6	-50	
88	1100	1400	0.5	-50	
89	930	970	0.5	-50	
90	1480	1520	0.5	-50	
91	1220	1250	0.5	-50	
92	1310	1340	0.5	-50	
93	Dark background			-50	

Meas. no.	Start wavelength [nm]	End wavelength [nm]	Interval [nm]	Detector temperature [C]	Core optics temperature [C]
94	1500	1540	0.5	-50	
95	1680	1720	0.5	-50	
96	1860	1900	0.5	-50	
97	900	1000	6	-50	
98	1100	2100	6	-50	
99	900	2100	6	-50	
100	2100	2500	6	-50	
101	2100	2500	6	-50	
102	2000	2500	6	-50	
103	2000	2500	6	-50	
104	2000	2500	0.5	-50	
105	2000	2500	6	-50	
106	2000	2300	0.5	-50	
107	1980	2020	0.5	-50	
108	1980	2020	0.5	-50	
109	2080	2120	0.5	-50	
110	2180	2220	0.5	-50	
111	2280	2320	0.5	-50	
112	Dark background			-60	
113	2000	2500	6	-60	-40
114	2000	2300	0.5	-60	
115	2080	2120	0.5	-60	
116	2180	2220	0.5	-60	
117	2280	2320	0.5	-60	
118	2280	2320	6	-60	
119	2000	2300	0.5	-60	
120	2000	2500	6	-60	
121	2000	2500	50	-50	

C   Radiometric calibration measurements of SIR-2

This appendix lists the detailed measurements of the radiometric and dark background calibration of the SIR-2 instrument carried out in Ahmedabad, India on 2.-3.10.2007. Each measurement has a number which indicates the order of the recordings in time. Some numbers are missing due to an invalid file or other technical problem. For each integration time, between 100 and 1000 spectra were recorded. The thermistor of the detector is located inside its housing and the thermistor of the quartz body is glued to the glass of the core optics. The "purpose" column of Table C.1 indicates the primary objective of the measurement: i) absolute sensitivity to determine the spectral response of the instrument, ii) linearities with respect to either changing light intensity or to different integration times, or iii) determination of the dark background signal. These three main types have alterations depending on the exact goal. The readout frequency was by default 1.54 MHz; the possible effect of another readout frequency has been tested, these case are indicated in the "Comments" column.

Table C.1: List of measurements in the order of recordings. (*) indicates that temperature was varying during the measurement.

Meas. no.	Purpose	Comments	Detector temp. [°C]	Core optics temp. [°C]	Integration times [ms]
1	Health check	Instrument inside chamber, ambient temperature and pressure	29	24	5
4	Quartz body temperature dependence	1 fixed position lamp on	-30	-9 (*)	151, 10, 151
6	Changing light intensity	Lamps switched off during recording	-30	-17	252
7	Dark background	Closed chamber	-30	-18	252
8	Dark background	Closed chamber	-30	-19	252, 120, 151, 200
9	Integrating sphere dark background	Lamps off	-30	-19	120, 151, 200, 252
10	Integrating sphere dark background	Lamps off, readout frequency 1 MHz	-30	-19	120, 151, 200, 252
11	Linearity w. r. t. light intensity	1 lamp at maximum setting 8/8	-40	-20	1, 151, 252
12	Linearity w. r. t. light intensity	1 lamp at setting 7/8	-40	-21	1, 151, 252
13	Linearity w. r. t. light intensity	1 lamp at setting 6/8	-40	-21	252
14	Linearity w. r. t. light intensity	1 lamp at setting 5/8	-40	-21	252
15	Linearity w. r. t. light intensity	1 lamp at setting 4/8	-40	-21	252
16	Linearity w. r. t. light intensity	1 lamp at setting 3/8	-40	-21	252
17	Linearity w. r. t. light intensity	1 lamp at setting 2/8	-40	-21	252
18	Linearity w. r. t. light intensity	1 lamp at setting 1/8	-40	-21	252
19	Integrating sphere dark background	Lamps off	-40	-21	252
20	Dark background	Closed chamber	-40	-21	252
21	Absolute sensitivity	1 lamp at maximum	-40	-21	252
22	Integrating sphere dark background	Lamps off	-50	-25	120, 151, 200, 252
23	Absolute sensitivity	1 lamp at maximum	-50	-26	120, 151, 200, 252
24	Integrating sphere dark, warm sphere	Lamps off	-50	-26	120, 151, 200, 252

Meas. no.	Purpose	Comments	Detector temp. [° C]	Core optics temp. [° C]	Integration times [ms]
25	Dark background	Closed chamber	-50	-27	120, 151, 200, 252
27	Dark background	Closed chamber, no temperature stabilization	-60 -> -25	-36 (*)	0.5 - 300
28	Dark background	Closed chamber, oversampling	-50	-29	252, 100, 151
29	Dark background	Closed chamber	-50	-30	0.5 - 300
30	Absolute sensitivity	1 lamp at maximum, oversampling	-50 (*)	-32	100, 151, 252
31	Linearity w.r.t. integration time	1 lamp at maximum	-50	-32	0.5 - 300
32	Linearity w.r.t. integration time	1 lamp at maximum, readout frequency 1 MHz	-50	-32	0.5 - 300
33	Absolute sensitivity	1 lamp at maximum	-50	-33	120, 151, 200, 252
34	Dark background	Closed chamber	-50	-34	120, 151, 200, 252
36	Integrating sphere dark background	Lamps off	-50	-34	120, 151, 200, 252
37	Linearity w. r. t. integration time	1 lamp at maximum	-60	-34	0.5 - 300
38	Linearity w. r. t. integration time	1 lamp at maximum, readout frequency 1 MHz	-60	-34	0.5 - 300
39	Absolute sensitivity	1 lamp at maximum, oversampling	-60	-35	100, 151, 252
40	Absolute sensitivity	1 lamp at maximum	-60	-35	120, 151, 200, 252
42	Integrating sphere dark background	Lamps off	-60	-36	120, 151, 200, 252
44	Linearity w. r. t. light intensity	1 lamp at setting 1/8	-60	-37	1, 151, 252
45	Linearity w. r. t. light intensity	1 lamp at setting 2/8	-60	-37	1, 151, 252
46	Linearity w. r. t. light intensity	1 lamp at setting 3/8	-60	-37	1, 151, 252
47	Linearity w. r. t. light intensity	1 lamp at setting 4/8	-60	-37	1, 151, 252
48	Linearity w. r. t. light intensity	1 lamp at setting 5/8	-60	-38	1, 151, 252
49	Linearity w. r. t. light intensity	1 lamp at setting 6/8	-60	-38	1, 151, 252
50	Linearity w. r. t. light intensity	1 lamp at setting 7/8	-60	-38	1, 151, 252
51	Linearity w. r. t. light intensity	1 lamp at maximum setting 8/8	-60	-38	1, 151, 252
52	Absolute sensitivity	1 lamp at maximum	-60	-38	120, 151, 200, 252

Meas. no.	Purpose	Comments	Detector temp. [°C]	Core optics temp. [°C]	Integration times [ms]
53	Integrating sphere dark background	Lamps off	-60	-38	120, 151, 200, 252
54	Dark background	Closed chamber	-60	-38	120, 151, 200, 252
55	Quartz body temperature dependence	1 lamp at maximum	-60	-39	120, 151, 200, 252
56	Quartz body temperature dependence	A and B lamps on, not calibrated	-60	-39	120
57	Quartz body temperature dependence	A and B lamps on, not calibrated	-60	-39	120, 151, 200, 252
59	Low light level	Only lamp B on, not calibrated	-60	-39	120, 151, 200, 252
60	Dark background	Integrating sphere on for a long time, O-Box heating effect	-60	-39	120, 151, 200, 252
61	Changing light intensity	Lamps switched off during recording	-60	-39	120, 151, 200, 252

D Parameters for dark background correction of SMART-1 / SIR data

Table D.1: Parameters for the function $I = d + aT^b \exp\frac{c}{T}$, where I is the background level in DN and T is the detector temperature in Kelvin. These parameters have been estimated by fitting this function to data measured by SIR on the non-illuminated farside of the Moon with integration time 151 ms.

Pixel	a	b	c	d	Pixel	a	b	c	d
1	1088	2.51	-3769	93.0	129	1141	1.49	-2888	93.3
2	1108	1.98	-3441	93.0	130	1101	2.48	-3892	93.8
3	1090	2.43	-3619	90.3	131	1150	1.86	-3195	93.5
4	1132	1.75	-2836	87.1	132	1089	2.70	-4029	94.0
5	1077	2.50	-3808	92.6	133	927	1.99	-3350	95.3
6	1000	-3.24	-4000	93.6	134	1097	1.80	-3080	93.5
7	1082	2.59	-3931	94.8	135	1106	1.88	-3187	92.8
8	1097	2.56	-3873	91.7	136	1071	2.72	-4039	95.9
9	1122	1.89	-3018	88.3	137	1160	0.90	-2178	92.6
10	1085	2.25	-3655	92.7	138	1115	2.24	-3664	93.6
11	1074	2.48	-3875	92.8	139	1112	1.92	-3324	99.6
12	1066	2.37	-3692	92.2	140	1105	2.38	-3896	94.4
13	1113	0.39	-837	154.8	141	1068	2.38	-3800	94.1
14	1087	2.59	-4100	92.7	142	1115	1.93	-3283	94.0
15	1136	1.27	-2517	96.1	143	1078	2.45	-3885	94.4
16	1082	2.43	-3863	95.6	144	1116	1.91	-3200	93.8
17	1109	2.21	-3654	92.8	145	1147	1.14	-2126	100.2
18	1025	1.35	-2432	105.9	146	930	1.96	-3081	97.3
19	1077	2.57	-3991	93.4	147	1145	1.64	-3019	93.8
20	1057	2.37	-3824	93.3	148	1097	2.03	-3353	93.4
21	1102	2.28	-3729	93.2	149	1127	1.71	-2868	90.5
22	1078	2.39	-3844	93.0	150	1102	2.02	-3340	93.3
23	1103	2.13	-3579	93.0	151	1096	2.67	-4233	94.6
24	1091	2.03	-3376	93.5	152	1093	2.36	-3752	94.0
25	1092	2.24	-3736	93.0	153	1075	2.34	-3793	94.3
26	1074	2.32	-3744	93.0	154	1106	2.10	-3417	93.6

Pixel	a	b	c	d	Pixel	a	b	c	d
27	1114	1.81	-3290	93.8	155	1174	1.31	-2805	93.7
28	1082	2.52	-4005	93.4	156	1109	2.25	-3716	94.0
29	1136	2.00	-3236	90.1	157	1112	2.32	-3803	94.0
30	1101	2.20	-3729	93.5	158	1133	1.96	-3316	93.3
31	1083	2.48	-3987	93.5	159	1055	2.79	-4150	95.5
32	1127	1.65	-3077	92.3	160	1117	0.28	-1157	79.6
33	1080	2.50	-3980	93.4	161	1094	2.21	-3594	94.8
34	1154	1.63	-3009	93.0	162	1092	2.12	-3505	95.5
35	1076	2.41	-3842	92.9	163	1106	2.27	-3650	95.7
36	1133	1.42	-2836	92.5	164	1042	2.70	-4035	94.7
37	1119	2.03	-3466	92.7	165	1025	1.41	-2271	82.7
38	1097	2.29	-3560	92.8	166	1124	1.88	-3102	92.0
39	1059	2.58	-4003	93.7	167	1111	1.68	-3104	93.7
40	1124	-0.48	-573	89.0	168	1073	2.61	-4005	94.5
41	1112	2.52	-3785	94.5	169	1089	1.86	-2822	97.2
42	1090	2.13	-3601	93.4	170	1000	-9.25	-4000	94.5
43	1097	2.21	-3551	104.4	171	1091	2.27	-3754	94.2
44	995	1.61	-2616	92.3	172	1079	2.61	-4075	94.7
45	1071	2.50	-4030	93.6	173	1134	1.29	-2586	92.7
46	1154	0.51	-1743	90.7	174	1095	2.47	-3800	94.5
47	1093	2.21	-3725	93.0	175	1085	2.34	-3669	93.9
48	1130	1.43	-2818	92.8	176	1111	2.03	-3436	94.1
49	1066	2.70	-4072	93.8	177	1036	0.96	-1654	70.3
50	1079	2.05	-3438	93.1	178	1043	2.59	-3990	94.8
51	1117	2.24	-3571	93.0	179	1095	2.36	-3811	94.6
52	1117	2.07	-3502	93.6	180	1100	2.11	-3387	93.4
53	1044	2.56	-3950	95.1	181	1090	2.07	-3365	94.1
54	1112	2.21	-3628	93.3	182	1112	-0.11	-902	88.4
55	1086	2.28	-3608	94.3	183	1078	2.61	-4034	94.3
56	1070	2.14	-3616	93.8	184	1151	1.11	-2385	92.9
57	1104	2.41	-3756	93.3	185	1095	2.39	-3772	94.0
58	1040	0.58	-1778	91.2	186	1106	2.08	-3464	94.7
59	1092	2.52	-4045	93.5	187	926	1.90	-3109	100.9
60	1097	1.94	-3447	93.6	188	1097	2.05	-3399	94.6
61	1098	2.20	-3492	93.6	189	1054	2.48	-3773	95.2
62	1088	2.21	-3645	93.5	190	981	2.40	-3740	96.3
63	1068	2.49	-3969	93.8	191	1092	2.68	-4086	96.6
64	1090	2.13	-3296	92.7	192	1118	-0.31	-725	89.4
65	1173	1.74	-2842	98.9	193	1114	2.06	-3290	94.8
66	1100	2.22	-3618	93.4	194	1080	2.38	-3864	95.1
67	1100	1.46	-2687	94.3	195	1075	2.62	-3988	95.3
68	1110	2.07	-3485	93.3	196	1092	1.73	-3105	94.8
69	1063	2.56	-4037	95.6	197	1070	2.52	-3879	95.0
70	1079	2.42	-3826	94.3	198	1074	2.22	-3552	94.9
71	1065	2.59	-3988	94.0	199	1109	2.13	-3603	94.7

Pixel	a	b	c	d	Pixel	a	b	c	d
72	1129	1.83	-3161	93.2	200	1077	2.27	-3712	94.9
73	1050	2.77	-4138	94.0	201	1077	2.11	-3573	94.5
74	1085	1.90	-3332	94.7	202	1118	1.97	-3265	93.7
75	1140	1.31	-2669	92.7	203	1088	2.35	-3744	94.1
76	1102	2.51	-3898	93.5	204	1111	0.36	-857	80.0
77	1096	2.35	-3624	93.2	205	1077	2.55	-3870	93.9
78	1074	2.51	-3913	94.1	206	1133	1.74	-3090	94.6
79	1096	2.27	-3688	93.7	207	1100	2.17	-3516	94.1
80	1084	2.58	-4008	93.3	208	1088	2.39	-3816	95.1
81	1107	2.03	-3261	92.1	209	1122	1.68	-3113	94.4
82	1117	1.62	-2943	103.1	210	1113	2.37	-3637	93.4
83	1072	2.58	-4038	94.2	211	995	1.87	-2826	93.2
84	1081	2.09	-3283	98.9	212	1001	-3.62	-3985	434.0
85	1082	2.52	-3964	94.6	213	1069	1.59	-2917	93.0
86	1164	1.16	-2505	92.5	214	996	2.51	-3770	94.9
87	1093	2.38	-3735	93.4	215	1072	2.42	-3927	95.2
88	1085	2.27	-3706	94.1	216	1093	2.33	-3631	94.6
89	1106	2.15	-3532	94.9	217	1085	2.07	-3284	94.2
90	1101	1.97	-3420	93.5	218	1083	2.48	-3858	94.8
91	1075	2.59	-4070	93.8	219	1135	1.95	-3233	95.0
92	1074	2.40	-3838	94.2	220	1062	2.27	-3829	95.2
93	1091	2.24	-3628	93.6	221	1114	2.22	-3462	94.2
94	1109	2.04	-3312	93.5	222	1121	1.35	-2643	93.4
95	1094	2.25	-3698	94.0	223	837	2.48	-3896	109.0
96	1102	2.16	-3474	92.8	224	1099	2.00	-3392	95.0
97	1100	2.19	-3651	93.6	225	1113	1.91	-3205	93.9
98	953	1.61	-2577	133.9	226	1094	2.54	-3792	93.7
99	1110	1.74	-3146	93.6	227	1103	2.25	-3686	95.0
100	1108	2.29	-3665	93.9	228	1068	2.63	-4010	95.5
101	1061	2.36	-3779	94.1	229	1126	-0.55	-523	91.7
102	1122	-0.04	-540	50.3	230	1081	2.39	-3703	95.3
103	1169	1.31	-2746	93.0	231	1056	2.51	-3896	95.9
104	1103	2.22	-3725	93.9	232	1098	2.37	-3787	95.0
105	1084	2.46	-3962	94.0	233	1122	1.86	-2905	87.5
106	1098	2.41	-3805	96.4	234	1086	2.22	-3706	96.3
107	1108	1.61	-2644	88.8	235	952	2.51	-3803	95.1
108	1034	0.62	-1565	85.4	236	1120	1.54	-2582	91.9
109	1073	2.63	-3998	94.3	237	1110	2.06	-3397	95.2
110	1074	2.29	-3674	93.6	238	1111	0.29	-882	38.7
111	1094	2.24	-3691	93.8	239	1096	2.44	-3834	95.7
112	1108	2.09	-3434	95.2	240	1073	2.27	-3598	96.1
113	1095	2.26	-3733	93.7	241	1114	2.27	-3604	94.0
114	1175	1.45	-2921	93.7	242	1147	0.76	-1978	93.6
115	959	2.58	-3823	94.0	243	925	2.42	-3616	106.8
116	1067	2.43	-3835	93.7	244	1107	2.13	-3467	95.6

Pixel	a	b	c	d	Pixel	a	b	c	d
117	8	17.23	-21490	122.8	245	1099	1.97	-3279	94.3
118	1116	1.71	-3114	93.4	246	1099	2.16	-3534	94.9
119	1005	1.23	-2309	98.9	247	1069	1.90	-3143	95.5
120	1075	2.73	-4156	94.0	248	1078	2.47	-3821	95.6
121	1145	1.33	-2666	92.9	249	1109	2.16	-3457	94.4
122	1077	2.66	-4083	94.1	250	1104	1.56	-2954	94.8
123	1123	2.21	-3681	94.3	251	1134	1.86	-3239	94.6
124	1141	0.82	-1602	135.2	252	1050	2.33	-3612	95.8
125	1119	2.31	-3832	93.8	253	1129	-0.66	-456	92.8
126	1109	0.30	-918	100.3	254	1128	1.22	-2191	101.5
127	1053	2.39	-3727	94.6	255	1072	2.70	-4093	95.2
128	1072	2.46	-3861	94.3	256	1123	1.84	-3197	94.6

Table D.2: Parameters for the function $I = d + aT^b \exp \frac{c}{T}$, where I is the background level in DN and T is the detector temperature in Kelvin. These parameters have been estimated by fitting this function to data measured by SIR on the non-illuminated farside of the Moon with integration time 252 ms.

Pixel	a	b	c	d	Pixel	a	b	c	d
1	675	2.61	-3868	59.9	129	839	1.76	-3250	57.3
2	861	1.84	-3290	56.6	130	715	2.60	-4028	58.3
3	720	2.50	-3689	58.5	131	826	1.83	-3184	57.9
4	828	1.76	-2862	56.0	132	665	2.79	-4118	59.6
5	673	2.50	-3788	58.4	133	798	2.00	-3407	58.6
6	1000	-3.72	-4000	56.5	134	746	2.00	-3333	58.8
7	653	2.69	-4019	60.5	135	845	1.79	-3097	57.2
8	649	2.67	-3971	58.2	136	625	2.87	-4181	61.4
9	732	2.00	-3146	57.2	137	956	1.40	-2858	57.4
10	776	2.18	-3586	57.0	138	773	2.11	-3508	57.3
11	703	2.57	-3979	57.8	139	735	2.04	-3471	63.2
12	716	2.41	-3722	57.5	140	779	2.29	-3789	57.6
13	1137	-0.21	-262	149.5	141	720	2.47	-3917	58.2
14	709	2.64	-4156	56.9	142	782	1.99	-3370	58.1
15	809	1.45	-2761	61.0	143	729	2.51	-3973	58.3
16	702	2.46	-3898	60.0	144	795	1.87	-3166	58.2
17	775	2.25	-3723	57.2	145	856	1.07	-2042	64.6
18	1161	5.76	-8460	80.8	146	712	2.14	-3307	63.1
19	694	2.61	-4017	57.9	147	1405	1.64	-3175	57.7
20	722	2.42	-3884	57.4	148	827	1.88	-3175	57.3
21	761	2.30	-3759	57.4	149	1486	3.13	-5017	62.6
22	709	2.47	-3939	57.3	150	780	1.99	-3307	57.9
23	802	2.04	-3479	56.9	151	732	2.65	-4196	57.8
24	771	2.03	-3383	58.0	152	711	2.46	-3861	58.3

Pixel	a	b	c	d	Pixel	a	b	c	d
25	731	2.37	-3890	57.1	153	723	2.42	-3885	58.1
26	758	2.34	-3780	57.3	154	750	2.12	-3439	58.1
27	700	1.83	-3274	57.1	155	852	2.06	-3771	57.3
28	677	2.63	-4126	57.6	156	787	2.24	-3730	57.7
29	818	1.81	-3017	55.7	157	721	2.47	-3986	57.9
30	789	2.36	-3945	57.4	158	823	1.94	-3299	57.6
31	744	2.41	-3902	57.1	159	631	2.89	-4231	60.3
32	812	1.98	-3525	56.8	160	1253	0.17	-1156	49.3
33	692	2.57	-4052	57.4	161	772	2.16	-3545	58.8
34	803	1.90	-3369	57.7	162	777	2.12	-3515	59.1
35	738	2.49	-3944	57.5	163	742	2.30	-3693	59.9
36	944	1.81	-3393	56.8	164	677	2.83	-4175	60.0
37	782	2.14	-3604	56.9	165	854	1.44	-2347	55.4
38	703	2.39	-3671	58.9	166	787	1.80	-3016	57.3
39	691	2.70	-4145	58.4	167	1134	1.83	-3390	57.5
40	1307	0.01	-1445	55.8	168	704	2.75	-4158	59.1
41	662	2.56	-3781	59.7	169	768	1.89	-2857	67.8
42	856	2.02	-3479	56.9	170	1000	-11.16	-4000	57.0
43	704	2.46	-3850	69.5	171	831	2.18	-3678	57.7
44	755	1.55	-2549	59.4	172	698	2.66	-4119	58.5
45	771	2.45	-3970	57.2	173	1182	1.39	-2828	57.2
46	853	1.41	-2959	56.5	174	676	2.54	-3859	59.4
47	834	2.24	-3805	56.9	175	725	2.41	-3761	58.9
48	825	1.86	-3389	57.1	176	811	1.96	-3364	57.6
49	638	2.86	-4238	59.2	177	879	1.13	-1926	57.5
50	761	2.17	-3599	57.6	178	654	2.75	-4163	59.2
51	740	2.31	-3655	58.2	179	768	2.40	-3872	58.3
52	813	2.04	-3478	57.3	180	722	2.14	-3409	58.4
53	664	2.58	-3944	59.0	181	732	2.17	-3488	59.0
54	753	2.27	-3691	57.6	182	1170	0.90	-2419	57.5
55	711	2.46	-3821	59.7	183	723	2.63	-4047	58.4
56	787	2.14	-3631	57.3	184	825	1.27	-2619	57.2
57	709	2.41	-3737	58.2	185	755	2.35	-3734	58.3
58	779	1.21	-2614	56.7	186	793	1.99	-3362	58.3
59	722	2.56	-4104	57.4	187	857	2.82	-4399	67.3
60	781	2.35	-3972	57.5	188	775	2.04	-3393	58.4
61	709	2.39	-3703	59.2	189	683	2.60	-3915	60.5
62	748	2.24	-3671	57.4	190	685	2.55	-3917	60.5
63	730	2.57	-4074	57.8	191	689	2.82	-4250	61.1
64	681	2.34	-3526	61.1	192	779	1.65	-3387	57.8
65	734	1.72	-2801	66.0	193	854	2.00	-3237	59.6
66	795	2.14	-3540	57.4	194	753	2.38	-3870	58.5
67	820	1.41	-2641	58.7	195	658	2.74	-4104	60.1
68	791	2.01	-3426	57.3	196	825	1.84	-3262	58.3
69	704	2.62	-4110	59.6	197	685	2.65	-4019	59.7

Pixel	a	b	c	d	Pixel	a	b	c	d
70	687	2.49	-3890	58.6	198	728	2.40	-3783	59.9
71	681	2.74	-4163	58.8	199	813	2.21	-3729	58.1
72	903	1.76	-3110	57.4	200	742	2.23	-3664	58.2
73	638	2.91	-4269	59.4	201	778	2.27	-3796	58.0
74	810	2.01	-3502	58.7	202	792	1.92	-3215	58.0
75	893	1.41	-2837	56.8	203	790	2.22	-3596	57.9
76	693	2.65	-4058	58.5	204	1046	0.50	-1119	81.0
77	683	2.48	-3763	59.3	205	663	2.66	-3980	59.3
78	691	2.55	-3942	58.4	206	908	1.73	-3110	58.3
79	712	2.37	-3803	58.0	207	808	2.11	-3464	58.3
80	718	2.62	-4045	57.9	208	736	2.36	-3774	58.6
81	736	2.11	-3351	58.2	209	1248	1.76	-3338	57.7
82	752	1.52	-2777	65.4	210	683	2.49	-3758	59.5
83	736	2.52	-3960	57.9	211	773	1.85	-2817	62.6
84	686	2.28	-3484	65.5	212	1000	-3.13	-3993	260.1
85	717	2.48	-3903	58.2	213	1208	1.50	-2929	56.9
86	836	1.67	-3166	57.2	214	675	2.65	-3938	60.6
87	718	2.43	-3776	58.3	215	724	2.50	-4022	58.4
88	768	2.17	-3580	57.7	216	700	2.40	-3708	59.8
89	743	2.09	-3454	58.8	217	689	2.20	-3416	59.9
90	781	2.11	-3599	57.4	218	715	2.50	-3874	59.0
91	698	2.76	-4264	58.0	219	763	1.94	-3211	59.4
92	687	2.51	-3966	58.3	220	735	2.32	-3891	58.1
93	730	2.36	-3777	58.1	221	682	2.33	-3575	60.0
94	723	2.06	-3323	58.6	222	1278	0.98	-2283	56.1
95	751	2.24	-3691	57.7	223	616	2.24	-3527	67.8
96	739	2.19	-3507	57.8	224	855	1.98	-3396	58.2
97	841	2.18	-3674	57.5	225	871	1.72	-3008	57.7
98	720	1.65	-2609	96.3	226	689	2.59	-3830	59.7
99	807	1.81	-3248	57.6	227	795	2.21	-3646	58.4
100	757	2.25	-3608	58.1	228	678	2.69	-4065	59.7
101	733	2.43	-3863	58.3	229	1114	-0.43	-640	53.2
102	1132	0.06	-390	-166.0	230	707	2.42	-3733	59.8
103	1309	1.92	-3648	57.0	231	672	2.59	-3979	59.8
104	750	2.23	-3747	57.4	232	734	2.39	-3807	58.7
105	715	2.50	-4013	57.7	233	772	1.92	-2995	57.7
106	721	2.50	-3909	60.9	234	800	2.16	-3652	58.9
107	735	1.84	-2919	58.8	235	650	2.58	-3890	60.1
108	1279	0.67	-1765	54.6	236	795	1.63	-2719	60.7
109	672	2.74	-4113	59.2	237	803	1.93	-3250	58.8
110	775	2.23	-3612	57.7	238	977	0.50	-1261	44.7
111	775	2.24	-3702	57.5	239	730	2.42	-3800	59.2
112	752	2.06	-3390	59.2	240	721	2.31	-3632	59.9
113	779	2.30	-3799	57.7	241	774	2.22	-3545	58.3
114	1269	1.67	-3322	57.1	242	1305	0.80	-2157	57.5

Pixel	a	b	c	d	Pixel	a	b	c	d
115	639	2.66	-3918	60.2	243	685	2.17	-3286	67.3
116	710	2.50	-3908	58.1	244	752	2.03	-3335	58.8
117	1080	8.76	-12369	73.3	245	890	1.67	-2947	57.6
118	891	2.01	-3534	57.5	246	796	2.17	-3562	58.8
119	858	1.15	-2257	63.9	247	739	2.02	-3296	60.2
120	667	2.87	-4304	58.9	248	694	2.53	-3883	59.7
121	1191	1.50	-2986	57.3	249	735	2.18	-3480	59.0
122	655	2.75	-4164	58.6	250	1131	1.61	-3113	58.0
123	1317	2.01	-3563	57.6	251	1304	1.65	-3100	57.8
124	899	0.59	-1364	99.5	252	691	2.38	-3659	60.4
125	1174	2.24	-3845	57.3	253	1377	1.11	-2933	57.9
126	990	0.43	-1175	84.9	254	763	1.41	-2420	70.1
127	737	2.42	-3771	59.2	255	645	2.78	-4155	59.6
128	693	2.60	-4016	58.8	256	868	1.48	-2789	57.2

E   List of sites observed during SMART-1 mission useful for photometric function studies

The conditions of the illumination geometry have a wavelength dependent effect on the brightness of an observed spectrum. In the approach of Shkuratov and Akimov the phase function for this photometric correction (Section 5.4) has three parameters: shadow hiding, effective radius of particles, and light diffusion length. These parameters can be determined from observations at various phase angles once Akimov's disk function has been applied. The SMART-1 mission observed certain locations on the Moon with a special operational mode called target tracking, where the whole spacecraft was pointing to the same location on the Moon for recording several spectra with changing geometry. These and other useful observations are listed in Table E.1.

Table E.1: List of sites used to find the shadow hiding parameter of the semi-empirical Shkuratov phase function. The number of orbits column indicates the number of orbits from which the site has been observed.

Site name	Latitude [°]	Longitude [°]	Orbits
Apollo 11	0.63	23.52	364, 365, 2212
Apollo 12	-3.07	-23.38	381, 382
Apollo 14	-3.71	-17.43	378, 379, 380
Apollo 15	26.12	3.68	369, 371, 372
Apollo 16	-8.84	15.24	366, 367
Apollo 17	20.19	30.82	361, 362
Mare Serenitatis 2	18.67	21.46	363, 364, 365, 366, 2214
Humboldt	-27.52	80.92	1730, 1731
southeast of Lindsay, site 1	-9.26	15.39	1623
southeast of Lindsay, site 2	-9.16	15.50	1623
southeast of Lindsay, site 3	-9.10	15.34	1617, 1623
Piccolomini	-29.86	32.12	1617
south of Tacitus	-17.99	19.68	1617, 2214
southeast of Rarnan	27.09	-52.85	2241
Sinus Medii	3.96	-1.43	1623, 2222

Bibliography

Abe, M., Y. Takagi, K. Kitazato, S. Abe, T. Hiroi, F. Vilas, B. E. Clark, P. A. Abell, S. M. Lederer, K. S. Jarvis, T. Nimura, Y. Ueda, A. Fujiwara, 2006, Near-Infrared Spectral Results of Asteroid Itokawa from the Hayabusa Spacecraft, Science Vol. 312, pp. 1334–1338

Alvarez, L. W., P. H. Eberhard, R. R. Ross, R. D. Watt, 1970, Search for Magnetic Monopoles in the Lunar Sample, Science Vol. 167, pp. 701-703

Andersen, C. A., J. R. Hinthorne, 1971, $^{207}Pb/^{206}Pb$ ages of individual mineral phases in Luna 20 material by ion microprobe mass analysis, Geochimica et Cosmochimica Acta, Vol. 37, pp. 745-754

The Apollo 17 Preliminary Examination Team, 1973, Apollo 17 Lunar Samples: Chemical and Petrographic Description, Science Vol. 182, No. 4113

ASTM E 490 Standard Solar Constant and Zero Air Mass Solar Spectral Irradiance Tables, 2000, The American Society for Testing and Materials

Basilevsky, A. T., H. U. Keller, A. Nathues, U. Mall, H. Hiesinger, M. Rosiek, 2004, Scientific objectives and selection of targets for the SMART-1 Infrared Spectrometer (SIR), Planetary and Space Science, Vol. 52, Issue 14, pages 1261-1285

Benkert, J.-P., H. Baur, P. Signer, R. Wieler, 1993, He, Ne, and Ar From the Solar Wind and Solar Energetic Particles in Lunar Ilmenites and Pyroxenes, Journal of Geophysical Research, Vol. 98, No. E7, pp. 13147-13162

Binder, A. B., 1998, Lunar Prospector: Overview, Science, Vol. 281

Byrne, C, J, 2007, A Large Basin on the Near Side of the Moon, Earth, Moon and Planets, Vol. 101, pp. 153–188, DOI 10.1007/s11038-007-9225-8

Cahill, J. T., P. G. Lucey, J. J. Gillis, D. Steutel, 2004, Verification of quality and compatibility for the newly calibrated NIR data set, 35th Lunar and Planetary Science Conference, abstract 1469

Canup, R. M., E. Asphaug, 2001, Origin of the Moon in a giant impact near the end of the Earth's formation, Nature, Vol. 412, pp. 708–7112

Carlson, R. W., P. R. Weissman, W. D. Smythe, J. C. Mahoney, 1992, Near-infrared Mapping Spectrometer Experiment on Galileo, Space Science Reviews, 60, pp. 457–502

Carlson, R. W., H. H. Kieffer, K. H. Baines, K. J. Becker, G. E. Danielson, K. Edwards, F. P. Fanale, J. Forsythe, L. R. Gaddis, J. C. Granahan, J. Hui, T. V. Johnson, R. Lopes-Gautier, L. W. Kamp, D. L. Matson, T. B. McCord, R. Mehlman, A. C. Ocampo, L. A. Soderblom, W. D. Smythe, J. Torson, P. R. Weissman, 1993, Preliminary report of lunar observations by the near-infrared mapping spectrometer (NIMS) during the second Galileo Earth-Moon encounter, 24th Lunar and planetary Science Conference, Part 1: A-F, pp. 255–256

Clark, R. N., 1999, Chapter 1: Spectroscopy of Rocks and Minerals, and Principles of Spectroscopy, in Manual of Remote Sensing, Vol. 3: Remote Sensing for Earth sciences, ed. A. N. Rencz, John Wiley and Sons, New York, pp. 3–58

Combe, J.-Ph., S. Le Mouélic, G. Y. Kramer, T. B. McCord, 2008, Mapping of the mineralogy of the Moon with Clementine UVVIS and NIR data analyzed by a multiple-endmember linear spectral unmixing model (MELSUM), 39th Lunar and Planetary Science Conference, abstract 2247

Das, P., 2007, Thermal analysis report on SIR-2 instrument SIR-2 project document No. MPS/SIR-2/Thermal/Das-01

Draper, N. R., Smith, H., 1981, Applied Regression Analysis, 2nd ed., John Wiley & Sons, ISBN 0-471-02995-5

Durbin, J., Watson, G. S., 1951, Testing for serial correlation in least square regression II, Biometrika, 38, 159–178

Edwards, K. E., T. R. Calvin, T. L. Becker, D. Cook, M. E. Davies, T. E. Duxburg, E. M. Eliason, E. M. Lee, A. S. McEwen, H. Morgan, M. S. Robinson, T. Sorensen, 1996, 27th Lunar and Planetary Science Conference, Vol. 27, p. 335

Foing, B. H., G. D. Racca, A. Marini, E. Evrard, L. Stagnaro, M. Almeida, D. Koschny, D. Frew, J. Zender, J. Heather, M. Grande, J. Huovelin, H. U. Keller, A. Nathues, J. L. Josset, A. Malkki, W. Schmidt, G. Noci, R. Birki, L. Iess, Z. Sodnik, P. McManamon, 2006, SMART-1 mission to the Moon: Status, first results and goals, Advances in Space Research, Vol. 37, Issue 1, pp. 6-13

Fraden, J, 1996, Handbook of modern sensors: physics, designs, and applications, 2nd ed., ISBN 1-56396-538-0

Goswami, J. N., K. Thyagarajan, M. Annadurai, 2006, Chandrayaan-1: Indian Mission to Moon, 37th Lunar and Planetary Science Conference, abstract no. 1704

Grande, M., B. J. Kellett, C. Howe, C. H. Perry, B. Swinyard, S. Dunkin, J. Huovelin, L. Alha, L. C. d'Uston, S. Maurice, O. Gasnault, S. Couturier-Doux, S. Barabash, K. H. Joy, I. A. Crawford, D. Lawrence, V. Fernandes, I. Casanova, M. Wieczorek, N. Thomas, U. Mall, B. Foing, D. Hughes, H.Alleyne, S. Russell, M. Grady, R. Lundin, D. Baker, C. D. Murray, J. Guest, A. Christon, 2007, The D-CIXS X-ray spectrometer on the SMART-1 mission to the Moon - First results, Planetary and Space Science, Vol. 55, pp. 494-502

Green, R., C. Pieters, P. Mouroulis, G. Sellars, M. Eastwood, S. Geier, J. Shea, 2007, The Moon Mineralogy Mapper: Characteristics and Early Laboratory Calibration Results, 38th Lunar and Planetary Science Conference, abstract no. 2345

Hamamatsu Photonics K. K., 2000, InGaAs linear image sensor G8160 to G8163/G8180 series data sheet

Hamamatsu Photonics K. K., 2003, InGaAs linear image sensor operational manual, DWG.NO.K11-B6G044, February 24, 2003

Hapke, B., 1963, A Theoretical Photometric Function for the Lunar Surface, Journal of Geophysical Research, Vol. 68, No. 15

Hapke, B., 1981, Bidirectional Reflectance Spectroscopy 1. Theory, Journal of Geophysical Research, Vol 86, No. B4, pp. 3039–3054

Hapke, B., 1993, Theory of reflectance and emittance spectroscopy, Cambridge University Press

Haruyama, J, T. Matsunaga, M. Ohtake, T. Morota, C. Honda, Y. Yokota, M. Torii, Y. Ogawa, 2008, Global lunar-surface mapping experiment using the Lunar Imager/Spectrometer on SELENE, Earth, Planets and Space, Vol. 60, pp. 243-255

Hecht, E., 2002, Optics, 4th ed., Addison Wesley, ISBN 0-321-18878-0

Hoogeveen, R. W. M., R. J. van der A, A. P. H. Goede, 2001, Extended Wavelength InGaAs infrared ($1.0 - 2.4$ μm) detector arrays on SCIAMACHY for space-based spectrometry of the Earth atmosphere, Infrared Physics and Technology, Vol. 42, 1-16

Howell, S. B., Handbook of CCD Astronomy, 2nd ed., Cambridge University Press, ISBN-13 978-0-521-61762-8

Irwin, P. G. J., A. L. Wein, S. E. Smith, F. W. Taylor, A. L. Lambert, S. B. Calcutt, P. J. Cameron-Smith, R. W. Carlson, K. Baines, G. S. Orton, P. Drossart, T. Encrenoz, M. Roos-Serote, 1998, Jovian Atmospheric Retrievals from Galileo NIMS, Journal of Geophysical Research, Vol. 103, No. E10, pp. 23001–21

Ivanov, B. A., W. K. Hartmann, 2007, Treatise on Geophysics, Vol. 10: Planets and Moons, ed. Tilman Sphon, ISBN 978-0-444-51928-3, pp. 207–236

King, P. L., M. S. Ramsey, G. H. Swayze, 2004, Infrared spectroscopy in Geochemistry, Exploration and Remote Sensing, Vol 33

Kitchin, C. R., Astrophysical Techniques, 1984, Adam Hilger Ltd., Bristol, ISBN 0-85274-461-7

Konopliv, A. S., A. B. Binder, L. L. Hood, A. B. Kucinskas, W. L. Sjogren, J. G. Williams, 1998, Improved Gravity Field of the Moon from Lunar Prospector, Science Vol. 281, pp. 1476–1479

Kreslavsky, M. A., Shkuratov, Yu. G., Velikodsky, Yu. I., Kaidash, V. G., Stankevich, D. G., Pieters, C. M., 2000, Photometric properties of the lunar surface derived from Clementine observations, Journal of Geophysical Research, Vol. 105, No. E8, pp. 20281–20295, August 25, 2000

Le Mouélic, S., Y. Langevin, S. Erard, 1999, A new data reduction approach for the Clementine NIR data set: Application to Aristillus, Aristarchus and Kepler, Journal of Geophysical Research, 104, E2, pp. 3833-3843, doi: 1998JE900035

Le Mouélic, S., Y. Langevin, S. Erard, P. Pinet, Y. Daydou, S. Chevrel, 1999, Workshop on New Views of the Moon 2: Understanding the Moon through the integration of diverse datasets

Lucey, P. G., J. L. Hinrichs, E. Malaret, 1997, Progress toward calibration of the Clementine NIR camera data set, Lunar and Planetary Science Conference XXVIII, abstract 1401

Lucey, P. G., D. T. Blewett, B. L. Jolliff, 2000, Lunar iron and titanium abundance algorithms based on final processing of Clementine ultraviolet-visible images, Journal of Geophysical Research, Vol. 105, No. E8, pp. 20297–20305

The Lunar Sample Preliminary Examination Team, 1969, Preliminary Examination of Lunar Samples from Apollo 11, Science Vol. 165, No. 3899

Mall, U., A. Nathues, H. U. Keller, SIR - a flexible, compact, low mass, near-infrared spectrometer, 2004, Sensors, Systems, and Next-Generation Satellites VII, ed. by R. Meynart, S. P. Neeck, H. Shimoda, J. B. Lurie, M. L. Aten, Proceedings of SPIE, Vol. 5234, doi:10.1117/12.511063

McCord, T. B., L. A. Soderblom, R. W. Carlson, F. P. Fanale, R. Lopes-Gautier, A. C. Ocampo, J. Forsythe, B. Campbell, J. C. Granahan, W. D. Smythe, P. R. Weissman, K. J. Becker, K. Edwards, L. Camp, J. Lo, R. Mehlman, J. Torson, G. E. Danielson, D. L. Matson, H. H. Kieffer, T. V. Johnson, 1994, Galileo infrared imaging spectrometry measurements at the Moon, Journal of Geophysical Research, Vol. 99, No. E3, pp. 5587–5600

Nagy, B. V., 2006, PRC Krochmann Ulbricht-sphere calibration, internal report, 10 March 2006

Neukum, G., R. Jaumann, H. Hoffman, J. Oberst, R. Wagner, P. Regner, H. Rebhan, H. Hiesinger, A. Dummel, 1991, Earth-based multispectral observations of the Moon22th Lunar and Planetary Science Conference, abstract 971

Nimmo, F., S. D. Hart, D. G. Korycansky, C. B. Agnor, 2008, Implications of an impact origin for the martian hemispheric dichotomy, Nature, Vol. 453, doi: 10.1038/nature07025

Nozette, S., P. Rustan, L. P. Pleasance, D. M. Horan, P. Regeon, E. M. Shoemaker, P. D. Spudis, C. H. Acton, D. N. Baker, J. E. Blamont, B. J. Buratti, M. P. Corson, M. E. Davies, D. C. Duxbury, E. M. Eliason, B. M. Jakosky, J. F. Kordas, I. T. Lewis, C. L.

Lichtenberg, P. G. Lucey, E. Malaret, M. A. Massie, J. H. Resnick, C. J. Rollins, H. S. Park, A. S. McEwen, R. E. Priest, C. M. Pieters, R. A. Reisse, M. S. Robinson, R. A. Simpson, D. E. Smith, T. C. Sorenson, R. W. Vorder Breugge, M. T. Zuber, 1994, The Clementine Mission to the Moon: Scientific Overview, Science, Vol. 266

Ohtake, M., J. Haruyama, T. Matsunaga, Y. Yokota, T. Morota, C. Honda, 2008, Performance and scientific objectives of the SELENE (KAGUYA) multiband imager, Earth, Planets and Space Vol. 60, 257-264

Pahlevan, K., D. Stevenson, 2007, Earth and Planetary Science Letters, Vol. 262, pp. 438-449

Papanastassiou, D. A., G. J. Wasserburg, 1971, Lunar chronology and evolution from Rb-Sr studies of Apollo 11 and 12 samples, Earth and Planetary Science Letters, Vol. 11, pp. 37-62

Papike, J., L. Taylor, S. Simon, Lunar Minerals in Lunar Sourcebook, ed. by G. Heiken, D. Vaniman, B. French, Cambridge University Press, ISBN 0-521-33444-6

Pieters, C., J. Boardman, B. Buratti, R. Clark, R. Green, J. W. Head III, T. B. McCord, J. Mustard, C. Runyon, M. Staid, J. Sunshine, L. Taylor, S. Tompkins, 2006, Global mineralogy of the Moon: A cornerstone to science and exploration, Lunar and Planetary Science Conference XXXVII, abstract 1630

Pieters, C. M., S. Pratt, 2000, Earth-based near-infrared collection of spectra for the Moon: A New PDS data set, 31st Annual Lunar and Planetary Science Conference, March 13-17, 2000, Houston, Texas, abstract no. 2059

Physikalisch-Technische Bundesanstalt, 2001, 4481 PTB 01 18.1.2001-8.2.2001

Racca, J. D., A. Marini, L. Stagnaro, J. van Dooren, L. di Napoli, B. H. Foing, R. Lumb, J. Volp, J. Brinkmann, R. Grünagel, D. Estublier, E. Tremolizzo, M. McKay, O. Camino, J. Schoemaekers, M. Hechler, M. Khan, P. Rathsman, G. Anderson, K. Anflo, S. Berge, P. Bodin, A. Edfors, A. Hussain, J. Kugelberg, N. Larsson, B. Ljung, L. Meijer, A. Mörtsell, T. Nordebäck, S. Persson, F. Sjöberg, 2000, SMART-1 mission description and development status, Planetary and Space Science, Vol. 50, issues 14-15, December 2000, pages 1323-1337

Rieke, G. H., 1996, Detection of Light: From the Ultraviolet to the Submillimeter, Cambridge University Press, ISBN 0-521-41028-2

Saal, A. E., E. H. Hauri, M. L. Cascio, J. A. van Orman, M. C. Rutherford, R. F. Cooper, 2008, Volatile content of lunar volcanic classes and the presence of water in the Moon's interior, Nature, Vol. 454, Issue 7201, pp. 192-195, doi: 10.1038/nature07047

Schrunk, D., B. Sharpe, B. Cooper, M. Thangavelu, 1999, The Moon – Resources, Future and Colonization, John Wiley & Sons Ltd, ISBN 0-471-97635-0

Schultz, P. H., L. J. Srnka, 1980, Cometary collisions on the Moon and Mercury, Nature Vol. 284, pp. 22–26

Sebastian, I., 2002a, SIR Calibration Plan, S1-SIR-PL-3006

Sebastian, I., 2002b, OSIRIS Monochromator Calibration Report, RO-RIS-MPAE-RP-132/1-10.7.2002

Sebastian, I., Dannenberg, A., Mall, U., Nathues, A., Perplies, H., 2002, SIR Calibration Report, S1-SIR-TR-3017

The SIR team, 2000, SIR Science and Technology Demonstration Plan 2000, project document S1-SIR-PL-3001

Shkuratov, Y, L. Strarukhina, H. Hoffmann, G. Arnold, 1999, A Model of Spectral Albedo of Particulate Surfaces: Implications for Optical Properties of the Moon, Icarus Vol. 137, pp. 235–246

Shkuratov, Yu. G., Kaydash, V. G., Kreslavsky, M. A., Opanasenko, N. V., 2001, Absolute Calibration of the Clementine UVVIS Data: Comparison with Ground-Based Observation of the Moon, Solar System Research, Vol. 35, No 1, pp. 29-34

Shkuratov, Yu. G., Kreslavsky, M. A., Ovcharenko, A. A., Stankevich, D. G., Zubko, E. S., Opposition Effect from Clementine Data and Mechanisms of Backscatter, 1999, Icarus, Vol. 141, pp. 132-155

Sitek, P., E. Vilenius, U. Mall, 2007, Performance comparison and selection criteria – an assessment for choosing the best flight detector for the SIR-2 NIR-spectrometer on Chandrayaan-1, Proceedings of SPIE, ed. by R. S. Romaniuk, Vol. 6937, 69370C, doi: 10.1117/12.784588

SIR-2 Team, 2007, SIR-2 User manual and ICD, project document C1-SIR-MA-3001

SORCE, 2008, Solar Radiation and Climate Experiment / Spectral Irradiance Monitor, <URL>http://lasp.colorado.edu/sorce/index.htm

Streetman, B. G., 1990, Solid State Electronic Devices, 3rd. ed., Prentice Hall, ISBN 0-138-22941-4

Taylor, S. R., 2005, Lunar science: An overview, Journal of Earth System Science, 114, No. 6, pp. 587-591

Telemeter Electronic GmbH, URL www.telemeter.de accessed 7.12.2005

Touboul, M., T. Kleine, B. Bourdon, H. Palme, R. Wieler, 2007, Late formation and prolonged differentiation of the Moon inferred from W isotopes in lunar metals, Nature Vol. 450, pp. 1206–1209

Zuber, M. T., D. E. Smith, G. A. Neumann, 1994, The shape and internal structure of the Moon from the Clementine Mission, Science Vol. 266, pp. 1839-1843

Publications

Publications in peer reviewed journals

U. Mall, M. Banasykiewicy, K. Brønstad, S. McKenna-Lawrol, A. Nathues, F. Søraas, *E. Vilenius*, K. Ullaland, **Near Infrared Spectrometer SIR-2 on Chandrayaan-1**, Current Science, Vol 96, No. 4, 2009

M. Markkanen, M. Lehtinen, T. Nygrén, J. Pirttilä, P. Henelius, *E. Vilenius*, E. D. Tereshchenko, B. Z. Khudukon, **Bayesian approach to satellite radiotomography with applications in the Scandinavian sector**, Annales Geophysicae, Vol. 13, pp. 1277-1287, 1995

H. Teräsranta et al. (27 co-authors), **Twenty years of monitoring of extragalactic sources at 22, 37 and 87 GHz**, Astronomy and Astrophysics, Vol. 427, pp. 769–771, 2004

E. Vilenius, T. Nygrén, M. Lehtinen, M. Markkanen, A. Väänänen, **Ionospheric Tomography**, The photogrammetric journal of Finland, Vol. 17, No. 2, pp. 78-91, 2001

Publications in peer reviewed conference proceedings

M. Lehtinen, M. Markkanen, P. Henelius, *E. Vilenius*, T. Nygrén, E. D. Tereshchenko, B. Z. Khudukon, **Bayesian approach to satellite radiotomography**, Proceedings of the International Beacon Satellite symposium, University of Wales, UK, ed. by L. Kersley, pp. 80-83, 1994

P. Sitek, *E. Vilenius*, U. Mall, **Performance comparison and selection criteria – an assessment for choosing the best flight detector for the SIR-2 NIR spectrometer on Chandrayaan-1**, Photonics Applications in Astronomy, Communications, Industry, and High-Energy Physics Experiments 2007, ed. R. S. Romaniuk, Proceedings of SPIE, Vol 6937, doi: 10.1117/12.784588, 2007

Acknowledgements

Curriculum Vitae

Name:	Esa Vilenius	
Geburtsdatum:	Januar 22, 1974	
Geburtsort:	Helsinki, Finnland	
Staatsbürgerschaft:	finnisch	
Schulbildung:	1993	Simonkylä Gymnasium, Vantaa, Finnland
Studium:	2002	M.Sc., Helsinki University of Technology Diplomarbeit: "Interferometric synthetic aperture sonar for three-dimensional imaging of riverbeds"
	2004	M.Sc., International Space University Diplomarbeit: "X-band spectral line survey of Orion KL, Taurus TMC-1 and Lupus 4"